



Norwegian University of  
Science and Technology

# The Influence of Transient Change in Strain Rate on Subgrain Size During Deformation by Torsion of AA6063

**Pål Rist**

Materials Technology

Submission date: June 2016

Supervisor: Bjørn Holmedal, IMTE

Co-supervisor: Knut Marthinsen, IMT

Norwegian University of Science and Technology  
Department of Materials Science and Engineering





---

## Preface


This thesis is the result of a master's project carried out in Trondheim, at the Department of Materials Science and Engineering at the Norwegian University of Technology and Science (NTNU). This report has been submitted as the final product of TMT4905 - Materials Technology, Master's Thesis with Professor Bjørn Holmedal as supervisor and Professor Knut Marthinsen as co-supervisor. This project is part of the COSMETEX research project financed by SAPA and The Research Council of Norway with NTNU and SINTEF as research partners.

I would especially like to thank Post-Doctorate Kai Zhang for the help with data analysis, texture simulations and guidance during this whole project. I would like to give another special thanks to Trygve Lindahl Schanche for assisting me at the torsion laboratory, and making the torsion experiments possible.

My greatest acknowledgment is directed toward my supervisor, Professor Bjørn Holmedal, for sharing his knowledge and counsel throughout this project. I would also like to thank Professor Knut Marthinsen for providing guidance during this project.

Finally, I would like to thank my family and Christina Tønset, for support, guidance and proof-reading.

Trondheim, June 2016



Pål Rist



---

## Abstract

During hot extrusion a extrusion billet's cross section is reduced, altering the metals microstructure. As the billet is passing through the extrusion die the strain rate and temperature increases, resulting in a highly deformed extrusion profile with high subgrain density, giving a great driving force for recrystallisation. The extruded profile recrystallises almost immediately after the extrusion die [1, 2]. However, recrystallisation after extrusion of non-dispersoid containing alloys like AA6063 is not fully understood. Such alloys tend to undergo uncontrolled grain growth in the surface area [2, 3].

This master project aims to give a better understanding of the recrystallisation process occurring under extrusion by investigating the subgrain size evolution during transient changing strain rates. Using torsion to deform the metal, the deformation starts with a high (1<sup>st</sup>) strain rate allowing the steady-state microstructure of the high strain rate to be developed, then immediately changing the strain rate to a lower (2<sup>nd</sup>) strain rate, effectively simulating the passing through the extrusion die. The objective was to identify the strain region in which the subgrain size is in a transient state between the 1<sup>st</sup> and the 2<sup>nd</sup> steady-state microstructure, referred to as the metals deformation memory.

AA6063s deformation memory at 375°C was found to be in the higher strain region of shear strains between 0.18 – 0.26 (equivalent to strains between 0.10 – 0.15). In the investigated strain region it was found little texture evolution. Investigations of the texture found that the samples' texture intensity increased with recovery due to annihilation of the orientation gradients. A correlation between the recorded stress and the deformation memory was also found, whereas the stress is in a transient state during the deformation memory.



---

## Sammendrag

Under varmekstrudering blir tverrsnittsarealet til en pressbolts redusert og mikrostrukturen endres. Når pressbolten passerer gjennom ekstruderingsdysen øker tøyningshastigheten og temperaturen. Dette fører til at bolten blir sterkt deformert med en finfordelt subkornstruktur med høy subkornstetthet. Den høye subkornstettheten gir stor drivkraft for rekrytallisering, og profilen rekrytalliseres nesten umiddelbart etter ekstruderingsdysen [1, 2]. Denne reskrytalliseringprosessen etter ekstruderingen er ikke fullstendig forstått. Etter ekstrudering kan dispersoidfrie legeringer som AA6063 få uønsket ukontrollert kornvekst [2, 3].

Dette masterprosjektets mål er å gi en bedre forståelse av rekrytalliseringprosessen som skjer etter ekstrudering ved å undersøke subkornstørrelsesutviklingen under transiente varierende tøyningshastigheter. Ved bruk av torsjon for å deformere metallet blir det først deformert med en høy (1.) tøyningshastighet til steady-state spenningsflyt, og deretter umiddelbart endret til en lav (2.) tøyningshastighet simuleres deformasjonen som skjer gjennom en ekstruderingsdyse. Målet var å identifisere tøyingsregionen hvor subkornstørrelsene er i en transient tilstand mellom 1. og 2. tøyningshastighets steady-state spenningsflyt, definert som metallets deformasjonsminne.

Det ble funnet at AA6063s deformasjonsminne ved  $375^{\circ}\text{C}$  er i den høyere regionen av skjærtøyninger mellom 0.18 – 0.26 (tilsvarende tøyninger lik 0.10 – 0.15). Det ble funnet lite teksturendring i den undersøkte tøyingsregionen. Undersøkelser av teksturen viste at prøvenes teksturintensitet økte ved recovery, som følge av annihilasjon av orienteringsgradienter i subkornstrukturen. Det ble funnet en korrelasjon mellom den målte skjærspenningen og deformasjonsminnet, hvor spenningen er i en transient tilstand ved deformasjonsminnet.

## Table of Contents

<b>Figures</b>	<b>viii</b>
<b>Tables</b>	<b>ix</b>
<b>1 Introduction</b>	<b>1</b>
<b>2 Theory</b>	<b>3</b>
2.1 Torsion Testing . . . . .	3
2.2 Microstructural Evolution . . . . .	6
2.2.1 Static Recrystallisation . . . . .	6
2.2.2 Dynamic Recovery . . . . .	8
2.2.3 Constitutive Relationships . . . . .	10
2.3 Texture . . . . .	11
2.3.1 Torsion Texture . . . . .	13
2.3.1.1 Deformation Torsion Texture . . . . .	13
2.3.1.2 Annealed Torsion Texture . . . . .	15
2.3.1.3 Simulated Torsion Texture . . . . .	17
2.4 Experimental Techniques . . . . .	19
2.4.1 Electron Backscatter Diffraction . . . . .	19
2.4.2 X-Ray Diffraction . . . . .	20
2.4.3 The Torsion Machine . . . . .	21
2.4.3.1 Proportional Integral Derivative Control . . . . .	23
<b>3 Material and Experiments</b>	<b>24</b>
3.1 The AA6063 material . . . . .	24
3.2 Method . . . . .	25
3.3 Experimental Plan . . . . .	28

---

<b>4 Experimental Results</b>	<b>31</b>
4.1 Average Subgrain Size . . . . .	33
4.2 Measured stress . . . . .	35
4.3 Texture . . . . .	37
<b>5 Discussion</b>	<b>43</b>
5.1 Deformation Memory . . . . .	43
5.1.1 Shear Stress Evolution . . . . .	43
5.1.2 Subgrain Size Evolution . . . . .	44
5.1.3 Implications of the Deformation Memory . . . . .	46
5.2 Texture Development . . . . .	48
5.3 Result accuracy . . . . .	53
<b>6 Conclusion</b>	<b>56</b>
<b>7 Referanses</b>	<b>57</b>
<b>Appendix A Derivation of the Grain Elongated</b>	<b>1</b>
<b>Appendix B IPF and IQ-maps</b>	<b>2</b>
<b>Appendix C The Average Grain Size Values</b>	<b>12</b>
<b>Appendix D Pole figures</b>	<b>13</b>
<b>Appendix E The full ODFs</b>	<b>17</b>

## List of Figures

1.1	(a) The extrusion process. (b) Uniform grain structure. (c) Uncontrolled grain growth.	1
2.1	The torsion sample with measurements.	3
2.2	(a) Quadratic grain with diagonal length $S_0$ . (b) Deformed grain with diagonal length $S$ .	5
2.3	The different stages of recovery of a deformed metal.	7
2.4	The different stages of recrystallisation of a deformed metal.	7
2.5	Summary of the microstructural changes which occur during dynamic recovery.	9
2.6	Construction of a $\{100\}$ -pole figure.	11
2.7	Representation of orientations in the Euler Space.	12
2.8	Orientation of the pole figures with respect to the $r$ , $\theta$ and $z$ axes of the sample.	13
2.9	Schematic ideal texture components (from Table 2.1) for torsion deformed aluminium, illustrated in $\{111\}$ -pole figures.	14
2.10	Schematic ideal texture components (from Table 2.1) for torsion deformed aluminium, illustrated in $\{200\}$ -pole figures.	14
2.11	Schematic ideal texture components (from Table 2.1) illustrated in ODFs	15
2.12	Schematic illustration of the caption of the diffraction pattern from a sample.	19
2.13	The torsion machine.	21
2.14	The fixture of the torsion sample.	22
2.15	Schematic illustration of the PID controller mechanism.	23
3.1	Sample preparation of torsion sample. (a) Removal of core. (b) Cut into a half cylinder (c) Flattening of sample with use of an hydraulic press.	25
3.2	Illustration of the experimental plan.	28
3.3	Illustration of the $Z$ -values in relation to a HyperXtrude extrusion simulations for a particle traveling at a radius of $1.425\text{mm}$ in a aluminium profile with a radius of $1.5\text{mm}$ . Adapted from Zhang (2016) [37].	29
4.1	An illustration of the line intercept measuring-lines in relation to the sense of shear. Both maps are presented with the horizontal direction in the $z$ direction and the vertical direction in the $\theta$ direction in relation to the torsion samples.	33
4.2	The line intercept subgrain boundary counting method. Graph of a smaller area of $11\mu\text{m}$ with three identified subgrain boundaries.	34
4.3	The average subgrain size as a function of the 2 <sup>nd</sup> shear strain, with the standard deviation marked in grey.	35



4.4	(a) 1 <sup>st</sup> steady-state stress-shear-strain curve, and (b) 1 <sup>st</sup> and 2 <sup>nd</sup> steady-state stress-shear-strain curve. . . . .	36
4.5	XRD obtained ODF for Sample $\pi - 0$ . . . . .	37
4.6	The different component intensities for (a) $\varphi_2 = 0^\circ$ and (b) $\varphi_2 = 45$ . . . . .	40
4.7	Components intensity fractions of the components for (a) $\varphi_2 = 0^\circ$ and (b) $\varphi_2 = 45$ . . . . .	41
5.1	Expected stress evolution. . . . .	43
5.2	The average subgrain size as a function of 2nd shear strain, with the standard deviation marked in grey and the approximated subgrain size as a function of 2nd shear strain (red line). . . . .	45
5.3	PTP-line intercept measurement for (a) Sample Ref.3 400 (b) Sample Ref.4 400NQ and (c) Sample Ref.5 375 RX 120s. The measurements were taken parallel the sense of shear. . . . .	49
5.4	Recorded torsion measurements for angle of twist as a function of time. . . . .	54
B.1	The colour representation of crystallographic orientations. . . . .	2
B.2	(a) The IPF-map and (b) IQ-map for Sample Ref.1 350°C. . . . .	2
B.3	(a) The IPF-map and (b) IQ-map for Sample Ref.2 375°C. . . . .	3
B.4	(a) The IPF-map and (b) IQ-map for Sample Ref.3 400°C. . . . .	3
B.5	(a) The IPF-map and (b) IQ-map for Sample Ref.4 400°C NQ. . . . .	4
B.6	(a) The IPF-map and (b) IQ-map for Sample Ref.5 375°C annealed 120sec. . . . .	4
B.7	(a) The IPF-map and (b) IQ-map for Sample 0- $\pi$ . . . . .	5
B.8	(a) The IPF-map and (b) IQ-map for Sample $\pi$ -0 NQ. . . . .	5
B.9	(a) The IPF-map and (b) IQ-map for Sample 0-4.71. . . . .	6
B.10	(a) The IPF-map and (b) IQ-map for Sample $\pi$ -1.4. . . . .	6
B.11	(a) The IPF-map and (b) IQ-map for Sample $\pi$ -0.7. . . . .	7
B.12	(a) The IPF-map and (b) IQ-map for Sample $\pi$ -0.5. . . . .	7
B.13	(a) The IPF-map and (b) IQ-map for Sample $\pi$ -0.87. . . . .	8
B.14	(a) The IPF-map and (b) IQ-map for Sample $\pi$ -0.34. . . . .	8
B.15	(a) The IPF-map and (b) IQ-map for Sample $\pi$ -0.26. . . . .	9
B.16	(a) The IPF-map and (b) IQ-map for Sample $\pi$ -0.18. . . . .	9
B.17	(a) The IPF-map and (b) IQ-map for Sample $\pi$ -0.14. . . . .	10
B.18	(a) The IPF-map and (b) IQ-map for Sample $\pi$ -0.13. . . . .	10
B.19	(a) The IPF-map and (b) IQ-map for Sample $\pi$ -0.03. . . . .	11

E.1	ODF for Sample Ref.1 350°C . . . . .	17
E.1	ODF for Sample Ref.2 375°C . . . . .	18
E.1	ODF for Sample Ref.3 400°C . . . . .	19
E.1	ODF for Sample Ref.4 400°C NQ . . . . .	20
E.1	ODF for Sample Ref.5 375°C annealed 120sec . . . . .	21
E.1	ODF for Sample 0- $\pi$ . . . . .	22
E.1	ODF for Sample $\pi$ -0 NQ . . . . .	23
E.1	ODF for Sample 0-4.71 . . . . .	24
E.1	ODF for Sample $\pi$ -1.4 . . . . .	25
E.1	ODF for Sample $\pi$ -0.7 . . . . .	26
E.1	ODF for Sample $\pi$ -0.50 . . . . .	27
E.1	ODF for Sample $\pi$ -0.44 . . . . .	28
E.1	ODF for Sample $\pi$ -0.34 . . . . .	29
E.1	ODF for Sample $\pi$ -0.26 . . . . .	30
E.1	ODF for Sample $\pi$ -0.18 . . . . .	31
E.1	ODF for Sample $\pi$ -0.14 . . . . .	32
E.1	ODF for Sample $\pi$ -0.13 . . . . .	33
E.1	ODF for Sample $\pi$ -0.03 . . . . .	34

## List of Tables

2.1	Torsion fibre components for f.c.c. metals [5, 22, 9, 23, 24, 25, 26, 27]. The representation of orientations is in the $\{z\}\langle\theta\rangle$ form, where $z$ is the axial direction and $\theta$ is the tangential direction relative to the torsion. . . . .	14
2.2	Torsion textures of pure (99.7%) aluminium at 400°C (not quenched) with a strain rate of 0.2/s. . . . .	16
2.3	Generated ODF sections with the Alamel-model of $\varphi_2 = 0^\circ$ and $\varphi_2 = 45$ with contour maps with intensities of 1.5/6/12/18/24/31/40. The components are given i Table 2.1. . . . .	17
2.4	Generated ODF sections with the FC-Taylor-model of $\varphi_2 = 0^\circ$ and $\varphi_2 = 45$ with contour maps with intensities of 1.5/6/12/18/24/31/40. The components are given i Table 2.1 . . . . .	18
3.1	The alloy elements in AA6063 given in weight percent [34, 35]. . . . .	24
3.2	Parameters for electropolishing. . . . .	26
3.3	Parameters for EBSD . . . . .	26
3.4	The experimental plan. Each sample undergoes a 1 <sup>st</sup> and a 2 <sup>nd</sup> angle of twist ( $\theta_{1,2}$ ), with different angular velocities ( $\omega_{1,2}$ ). NQ means not quenched. . . . .	30
4.1	The samples shear strain and strain. . . . .	32
4.2	The ODF sections of $\varphi_2 = 0^\circ$ and $\varphi_2 = 45$ with contour maps with intensities of 1.5/2.5/4/8/10/12. The components are given i Table 2.1 . . . . .	38
4.3	The $\{111\}$ and $\{200\}$ -pole figures for Sample $\pi-0$ with contour maps with intensities of 1/2/3/4.5/6. . . . .	42
5.1	Subgrain sizes for Ref.3, Ref.4 and Ref.5. . . . .	50
C.1	Values used in in Figure 4.3. . . . .	12
D.1	The 111 and 200-pole figures with contour maps with intensities of 1/2/3/4.5/6. . . . .	16



## 1 Introduction

Hot extrusion is a process for shaping metal by forcing it through a die, reducing its cross section and altering its microstructure. The process starts with preheating a billet, allowing for plastic deformation, before it is placed inside the extrusion chamber. A ram then presses the billet through the extrusion die and the profile is extruded. This process is shown in Figure 1.1a. Figure 1.1a also shows the metals outer edge strain rate in relation to the extrusion chamber. As the billet is pressed closer to the extrusion die, the strain rate increases [1].

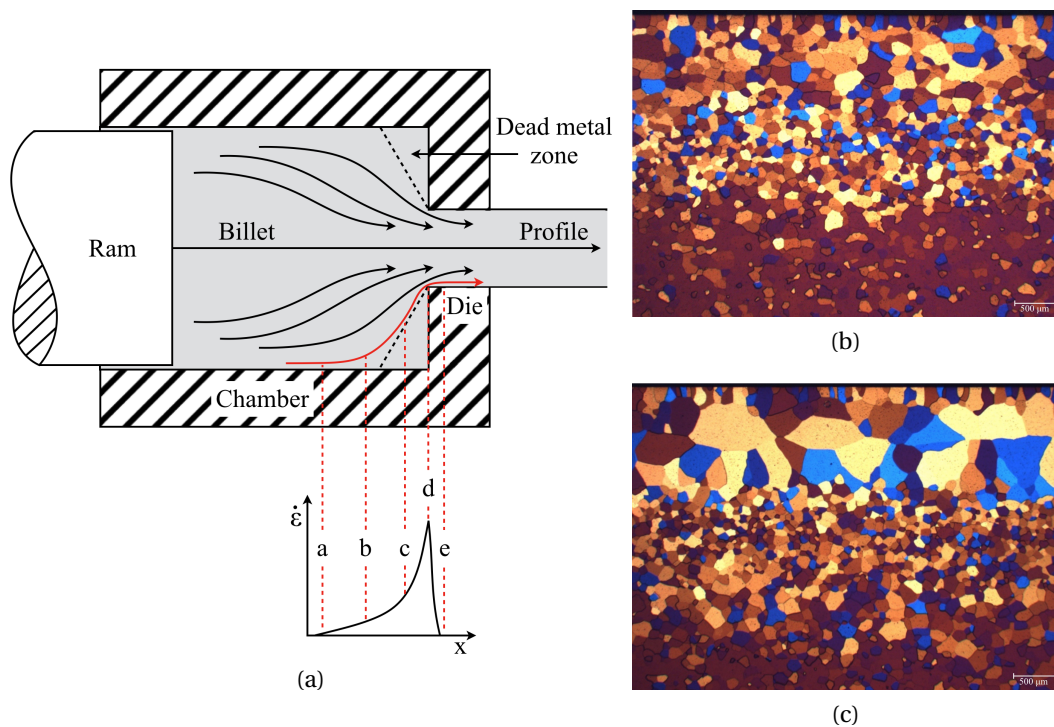


Figure 1.1: (a) A extrusion chamber with strain rates illustrated for one flow path. (b) An extrusion profile with uniform grain structure and (c) an extrusion profile with uncontrolled grain growth in the surface area.

When the metal has passed through the extrusion die the strain rate is equal to zero, and the material is extremely deformed with a finely grained structure and a high density of subgrains. The outer edge of the billet experiences the highest stress during extrusion and therefore has the highest subgrain density [2]. The subgrain density, in addition to the elevated temperature, gives the surface great driving force for recrystallisation, recrystallising the profile almost immediately

after the extrusion die. The profile is then water cooled to stop further grain growth, giving a uniform grain structure as shown in Figure 1.1b. However, recrystallisation after extrusion of non-dispersoid alloys like AA6063 is not fully understood. After extrusion AA6063 tend to undergo uncontrolled grain growth in the surface area as shown in Figure 1.1c [1, 2, 3].

This master project aims to give a better understanding of the recrystallisation process occurring under extrusion by investigating the subgrain size evolution during transient changing strain rates. Using torsion to deform the metal, the deformation starts with a high (1<sup>st</sup>) strain rate allowing the steady-state microstructure of the high strain rate to be developed (point *d* in Figure 1.1a), then immediately changing to a lower (2<sup>nd</sup>) strain rate (point *e* in Figure 1.1a), effectively simulating the passing through the extrusion die. By performing experiments with various 2<sup>nd</sup> strains, the subgrain size evolution will be investigated. The objective is to identify the strain region in which the subgrain size is in a transient state between the 1<sup>st</sup> and the 2<sup>nd</sup> steady-state microstructure. This region of strain is henceforth referred to as the metals *deformation memory*. During this investigation the texture evolution and the deformation stress will also be investigated.

## 2 Theory

In the following section the material used in this work will be presented, a description of torsion will be given, the microstructural evolution in hot deformation will be described as well as presentation of texture and torsion texture. Lastly, the experimental techniques used in this project will be described.

### 2.1 Torsion Testing

Torsion tests can be used to apply equal Z-values (§2.2.3) for strain rates and temperatures found in extrusion. Using torsion a samples temperature can be precisely controlled meanwhile it's geometry remains almost unchanged during deformation [4]. The torsion parameters (temperature, angle of twist and the angular velocity) are set prior to torsion and recorded during torsion. The stress, strain and strain rate are calculated from an inverse approximated solution based on the recorded torsion parameters, in addition to the samples geometry (Figure 2.1).

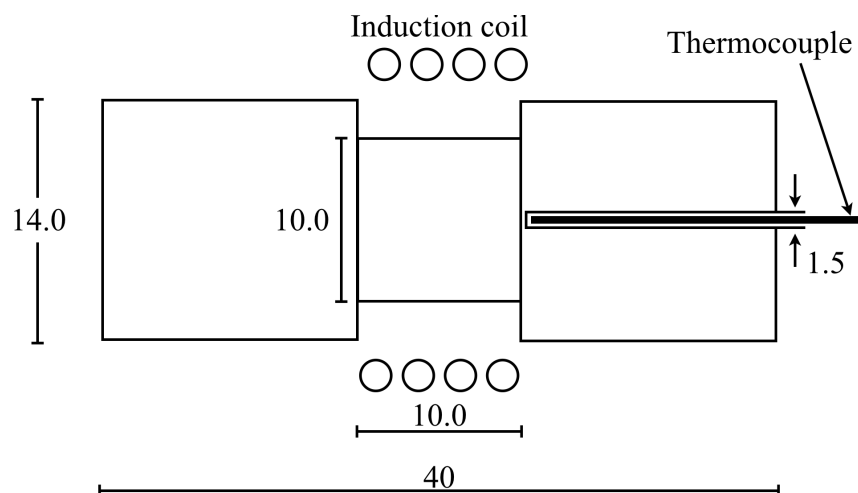


Figure 2.1: Sketch of a torsion sample showing sample measurements [mm], induction coil used for heating and the placement of the thermocouple for temperature regulation. The figure is adapted from Tanja Pettersen (1999) [5].

Presuming that the part of the specimen that deforms of the torsion sample is a cylindrical bar of length  $L$  with a cross section of radius  $r$ , which is subject to the angle of twist  $\theta$ , the shear strain and shear strain rate at the sample surface is expressed by Equation 1 and 2, given the following assumptions [1, 5]:

- The samples geometry stays unchanged during torsion
- The twist along the length is uniform
- The torsion axis is in the centre of the sample
- The sample is uniform isotropic

$$\gamma = \frac{r\theta}{L} \quad (1)$$

$$\dot{\gamma} = \frac{r}{L} \frac{d\theta}{dt} = \frac{r\omega}{L} \quad (2)$$

Where  $\omega$  is the angular velocity. Using the equivalent von Mises strain the shear strain and shear strain rate can be expressed by Equation 3 and 4. Von Mises assumes that the strain only arises from torsional revolutions [5, 6, 7, 8].

$$\epsilon = \frac{\gamma}{\sqrt{3}} \quad (3)$$

$$\dot{\epsilon} = \frac{\dot{\gamma}}{\sqrt{3}} \quad (4)$$

The shear stress ( $\tau$ ) for a solid cylindrical bar of radius  $r$ , with an angle of twist  $\theta$  and at an angular velocity  $\omega$ , giving the torque  $\Gamma(\theta, \omega)$ , given constant a  $\omega/\theta$ -ratio that the shear stress on the surface of a sample can be expressed in Formula 5 [5, 8].

$$\tau_r = \frac{\Gamma}{2\pi r^3} (3 + p + q) \quad (5)$$

Where  $p$  is the strain-hardening exponent defined by  $\partial(\ln\Gamma)/(\ln\theta)|_{\omega}$  and  $q$  is the strain rate



sensitivity defined by  $\partial(\ln \Gamma) / (\ln \omega)|_{\theta}$ . Given the von Mises criterion, the stress in the surface of the torsion sample can be expressed by Equation 6 [5, 9, 8]

$$\sigma_r = \sqrt{3}\tau \quad (6)$$

During torsion the grains are elongated along the tangential direction. This elongation can be calculated for a simplified quadratic grain with sides  $l$  and original length of diagonal  $S_o$  as a function of shear strain. Equation 7 (derived in Appendix A) shows the relation between a quadratic shaped grain and a parallelogram shaped grain with length of diagonal  $S$ , illustrated in Figure 2.2 [10].

$$\frac{S}{S_o} = \sqrt{\frac{1}{2} + \frac{1}{2}(\gamma + 1)^2} \quad (7)$$

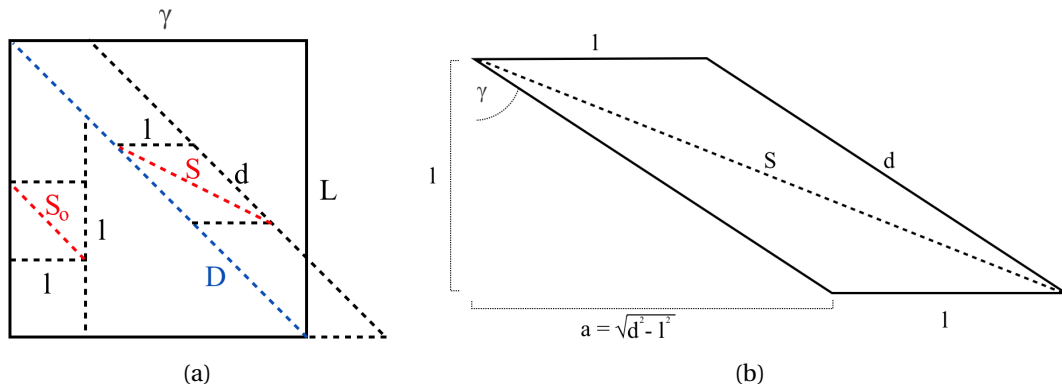


Figure 2.2: (a) Quadratic grain with diagonal length  $S_o$ . (b) Deformed grain with diagonal length  $S$ .

## **2.2 Microstructural Evolution**

When extruding a billet the deformation produces heat and the strain and strain rate is increased as the metal passes through the die, subsequently the extruded profile may become recrystallised, leaving a deformation free microstructure. In the following section the recovery and recrystallisation processes occurring at this stage are explained.

### **2.2.1 Static Recrystallisation**

Static recrystallisation is a process which occurs after a metal is deformed and it has sufficient stored energy for nucleation to spontaneously occur. The stored energy is accumulated in the metals microstructure in form of dislocations. When a metal is deformed most of the work spent in deforming produces heat, and only a small amount ( $\sim 1\%$ ) remains as stored energy in the metal. As the metal is more deformed the dislocation density increases, and thus the stored energy. This stored energy, the dislocation density, is the driving force for recrystallisation [2].

In order for the metal to release its stored energy the recovery process (Figure 2.3) initiates, allowing the dislocations to annihilate each other. Subsequently cells form with dislocation accumulated boundaries as illustrated in Figure 2.3b-c. Subgrains then form from the cells. As the subgrains grow, they transform into nucleation points for recrystallisation, causing the recrystallisation texture to be similar to the deformation texture. This nucleation mechanism is called grain boundary nucleation [2]. In torsion, grain boundary nucleation is known to be the dominating form of nucleation [11].

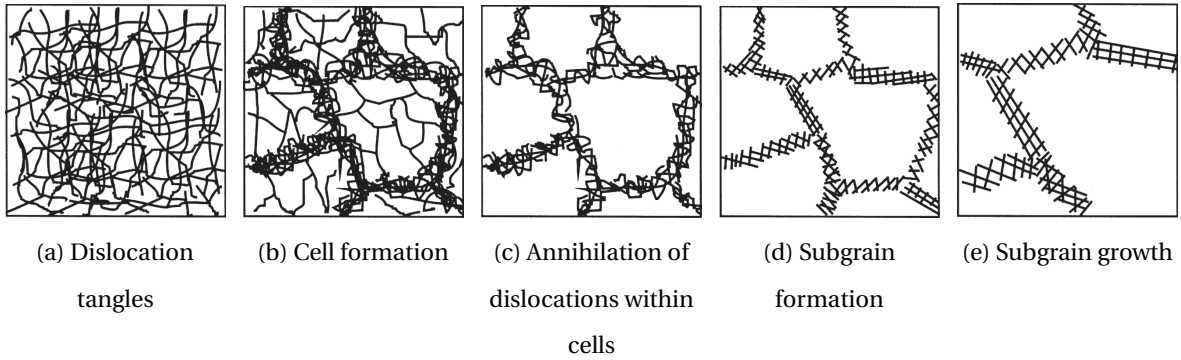


Figure 2.3: The different stages of recovery of a deformed metal. Figure adapted from Humphreys & Hatherly (2004) [2].

After recovery the nucleation process initiates as illustrated in Figure 2.4c. Nucleation is the initiation of recrystallisation. The recovery and nucleation processes are competing processes for releasing the stored energy. For nucleation to occur two criteria must be satisfied; the nucleus must be larger than a critical size ( $\delta_c$ ), and the nucleus must have an misorientation advantage ( $\theta \sim 15^\circ$  to the surrounding microstructure). The first criterion can be expressed with the Gibbs-Thomson relation in Formula 8 [2, 5]:

$$\delta > \delta_c = \frac{4\gamma_{GB}}{P_D} \quad (8)$$

Where  $\delta$  is the diameter of the growing deformation free subgrain,  $\gamma_{GB}$  is the specific grain boundary energy and  $P_D$  is the driving pressure on the grain boundary [5].

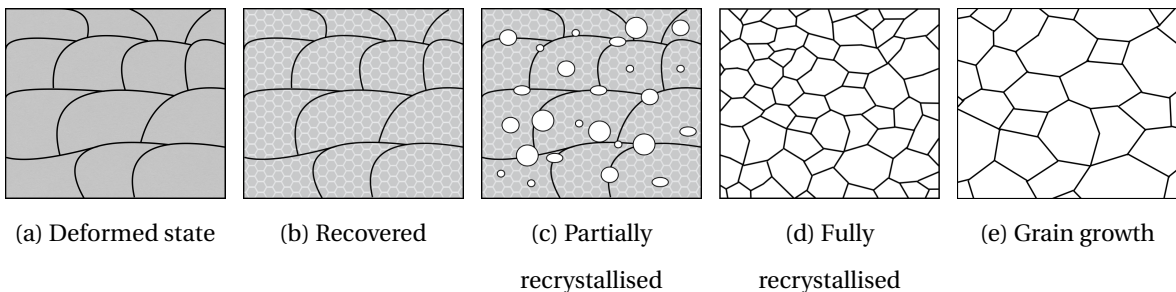


Figure 2.4: The different stages of recrystallisation of a deformed metal. Figure adapted from Humphreys & Hatherly (2004) [2].

The recrystallisation process consumes the deformed substructure leaving a deformation free microstructure with no stored energy. If the recrystallised grains have an misorientation advantage they will continue to grow and consume smaller grains, illustrated in 2.4d-e [2].

Static recrystallisation can be reduced to a three step process [2, 12]:

1. Recovery, *movement of dislocations and release of stored energy.*
2. Recrystallisation, *release of stored energy and movement of high angle grain boundaries.*
3. Grain growth, *reducement of surface energy by movement of high angle grain boundaries.*

In two-phase alloys like AA6063 second-phase particles can have an effect on the recrystallisation behaviour of the material. Particles are known for their ability to prevent grain boundary migration, due to the dislocation density surrounding the particles. The surrounding region of high dislocation density and large orientation gradients (see Texture §2.3) is an ideal location for the development of a recrystallisation nucleus. This is called particle stimulated nucleation (PSN). PSN recrystallised grains will often be different orientated than grain boundary nucleation grains, and typically give rise to a weak random texture [2, 13].

### 2.2.2 Dynamic Recovery

In metals of high stacking fault energy (e.g. aluminium,  $\alpha$ -iron and most BCC metals), dynamic recovery occurs during deformation. The stress-strain curve in Figure 2.5 illustrates the microstructural changes which occur during dynamic recovery. In the initial deformation, the stress increases as a result of dislocation multiplication arising from the deformation (work hardening). As the dislocation density rises, so does the driving force for recovery. At a certain stage the rate of recovery and the rate of work hardening reaches a dynamic equilibrium, with a constant dislocation density, resulting in steady-state flow stress [2].

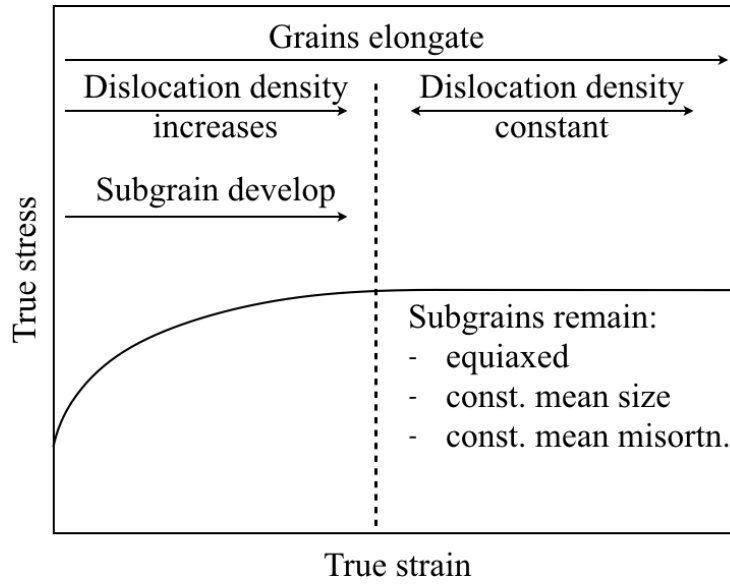


Figure 2.5: Summary of the microstructural changes which occur during dynamic recovery. Figure adapted from Humphreys & Hatherly (2004) [2].

Figure 2.5 illustrates how the stress evolves at small strains as subgrains develop from dislocation tangles. At higher strains the subgrain size stabilises during constant strain. As the subgrains develop new dislocation are introduced with the strain, giving rise to new cell formation and eventually new subgrains, resulting in a negative contribution  $\left(\frac{\partial\delta^-}{\partial\epsilon}\right)$  on the subgrain size. As the deformation continues dynamic recovery occurs, giving a positive contribution  $\left(\frac{\partial\delta^+}{\partial\epsilon}\right)$  to the subgrain size. These contributions are incorporated in Formula 9 as a parameter for the change in subgrain size [14, 15].

$$\frac{\partial\delta}{\partial\epsilon} = \frac{\partial\delta^-}{\partial\epsilon} + \frac{\partial\delta^+}{\partial\epsilon} \quad (9)$$

When  $\left(\frac{\partial\delta}{\partial\epsilon}\right)$  is equal to zero the deformation is in steady-state.

The flow stress can be expressed by Formula 10 [5]:

$$\sigma = \sigma_i + \alpha_1 M G b \sqrt{\rho_i} + \alpha_2 M G b \sqrt{\frac{1}{\delta}} \quad (10)$$

Where  $\sigma_i$  is the frictional stress,  $M$  is the Taylor factor (3.06 is often used for FCC metals),  $\alpha_1$  and  $\alpha_2$  are constants,  $G$  is the shear modulus,  $b$  is the Burgers vector and  $\rho_i$  is the dislocation density within a cell [14, 15]. While the Taylor factor is different for each grain depending on its orientation, each grain will have a different  $M$ -value ranging from 2.5 to 3.5, thus the stress two grains experiences stress could vary up to 40% [16]. From Formula 10, it can be seen that the flow stress is inversely proportional to the subgrain size:

$$\sigma \propto \left( \frac{1}{\delta} \right) \quad (11)$$

### 2.2.3 Constitutive Relationships

During steady state deformation the microstructural development is depending on the deformation temperature ( $T$ ) given in Kelvin and strain rate ( $\dot{\epsilon}$ ) in addition to the total strain ( $\epsilon$ ). The strain rate and deformation temperature are often incorporated into one parameter, The Zener–Hollomon parameter ( $Z$ -value), given in Equation 12 [2]:

$$Z = \dot{\epsilon} \exp\left(\frac{Q}{RT}\right) \quad (12)$$

Where  $Q$  is the activation energy and  $R$  is the gas constant ( $8.3145 \text{ J/mol K}$ ). For aluminium alloys the activation energy is about  $156 - 160 \text{ kJ/mol}$  [14]. The Zener–Hollomon parameter is particularly useful, since it can correlate stress, deformation temperature and strain rate in steady-state deformation [2].

## 2.3 Texture

Texture is the statistical distribution of crystallographic orientations in a polycrystalline. When deforming a sample the samples texture changes, and with it the samples properties such as strength and ductility [17]. By identifying different textures and their connection to the sample's microstructure and properties, one can better understand mechanisms such as recrystallisation and the mechanisms connection to a samples texture.

Texture is often presented in pole figures [2, 17]. Pole figures are stereographic projection's for the statistical distribution of crystallographic orientations of grain orientations in a polycrystalline. Figure 2.6 illustrates the construction of a  $\{100\}$ -pole figure. When a polycrystal has a certain crystallographic texture, regions of higher density are shown in a contour map as shown in Figure 2.6d. The different density distributions are often illustrated with different lines of equal density, as illustrated in Figure 2.6e [17, 18].

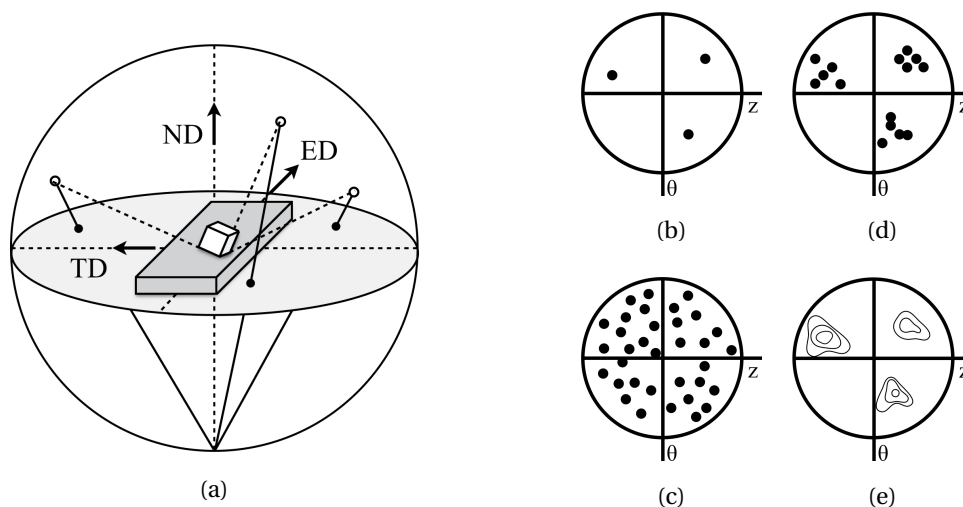


Figure 2.6: Construction of a  $\{100\}$ -pole figure. (a) Stereographic projection of the  $\{100\}$ -poles. (b) projection of the  $\{100\}$ -poles of one grain on the equatorial plane. (c) projection of the  $\{100\}$ -poles of a polycrystal. (d) projection of the  $\{100\}$ -poles of a textured polycrystal. (e) contour map of the  $\{100\}$ -pole density distribution. Figure adapted from Verlinden *et al.* (2007) [18].

Crystal orientations can be expressed with Miller indices in  $\{hkl\}\langle uvw \rangle$ -form. For extrusion, the reference frame for indexing texture is usually given by the extrusion direction (ED), the

normal direction (ND) and the transverse direction (TD), as illustrated in Figure 2.6a, where  $\{hkl\}$  is a plane parallel with the rolling plane and the direction  $\langle uvw \rangle$  is parallel with the ED. Axisymmetric processes like wire-drawing or torsion produces fibre textures in samples. Fibre texture is described by only one set of Miller indices, e.g.  $\langle uvw \rangle$ , meaning that all crystallographic orientations in the fibre are parallel to the  $\langle uvw \rangle$  axis regardless of the  $\{hkl\}$ -rotation [18].

Another common way of representing texture is with Orientation Distribution Functions (ODFs). An ODF is based on the three Euler angles of rotations, commonly referred to with the Bunge notation:  $\varphi_1, \Phi$  and  $\varphi_2$  [19]. ODF's are three-dimensional representations in the Euler Space, where every single crystal orientation can be represented. For portraying ODF's the Euler space is usually divided in cross sections of constant  $\varphi_2$ , e.g.  $\varphi_2 = 0^\circ$ ,  $\varphi_2 = 5^\circ$ , till  $\varphi_2 = 90^\circ$  [18]. Figure 2.7 illustrates the Euler Space with a crystal orientation  $\alpha$ , given where the Euler angles  $\varphi_1 = 130^\circ$   $\Phi = 90^\circ$  and  $\varphi_2 = 180^\circ$  meets in the Euler Space. Engler & Randle (2009) [17] explains in depth how to obtain and calculate  $\alpha$ .

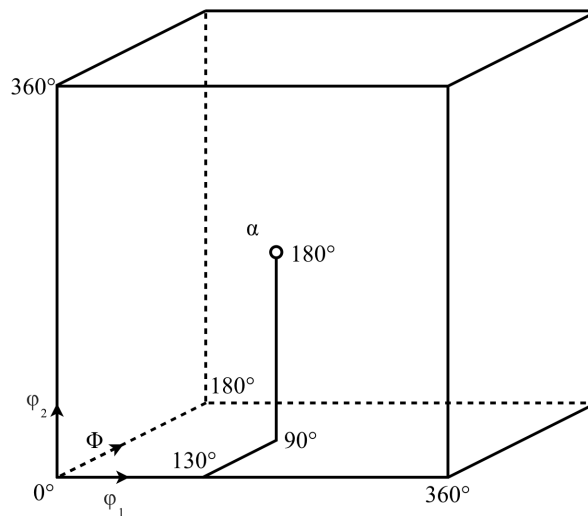


Figure 2.7: Representation of orientations in the Euler Space, with an illustrated orientation  $g$  with Euler angles:  $\varphi_1 = 130^\circ$   $\Phi = 90^\circ$  and  $\varphi_2 = 180^\circ$ . The figure is adapted from Verlinden *et al.* (2007) [18].

A grain or subgrain may have significant orientation gradients within, giving a spectre of orientations within the grain or subgrain. Such grains/subgrains are usually found where the nearest-neighbour misorientations are low and are often associated with the presence of second phase-particles. These orientation gradients are of relevance when studying the nucleation of



recrystallisation, due to the increase in dislocation density. An orientation gradient ( $\Omega$ ) can be defined as the rate of accumulation of misorientation ( $d\theta$ ) across some region of the microstructure ( $dx$ ), given in Formula 13 [2].

$$\Omega = \frac{d\theta}{dx} \quad (13)$$

### 2.3.1 Torsion Texture

In the following presentation of torsion texture, the crystal orientations are given in  $\{z\}\langle\theta\rangle$ -form. Figure 2.8 illustrates the  $\{z\}\langle\theta\rangle$ -notation with respect to the axial ( $z$ ), tangential ( $\theta$ ) and normal ( $r$ ) direction of the torsion sample.

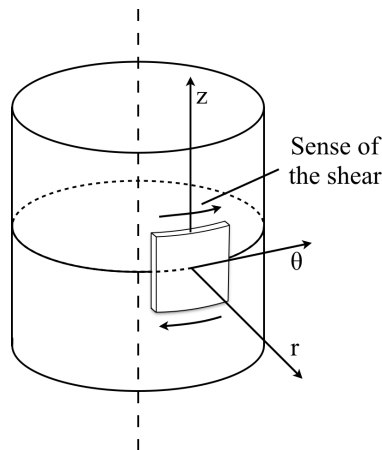


Figure 2.8: Orientation of the pole figures with respect to the  $r$ ,  $\theta$  and  $z$  axes of the sample.

#### 2.3.1.1 Deformation Torsion Texture

Experiments by Montheillet *et al.* (1984) have shown that deformed torsion textures in pure aluminium consists of an A-fibre ( $\{111\}\langle uvw\rangle$ ), an B-fibre ( $\{hkl\}\langle 110\rangle$ ) and a C-component as shown in Table 2.1 [5, 20]. However, only parts of the A-fibre and B-fibre were observed.  $A^{1,2}$  and  $B^1$  are fragments of their corresponding fibres presented in Table 2.1, which ideal orientations are illustrated as  $\{111\}$ -pole figures in Figure 2.9 and as  $\{200\}$ -pole figures in Figure 2.10 [5, 21, 9].

Table 2.1: Torsion fibre components for f.c.c. metals [5, 22, 9, 23, 24, 25, 26, 27]. The representation of orientations is in the  $\{z\}\langle\theta\rangle$  form, where  $z$  is the axial direction and  $\theta$  is the tangential direction relative to the torsion.

Component	Symbol	$\{z\}\langle\theta\rangle$	Symbol	$\{z\}\langle\theta\rangle$
$A^1$	$\triangle$	$\{111\}\langle\bar{1}10\rangle$	$\blacktriangle$	$\{111\}\langle1\bar{1}0\rangle$
$A^2$	$\blacktriangledown$	$\{111\}\langle2\bar{1}\bar{1}\rangle$	$\blacktriangledown$	$\{111\}\langle\bar{2}11\rangle$
$B^1$	$\square$	$\{\bar{1}12\}\langle110\rangle$	$\blacksquare$	$\{1\bar{1}\bar{2}\}\langle\bar{1}\bar{1}0\rangle$
$C$	$\circ$	$\{110\}\langle110\rangle$		
$Bs$	$\diamond$	$\{0\bar{1}1\}\langle\bar{2}11\rangle$	$\blacklozenge$	$\{01\bar{1}\}\langle2\bar{1}\bar{1}\rangle$
$A$ -fibre		$\{111\}\langle uvw\rangle$		
$B$ -fibre		$\{hkl\}\langle110\rangle$		

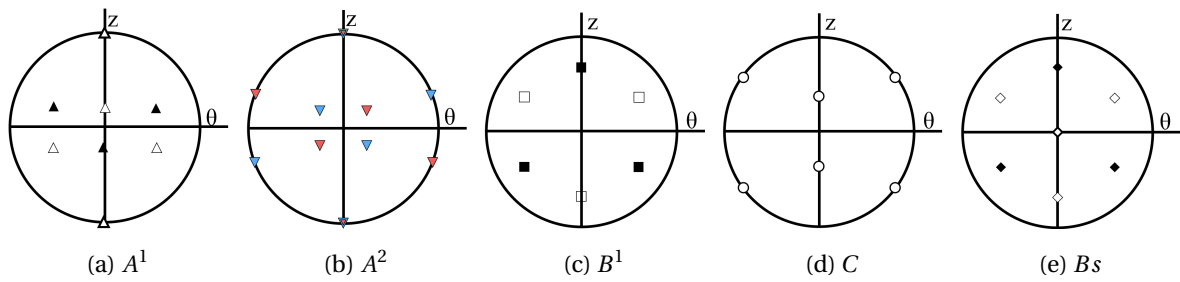


Figure 2.9: Schematic ideal texture components (from Table 2.1) for torsion deformed aluminium, illustrated in  $\{111\}$ -pole figures. Figure adapted from Montheillet *et al.* (1984) [21, 9].

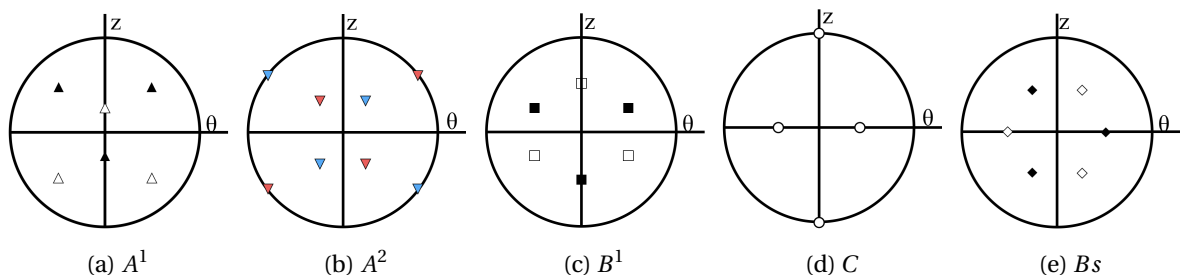


Figure 2.10: Schematic ideal texture components (from Table 2.1) for torsion deformed aluminium, illustrated in  $\{200\}$ -pole figures. Figure adapted from Pettersen (1999) [5].

The experiments revealed that torsion of aluminium in room temperature with small strains

(0.62) resulted in a dominant  $A^1$ -orientation. With increased strain the  $A^1$ -orientation decreased in intensity and the C-component increased. In effort of finding the steady state textures warmer torsion tests at 200°C and with strain of 5.58 were conducted. Montheillet *et al.* (1984) found that the texture consisted mainly of the C-component, with indications of  $B^1$ . At 300°C and a strain of 10.54 the  $B^1$ -component dominated the texture with little of the C-component remaining. At 350°C and a strain of 31 the  $B^1$ -component dominated the texture. At 400°C and a strain of 31 the  $B^1$ -component increased in intensity. All these experiments were quenched immediately after torsion.

Lastly, Figure 2.11 presents a schematic illustration of the ideal texture components from Table 2.2 in an ODF for  $\varphi_2 = 0^\circ$  and  $\varphi_2 = 45^\circ$ , with  $\Phi[0, 90]$ ,  $\varphi_1[0, 360]$  [23].

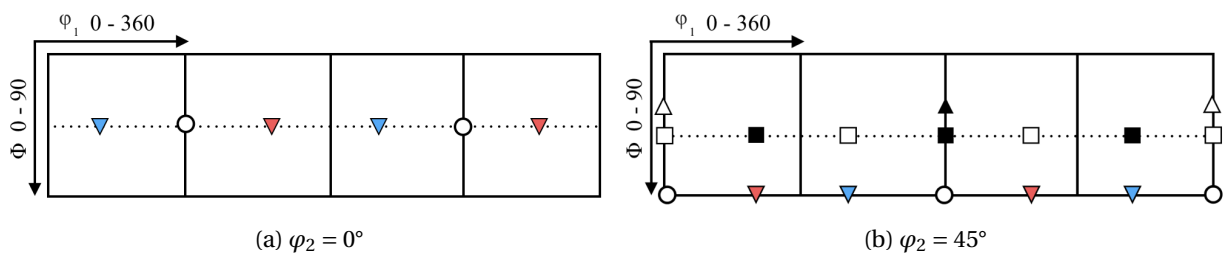


Figure 2.11: Schematic ideal texture components (from Table 2.1) illustrated in an ODF for (a)  $\varphi_2 = 0^\circ$  and (b)  $\varphi_2 = 45^\circ$ . Figure adapted from Panigrahi *et al.* (2014) [22, 23, 24, 25, 26].

### 2.3.1.2 Annealed Torsion Texture

Kassner *et al.* (1989) did a series of low strain rate (0.2/s) hot torsion experiments at 400°C in order to investigate aluminums developing texture. He only observed the  $A^1$ -,  $B^1$ - and C-component in these experiments and found that the different texture components intensity varied with grain size and strain. The results are presented in Table 2.2 [5, 9].

Table 2.2: Torsion textures of pure (99.7%) aluminium at 400°C (not quenched) with a strain rate of 0.2/s. S: strong intensity, M: medium intensity, W: weak intensity and W-: weaker intensity. Results taken from Kassner *et al.* (1989) [9].

Strain	Grain size (mm)	$A^1$	$B^1$	$C$
3	0.1	M	M	S
3	2	W-M	M-W	M
10	0.1	W	M	W
10	2	W	S-M	W
20	0.1	W-	S	W-
20	2	W	S	W
40	0.1	W-	S	W-
40	2	W	S	W
60	0.1	W-	S	W-
60	2	W	S-M	M-W

Pettersen (1999) investigated recrystallisation torsion texture in (non dispersoid containing) AA6060 and (dispersoid containing) AA6082. She found that the  $Bs$ -component plays a significant role during annealing of a deformed material. At small strains ( $\epsilon = 1$ ) it was found two different  $Bs$ -orientated regions: elongated bands in the shear direction and groups of subgrains not associated with bands [5].

At higher strains the  $Bs$ -orientated grains were only found in single subgrains or in groups of subgrains. The adjacent area was found to be  $B^1$ -orientated, with a gradual orientation change towards the  $Bs$ -orientation [5].

The characteristic recrystallisation component for annealed torsion texture is the  $Bs$  component, which is rotated 30° around the  $\langle 111 \rangle$ -axis of the  $B^1$  component. The  $Bs$  texture component was observed for deformed samples at a  $Z$ -value of  $7 \cdot 10^{11}$  after annealing experiments at 480°C for 21 seconds. It was observed that  $Bs$ -subgrains acted as nucleation sites, as a result of their misorientation [5]. Thus, the  $Bs$ -orientated subgrains is of interest when analysing the microstructure.

### 2.3.1.3 Simulated Torsion Texture

Torsion (shear) texture can be predicted using texture models such as the Alamel-model and the FC-Taylor-model. A description of these models is given by Zhang *et al.* (2015) in [28]. The Alamel-model and the FC-Taylor-model are statistical aggregate models, meaning they only show a the statistical selection of grain orientations.

Assuming a random initial texture the simulated texture by the Alamel-model is given in Table 2.3 and by the FC-Taylor model is given in Table 2.4. These simulated textures are comparable with experimental texture, however simulated texture component intensities are not as they can be three times stronger than measured intensities.

Table 2.3: Generated ODF sections with the Alamel-model of  $\varphi_2 = 0^\circ$  and  $\varphi_2 = 45^\circ$  with contour maps with intensities of 1.5/6/12/18/24/31/40. The components are given i Table 2.1.




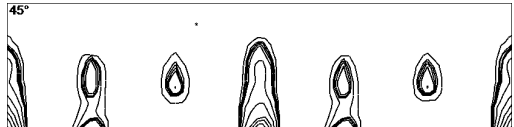
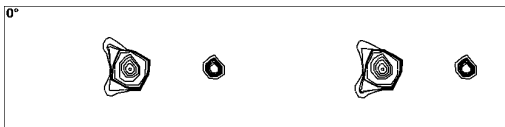



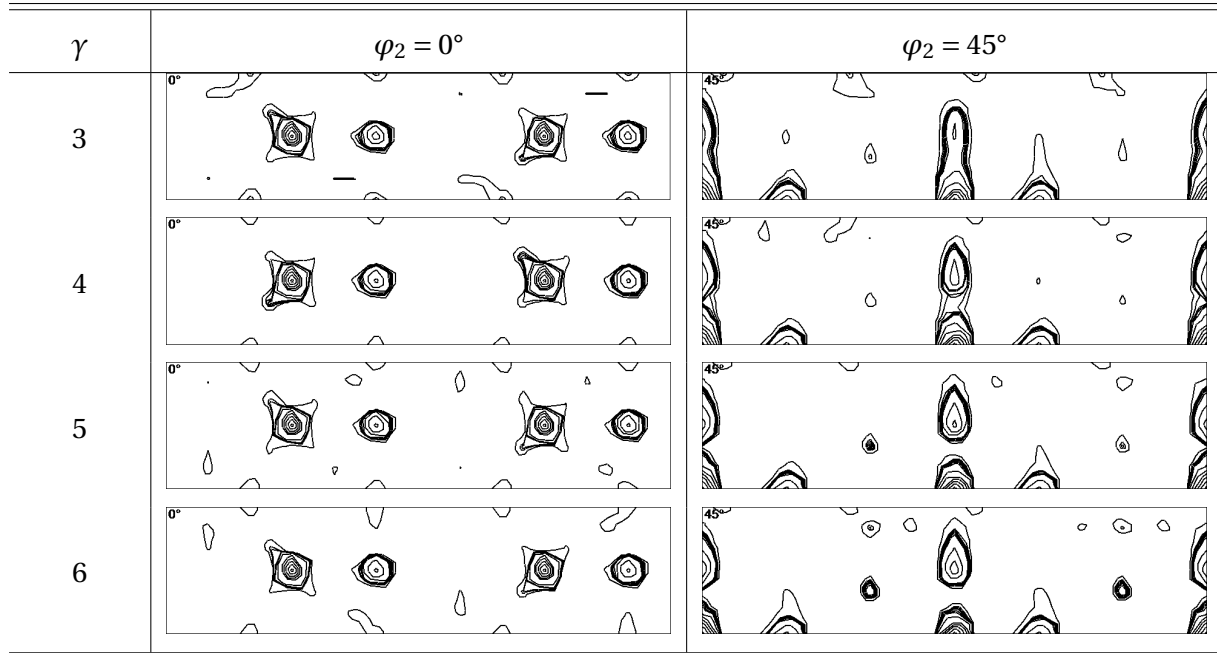
$\gamma$	$\varphi_2 = 0^\circ$	$\varphi_2 = 45^\circ$
3		
4		
5		
6		

Table 2.4: Generated ODF sections with the FC-Taylor-model of  $\varphi_2 = 0^\circ$  and  $\varphi_2 = 45^\circ$  with contour maps with intensities of 1.5/6/12/18/24/31/40. The components are given i Table 2.1



## 2.4 Experimental Techniques

In this work several methods of investigation (electron backscatter diffraction and X-Ray diffraction) and controlling of the torsion (the torsion machine and PID temperature regulation) for each sample are used. This chapter aims to explain these methods and how they are used in this work.

### 2.4.1 Electron Backscatter Diffraction

The Electron backscatter diffraction (EBSD) technique is utilised in this investigation in order to measure subgrain sizes. To obtain the diffraction pattern electrons are beamed onto a sample, tilted at angle of  $70^\circ$ . The diffracted electrons from the sample fulfilling Bragg's law<sup>1</sup> collides with a screen, generating the diffraction pattern. This is illustrated in Figure 2.12 [29].

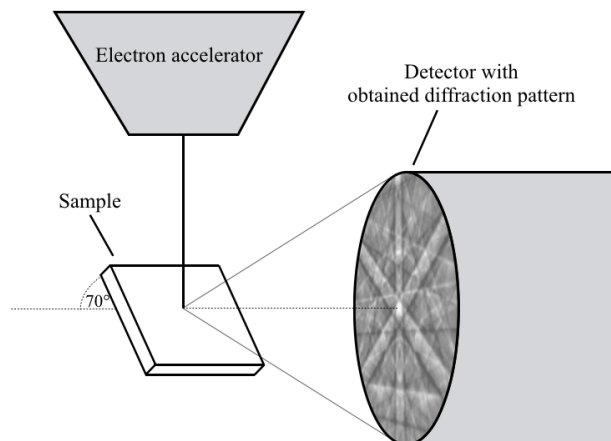


Figure 2.12: Schematic illustration of the caption of the diffraction pattern from a sample.

The pattern obtained by the detector is used to determine the crystallographic orientations for a defined area of the samples surface. When the pattern is acquired further indexing (using *EDAX Orientation Imaging Microscopy™ (OIM) Data Collection* in this work) is needed before specimen analysis.

<sup>1</sup>  $n\lambda = 2d_{hkl}\sin\theta$ , where  $n$  is the order of diffraction peak,  $\lambda$  is the wavelength of the X-ray,  $d_{hkl}$  is the inter-plane distance and  $\theta$  is the scattering angle [29].

*EDAX OIM™ Analysis* is used to analyse the obtained microstructure. OIM identifies grains by grouping sets of connected and similarly oriented points into *grains*. Each neighbouring point to a *grain* within a tolerance angle are added to the *grain*. This algorithm is not developed to differentiate subgrains from grains, even though the tolerance angle can be set very low, e.g. 1°. To properly identify subgrains and subgrain size an other method is used: line intercept on Image Quality (IQ)-maps. An IQ-map illustrates how well every point in a scan fits a crystallographic orientation (aluminium crystal in this work). Every point is then coloured in a grey scale, where light colours indicate a good fit and vice versa. Boundaries have poor fit and are dark in colour. An IQ-map can be used to investigate the Grain Orientation Spread (GOS) across a line in the map. The GOS is a measurement of the spread of crystallographic orientations within a defined area. In this work GOS is measured from point-to-point between any two points in a scan, giving a graph of the change in orientation across the line. The point-to-point method is particularly useful for manually determining subgrain and grain boundaries, as the delta angle between every point is shown, making subgrain and grain boundaries of any magnitude visible. Point-to-point can also be used for line intercept measurement for measuring the average subgrain size ( $\bar{\delta}$ ). Two other ways, that work on the same principle, is to measure the point-to-origin and the image quality for a line in the scan. The point-to-origin metode shows the misorientation in relation to the starting point, making it easy to see the orientation gradient in the microstructure, as they appear as tilted lines. By combining these techniques the average subgrain density can be determined with great certainty.

Recrystallised grains are deformation free volumes (§2.2.1), which have little to none GOS. Investigating the GOS for the samples in addition to a texture analysis will also give a good indication on whether the sample is recrystallised or not.

#### **2.4.2 X-Ray Diffraction**

The X-Ray Diffraction (XRD) technique is used to obtain texture from the samples, giving a qualitative representation of each samples texture. Advantages with XRD is the large penetration depth ( $5\mu m$ ) and the large spatial resolution ( $5\mu m - 1mm$ ) [30], allowing a relative large number of grains (tens of thousands) to be analysed in one scan, meanwhile EBSD only gives information



on the scanned grains. The large analysed area gives a good statistical representation of each samples' texture. To obtain a samples texture X-rays are beamed onto the sample. The diffracted X-rays fulfilling Bragg's law<sup>1</sup>, while the diffraction angle ( $n\lambda$ ) is fixed while varying the tilt angle and the rotation angle, are measured using *Bruker AXSs Diffrac Plus ARD Commander*. The measured intensities then are corrected for defocusing and background noise. Three measured pole figures are needed to calculate a samples ODF and to calculate the complete pole figures. The corrected registered intensities and angles of the diffracted X-rays are then used to calculated the pole figures and ODF [29, 31].

### 2.4.3 The Torsion Machine

The torsion machine (Figure 2.13) is a hydraulic driven special made machine, located at NTNU. It is driven by a hydraulic motor, and was recalibrated for operating pressure of 90 bar at the start of this work. The motor is at the very left in Figure 2.13, connected to a optical counting device measuring the actual angular velocity. The motor is followed by a gear (1 : 19.56) underneath the blue shield (upright position), which is connected to a stabilisation and cooling module.

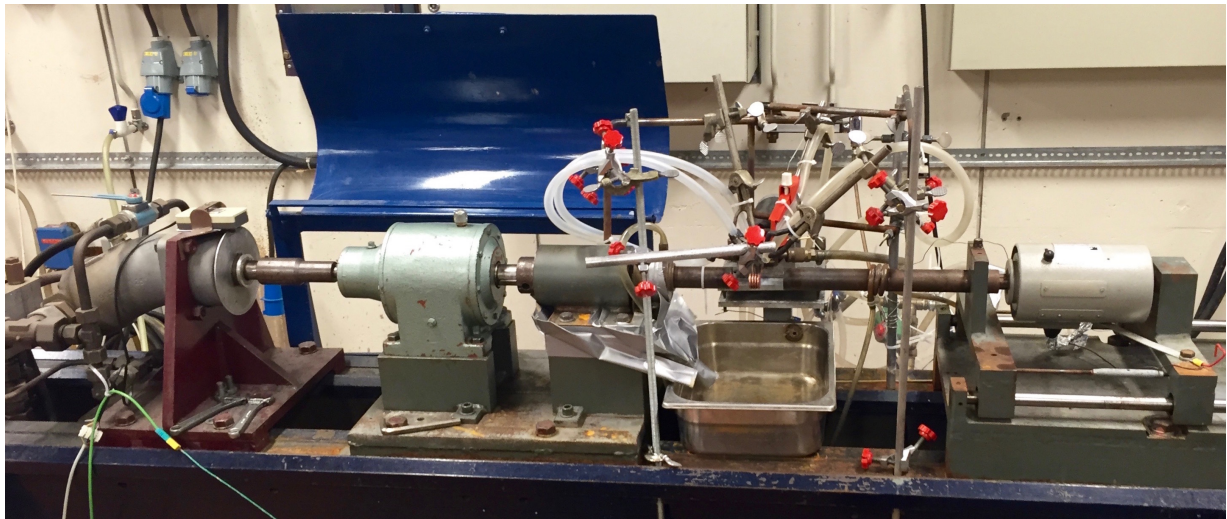


Figure 2.13: The torsion machine.

The torsion sample is directly mounted after the stabilisation module, followed by a copper cooling coil between the sample and the torque meter. Figure 2.14 shows how the torsion sample

is mounted. The sample is bolted with two screws on both sides, with the induction heating coil at the centre of the sample. The thermocouple for temperature regulation is within the right mount and right part of the torsion sample. Four water pipes of the equal length and height, are aimed towards the sample, giving it a thorough quench.

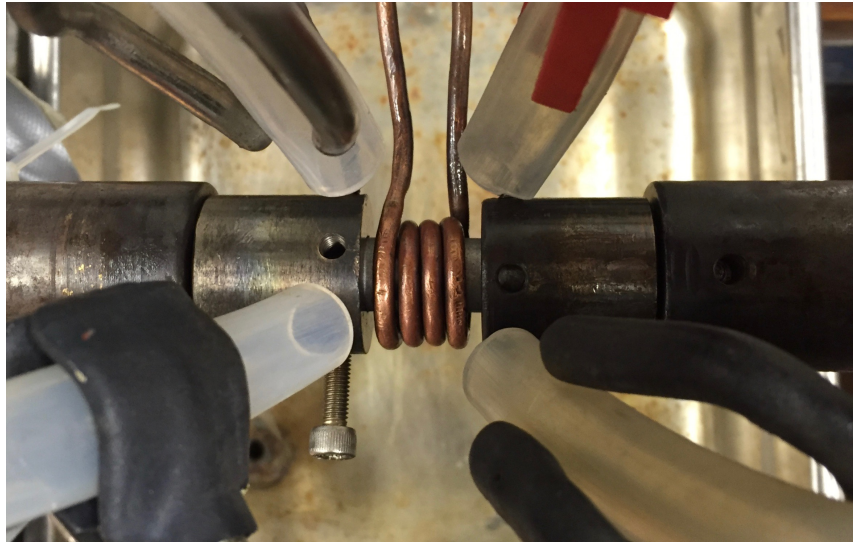


Figure 2.14: The fixture of the torsion sample.

The machine is programmed in *National Instruments LabVIEW 2011*. Prior to the experiments the original code was modified to include change of angular velocity during torsion. This was done by defining a first and second setpoint for angle of twist, and continuously checking if the first measured angle of twist was equal the first setpoint. When the measured angle of twist reached the first setpoint, the setpoint was switched to the second setpoint with the second angular velocity. The torsion machines angular velocity is based on voltage, as the machine is changing angular velocity it changes the voltage to the hydraulic motor.

Due to the delay between the signal sent for opening the quenching valve until the water reaches the sample, a new "Water Timing" variable was introduced to the program. This variable calculated a new smaller setpoint, than the second setpoint, on which the quenching signal is initiated before the torsion is ended. This variable was calibrated to a accuracy of  $\frac{1}{240}sec$ , quenching the sample immediately after torsion.

### 2.4.3.1 Proportional Integral Derivative Control

During torsion the sample is externally cooled by the sample mount on the torsion machine. As the sample is constantly cooled, it need to be constantly heated in order to maintain a set temperature. In order to properly control the temperature during torsion a Proportional Integral Derivative (PID) controller is used to constantly regulate the sample temperature.

A PID controller continuously calculates the difference between a given setpoint  $u(t)$  and a measured variable  $y(t)$ , and returns an error value  $e(t)$ . This error value is added to the output signal, correcting it, to minimise the error over time. The PID controller mechanism (Figure 2.15) consists of a Proportional ( $K_p$ ), Integral ( $K_i$ ) and Derivative element ( $K_d$ ) [32].

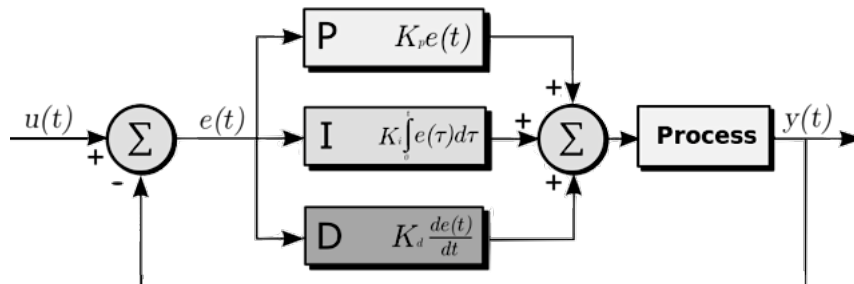


Figure 2.15: Schematic illustration of the PID controller mechanism. Figure adapted from Zahra (2016) [32]

### 3 Material and Experiments

The following section presents the material used in this work, the experimental method explained in detail and the development of the experimental plan.

#### 3.1 The AA6063 material

The Aluminium Alloy 6000-series are alloyed with Mg and Si and is an series with two-phases alloys, where  $Mg_xSi_y$  particles are precipitated. The alloy elements (Table 3.1) affects the alloys maximum extrusion speed (strain rate) before tearing. A higher content of Mg and Si will lower the maximum extrusion speed due to tearing from particle hardening [12, 33].

Table 3.1: The alloy elements in AA6063 given in weight procent [34, 35].

	Si	Fe	Cu	Mn	Mg	Cr	Zn	Ti	Ga	Sn
Generic alloy	0.20-0.60	0.35	0.10	0.10	0.45-0.90	0.10	0.10	0.10	0.02	0.01
Studied alloy	0.401	0.096	0	0.017	0.500	0	0	0.010	0.012	0

In present work, all samples are made of heterogeneous AA6063. The studied alloys chemical composition is presented in Table 3.1. The samples were from an casted homogenised extrusion ingot produced the Sapa Group. The used material contains little to no dispersoids (Mn, Cr and/or Zr), as shown in Table 3.1 [36].

The average grain size for the samples was measured using optical microscopy with linear interception, to be  $88 \mu m \pm 5 \mu m$ . The samples were produced using a water jet to cut cylinders from a billet. The cylinders were then lathed to dimensions (shown in Figure 2.1) and a temperature measuring opening for PID-regulation was drilled.

### 3.2 Method

Initially, the torsion machine was modified to better control the quenching and different torsion speeds (see §2.4.3).

After torsion, the upward facing sample surface was marked, as the uppermost point if the surface achieves the most accurate quenching. The samples' side pieces were cut off and their core drilled out, leaving a hollow cylinder with  $\sim 1\text{ mm}$  wall thickness for each sample, as illustrated in Figure 3.1a. The samples were then cut in half along the axial direction, leaving two half cylinders (top and bottom sides) as shown in Figure 3.1b. Using a hydraulic press the top half cylinder of each sample were pressed flat, straitening the samples out without compressing them. Figure 3.1c shows a sample in relation to the torsion axis.

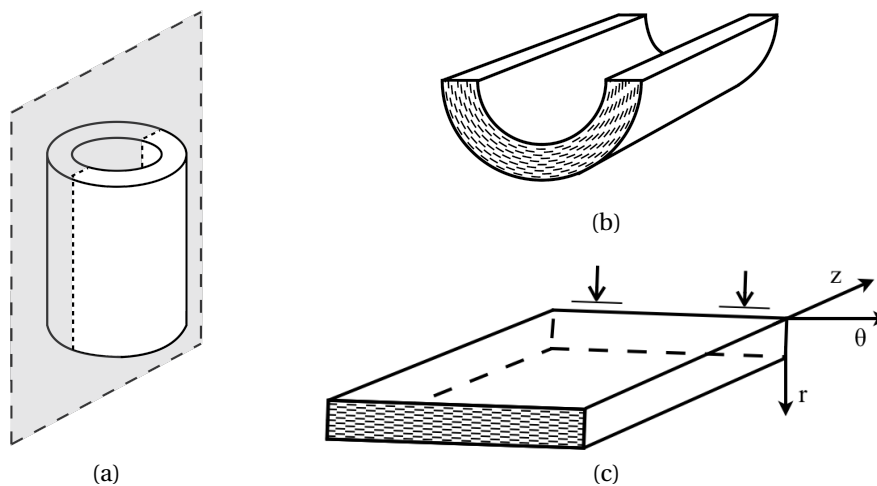


Figure 3.1: Sample preparation of torsion sample. (a) Removal of core. (b) Cut into a half cylinder (c) Flattening of sample with use of a hydraulic press.

The samples were then mounted in a specimen holder embedded with Epofix™ Cold-Setting Resin with the surface (r-direction) side facing outwards from the mold, and left to harden overnight. After hardening, the samples were sanded with SiC#2000, then SiC#4000, then polished at  $3\mu\text{m}$  and  $1\mu\text{m}$ . Sanding and polishing was done stepwise and the samples were rotated  $90^\circ$  until no earlier abrasive lines were visible. Using a fine saw the samples were cut out of the embedding epoxy. Remaining epoxy residue was carefully removed using a set of tweezers. Then

the samples' were electropolished, using parameters shown in Table 3.2.

Table 3.2: Parameters for electropolishing.

Parameter	Value
Electrolyte	A2
Temperature	-30°C
Time	20 sec
Voltage	31 V

The samples' microstructures were then studied using EBSD (parameters presented in Table 3.3). The EBSD data were then processed in *EDAX Orientation Imaging Microscopy™(OIM) Data Collection*. In addition to this, the samples' texture were then captured using XRD, for a quantitative representation of each samples texture. The diffraction signal intensity was recorded using *Bruker AXS DiffracPlus: TexEval* and corrected for defocusing and background noise. The XRD machine was set to have a spatial resolution with a diameter of  $0.8\text{mm}$ . The samples' texture were calculated with monoclinic sample symmetry with a harmonic expansion rank of 22, and the samples were rotated at an angle of 90 degrees (to correct for the observation angle used in the XRD).

Table 3.3: Parameters for EBSD

Parameter	Value
Voltage	$20\text{kV}$
Aperture	$300\mu\text{m}$
Working distance	$25\text{mm}$
Angle of tilt	$70^\circ$
Magnification	$300x$
High current mode	Enabled

It was carried out four reference experiments at (Ref.1) 350°C, (Ref.2) 375°C, (Ref.3) 400°C and at (Ref.4) 400°C without quenching, at the maximum angular velocity ( $7.35\text{rad/s}/\dot{\epsilon} = 4.241/\text{s}$ ) for a shear strain of 3.14 (reaching steady-state deformation,  $\epsilon = 1.81$ ), then immediately quenched, to check the equipments ability to capture the steady-state deformation microstructure. To determine the highest temperature the quenching mechanism was effective at, the average subgrain density, as well as the different texture components intensities, were investigated. The average subgrain size ( $\bar{\delta}$ ) was measured using line intercept, with GOS point-to-point for manually determining grain boundaries, in the direction normal to the sense of shear (shown in Figure 4.1b). The average subgrain size was measured in this direction due to the grain elongation parallel to the sense of shear, and because the subgrain density will be highest normal to the grain elongation. The grain elongation is about  $5.2 - 7.4x$  depending on sample, calculated from Formula 7 and the experimental plan in Table 3.4.

### 3.3 Experimental Plan

It was found that the quenching mechanism sufficiently quenched samples at temperatures up to  $375^{\circ}\text{C}$ , as the subgrain size was found to be equal to experiment Ref.1 and orientation gradients were observed in the metal, suggesting a deformed state. At  $400^{\circ}\text{C}$  subgrain growth was observed suggesting that recovery had occurred. Orientation gradients were also observed for this temperature, but due to the subgrain growth it was decided to proceed at  $375^{\circ}\text{C}$ . Another reference experiment (Ref.5) was therefore conducted at  $375^{\circ}\text{C}$ . Ref.5 was kept at  $375^{\circ}\text{C}$  for 120 seconds after torsion as a reference to the annealed texture under equal parameters. The experimental plan is illustrated in Figure 3.2 and presented in Table 3.4.

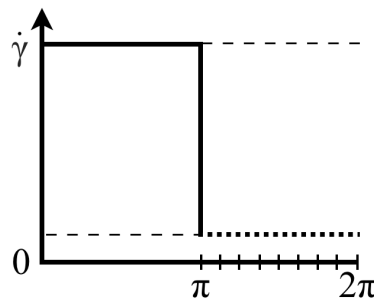


Figure 3.2: Illustration of the experimental plan.

The two different angular velocities  $7.35\text{rad/s}$  ( $\dot{\gamma} = 7.35\text{1/s}$ ,  $\dot{\epsilon} = 4.24\text{1/s}$ ) and  $2.8 \cdot 10^{-5}\text{rad/s}$  ( $\dot{\gamma} = 2.8 \cdot 10^{-5}\text{1/s}$ ,  $\dot{\epsilon} = 1.62 \cdot 10^{-5}\text{1/s}$ ) gives respectively Zener–Hollomon parameters of  $3.33 \cdot 10^{13}$  and  $1.27 \cdot 10^8$ , calculated using an activation energy of  $160\text{KJ/mol}$  and temperature of  $375^{\circ}\text{C}$ . Using the software *HyperXtrude* for extrusion simulations, it is shown in Figure 3.3 that these Z-values are approximately equivalent to a particle traveling at a radius of  $1.425\text{mm}$  in a aluminium profile with a radius of  $1.5\text{mm}$  at  $450^{\circ}\text{C}$  [37]. A comparison of the Z-values in relation to the simulated extrusion is plotted in Figure 3.3. It is seen from the figure that  $Z = 3.33 \cdot 10^{13}$  is approximately equal to the Z-value the particle experiences at the extrusion die. The simulation is terminated before the Z-value drops to zero as the particle is not being deformed any longer. The Z-value of  $1.27 \cdot 10^8$  is approximately equal to the Z-value the particle experiences right after the extrusion die, before deformation has completely ended.



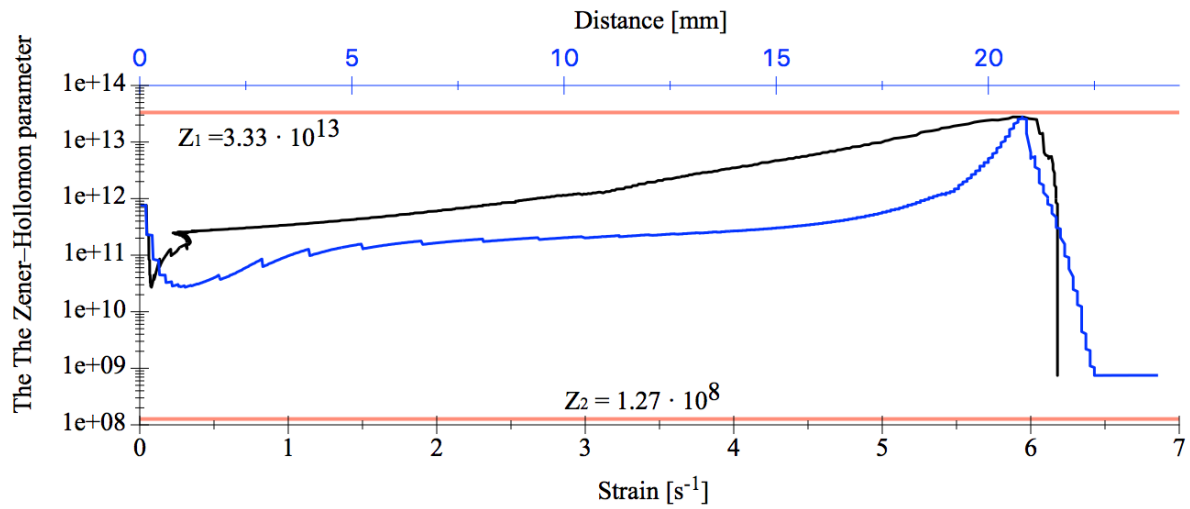


Figure 3.3: Illustration of the Z-values in relation to a HyperXtrude extrusion simulations for a particle traveling at a radius of  $1.425\text{mm}$  in a aluminium profile with a radius of  $1.5\text{mm}$ . Adapted from Zhang (2016) [37].

Table 3.4: The experimental plan. Each sample undergoes a 1<sup>st</sup> and a 2<sup>nd</sup> angle of twist ( $\theta_{1,2}$ ), with different angular velocities ( $\omega_{1,2}$ ). NQ means not quenched.

Sample	Temp. [°C]	$\omega_1$ [rad/s]	$\theta_1$ [rad]	$\omega_2$ [rad/s]	$\theta_2$ [rad]
Ref.1	350	7.35	$2\pi$	0	0
Ref.2	375	7.35	$2\pi$	0	0
Ref.3	400	7.35	$2\pi$	0	0
Ref.4 NQ	400	7.35	$2\pi$	0	0
Ref.5 RX	375	7.35	$2\pi$	0	0
0 – 4.71	375	0	0	$2.8 \cdot 10^{-5}$	4.7
0 – $\pi$	375	0	0	$2.8 \cdot 10^{-5}$	$\pi$
0 – $\pi$ NQ	375	0	0	$2.8 \cdot 10^{-5}$	$\pi$
$\pi$ – 1.4	375	7.35	$2\pi$	$2.8 \cdot 10^{-5}$	1.4
$\pi$ – 0.7	375	7.35	$2\pi$	$2.8 \cdot 10^{-5}$	0.7
$\pi$ – 0.5	375	7.35	$2\pi$	$2.8 \cdot 10^{-5}$	0.5
$\pi$ – 0.44	375	7.35	$2\pi$	$2.8 \cdot 10^{-5}$	0.45
$\pi$ – 0.34	375	7.35	$2\pi$	$2.8 \cdot 10^{-5}$	0.35
$\pi$ – 0.26	375	7.35	$2\pi$	$2.8 \cdot 10^{-5}$	0.25
$\pi$ – 0.18	375	7.35	$2\pi$	$2.8 \cdot 10^{-5}$	0.2
$\pi$ – 0.14	375	7.35	$2\pi$	$2.8 \cdot 10^{-5}$	0.15
$\pi$ – 0.13	375	7.35	$2\pi$	$2.8 \cdot 10^{-5}$	0.1
$\pi$ – 0.03	375	7.35	$2\pi$	$2.8 \cdot 10^{-5}$	0.05
$\pi$ – 0	375	7.35	$2\pi$	0	0

## 4 Experimental Results

In the following section the results from the EBSD and XRD analysis are presented. The average subgrain size as a function of the 2<sup>nd</sup> shear strain is presented, as well as the ODF texture for  $\varphi_2 = 0^\circ$  and  $\varphi_2 = 45$  in addition to the samples {111}- and {200}-pole figures.

Each sample is given a Sample ID consisting of two parts, the 1<sup>st</sup> and 2<sup>nd</sup> shear strain separated with a hyphen, i.e. Sample  $\pi - 0.7$  has the 1<sup>st</sup> shear strain of 3.14 and the 2<sup>nd</sup> shear strain of 0.7. The samples' shear strain and strain are presented in Table 4.1.

Table 4.1: The samples shear strain and strain.

Sample	$\gamma_1$	$\gamma_2$	$\gamma_{tot}$	$\epsilon_2$	$\epsilon_{tot}$
Ref.1	3.14	0	3.14	0	1.8
Ref.2	3.14	0	3.14	0	1.8
Ref.3	3.14	0	3.14	0	1.8
Ref.4 NQ	3.14	0	3.14	0	1.8
Ref.5 RX	3.14	0	3.14	0	1.8
0 – 4.71	0	4.71	4.71	2.72	2.7
0 – $\pi$	0	3.14	3.14	1.815	1.8
0 – $\pi$ NQ	0	3.14	3.14	1.815	1.8
$\pi$ – 1.4	3.14	1.4	4.54	0.81	2.6
$\pi$ – 0.7	3.14	0.7	3.84	0.405	2.2
$\pi$ – 0.5	3.14	0.5	3.64	0.29	2.1
$\pi$ – 0.44	3.14	0.435	3.575	0.25	2.1
$\pi$ – 0.34	3.14	0.335	3.475	0.195	2.0
$\pi$ – 0.26	3.14	0.255	3.395	0.145	1.96
$\pi$ – 0.18	3.14	0.175	3.315	0.10	1.9
$\pi$ – 0.14	3.14	0.135	3.275	0.08	1.9
$\pi$ – 0.13	3.14	0.125	3.265	0.07	1.88
$\pi$ – 0.03	3.14	0.025	3.165	0.015	1.83
$\pi$ – 0	3.14	0	3.14	0	1.8

## 4.1 Average Subgrain Size

The red lines in the Image Quality-map in Figure 4.1b illustrates how the average subgrain size ( $\bar{\delta}$ ) was measured using line intercept on Sample  $\pi - 0.13$  in the direction normal to the sense of shear (identified with the samples Inverse Pole Figure (IPF)-map in Figure 4.1a), measuring between 200-500 subgrains per sample. In Appendix B the IPF-maps and Image Quality (IQ)-maps are presented for all samples.

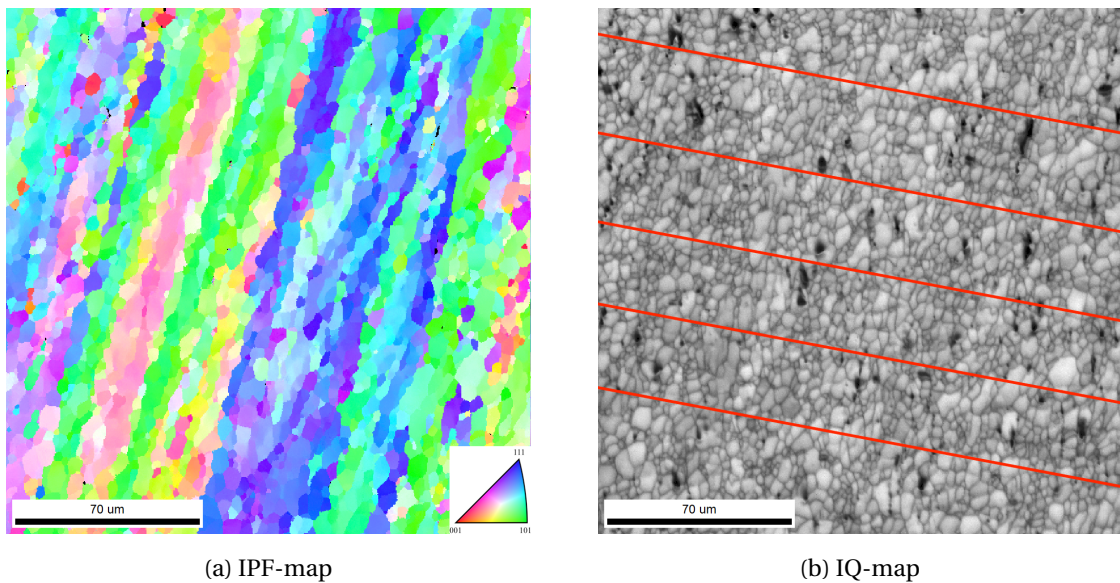


Figure 4.1: An illustration of the line intercept measuring-lines in relation to the sense of shear. Both maps are presented with the horizontal direction in the  $z$  direction and the vertical direction in the  $\theta$  direction in relation to the torsion samples.

The subgrain size was calculated using the traditional line intercept method, with the point-to-point (ptp)-method (§2.4.1). Figure 4.2 illustrates the output data from a ptp-line used for subgrain boundary counting. The red line in Figure 4.2 is the threshold value for measurement noise, specifically chosen for each sample (often equal to  $1^\circ$  misorientation) depending on background noise in the scan. All ptp-tops above the threshold are counted as subgrain boundaries, as a sudden change in misorientation only occurs in a boundary. By counting subgrains in this manner; all grains are interpreted as subgrains. The point-to-origin (pto)-method was used to confirm the ptp-readings.

During torsion the grains are elongated with the shear strain, parallel to the sense of shear, thus the subgrain density is highest normal to the sense of shear. Hence the subgrain size measurements were taken normal to the sense of shear.

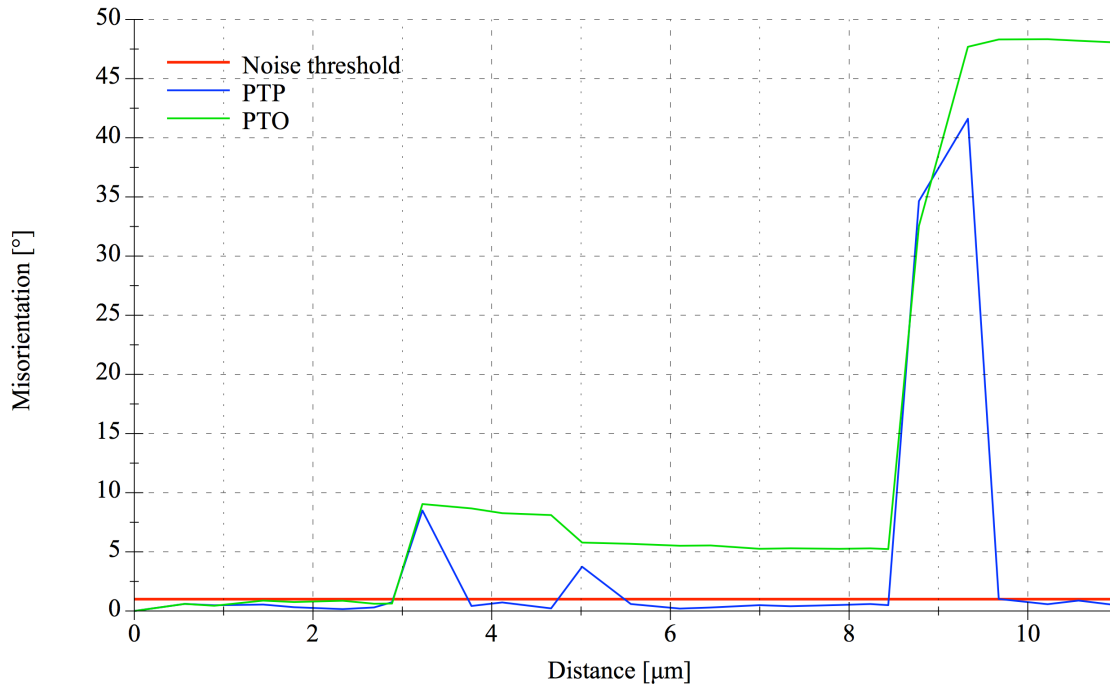


Figure 4.2: The line intercept subgrain boundary counting method. Graph of a smaller area of  $11\mu\text{m}$  with three identified subgrain boundaries.

The average subgrain size for each sample are plotted with their corresponding standard deviation in Figure 4.1. The graph shows how the subgrain size increases with the 2<sup>nd</sup> shear strain until a shear strain of 0.26 is reached, then stabilising between  $5 - 6\mu\text{m}$ . The data used in the plot are presented in Appendix C.

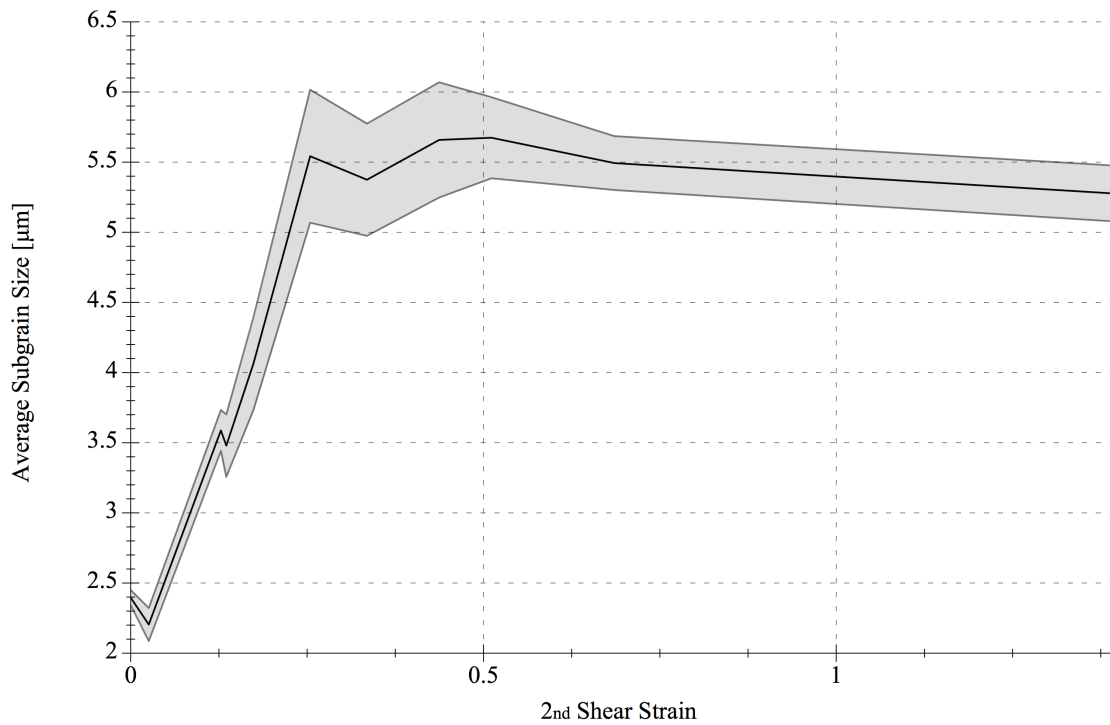
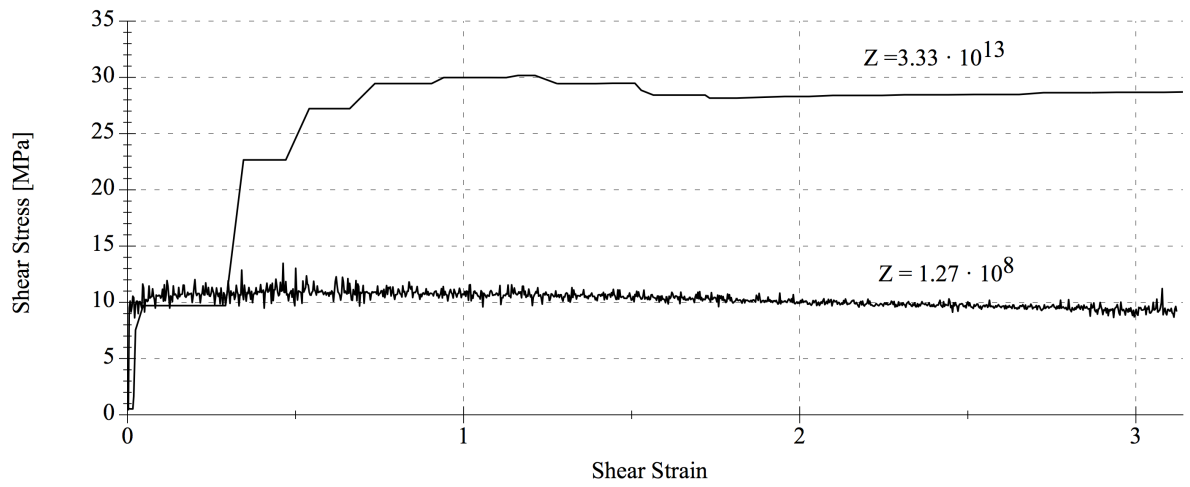


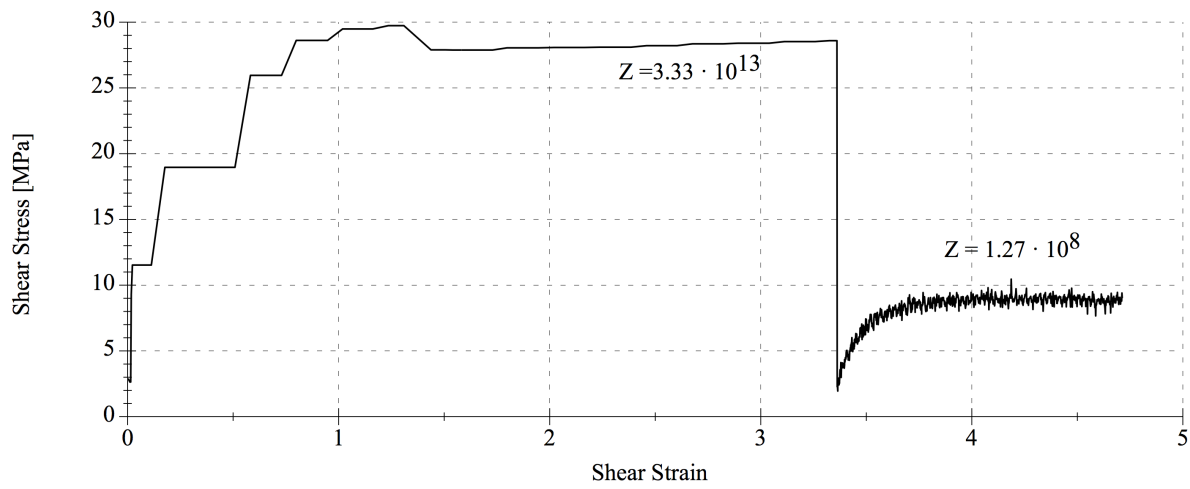
Figure 4.3: The average subgrain size as a function of the 2<sup>nd</sup> shear strain, with the standard deviation marked in grey.

## 4.2 Measured stress

During torsion the stress was recorded. Figure 4.4 presents stress-shear-strain curve for the two different  $Z$ -values, confirming steady-state flow stress for both  $Z$ -values. It can be seen that the resolution in the measurements for  $Z = 3.33 \cdot 10^{13}$  is poor, this is due to a too low measuring frequency for the high strain rate.



(a)



(b)

Figure 4.4: (a) 1<sup>st</sup> steady-state stress-shear-strain curve, and (b) 1<sup>st</sup> and 2<sup>nd</sup> steady-state stress-shear-strain curve. The curves have been calculated from the torque vs. angle of twist by assuming the temperature and the strain rate are constant for the two different  $Z$ -values,  $p = q = 0$ , and the geometry of the samples are constant during torsion.



### 4.3 Texture

In Figure 4.5 the complete ODF ( $\varphi_2 = 0^\circ, 5^\circ, \dots, 90^\circ$ ) for Sample  $\pi - 0$  is presented. All samples' ODFs are presented in Appendix E with contour maps of equal density distribution for easy comparison of the samples. In the following presentation of the samples ODFs, only the sections of  $\varphi_2 = 0^\circ$  and  $\varphi_2 = 45^\circ$  are presented in Table 4.2.

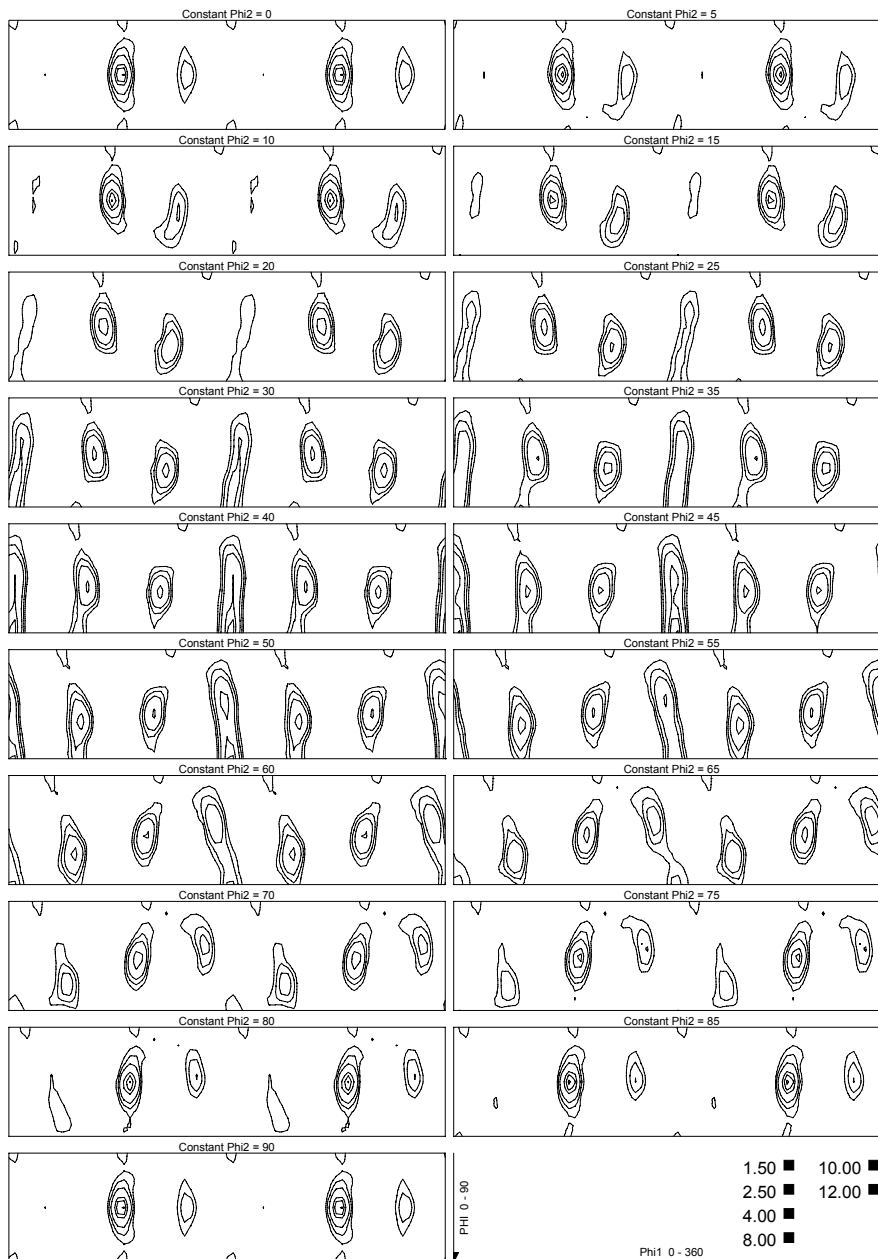
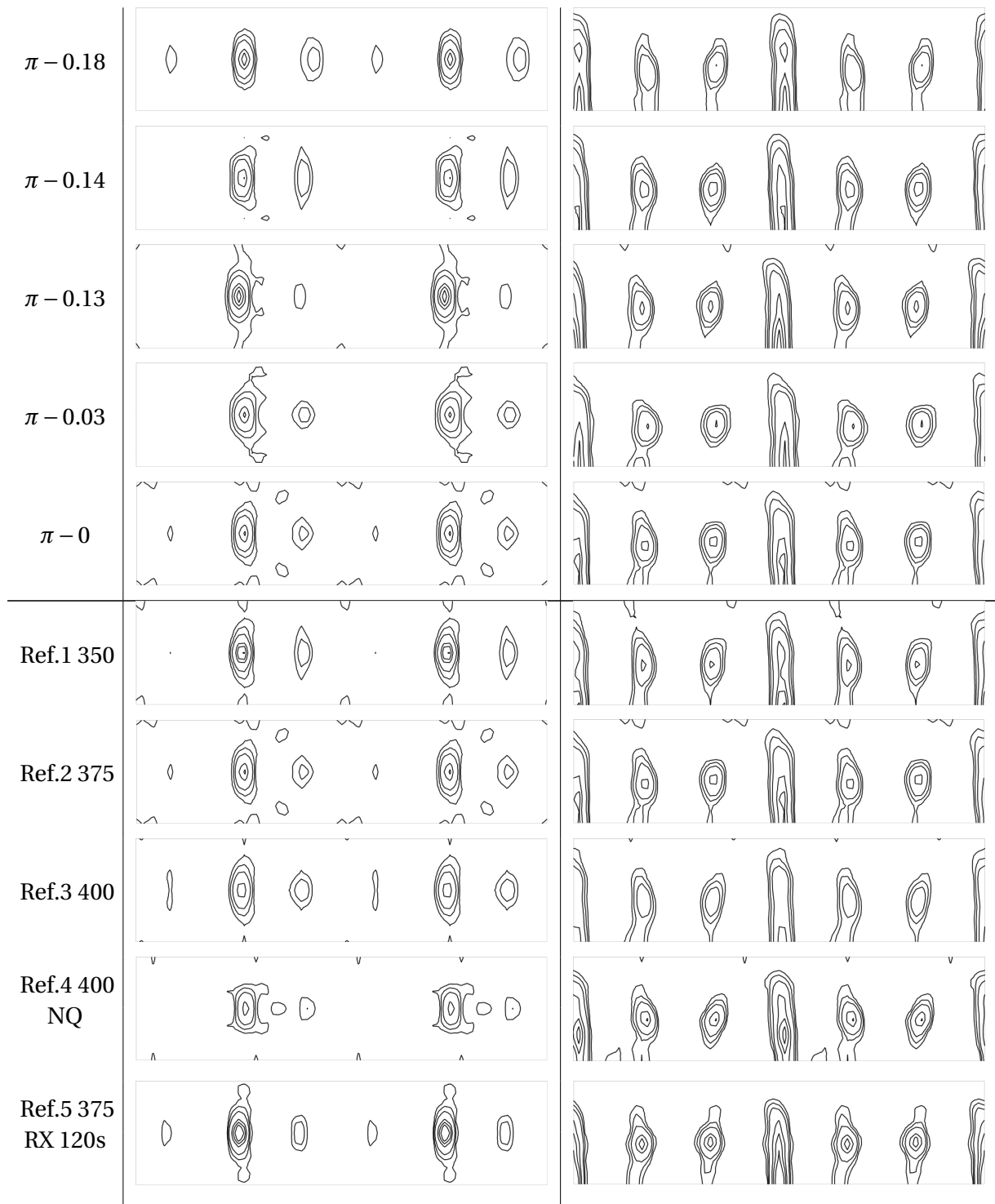


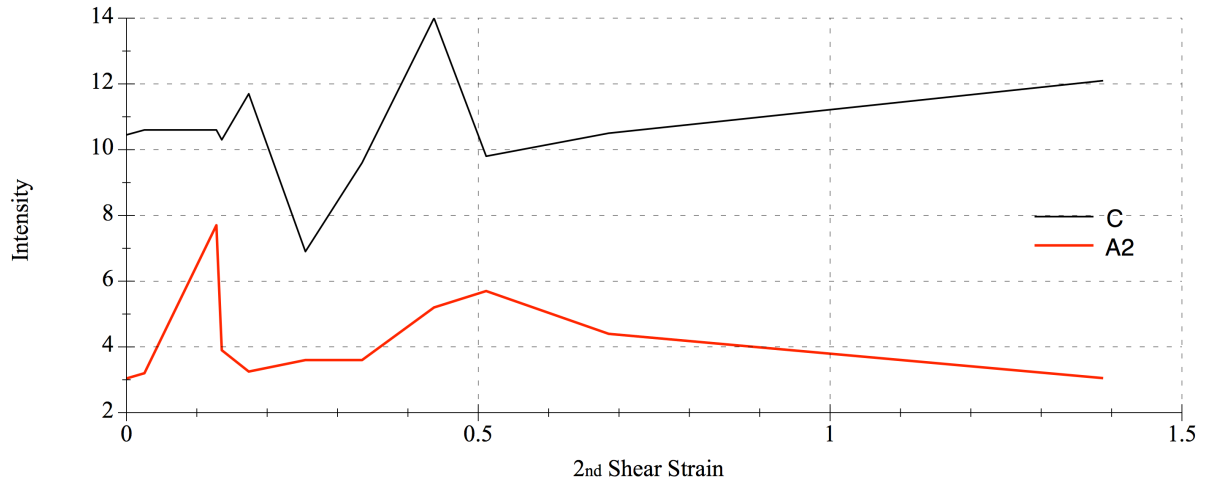
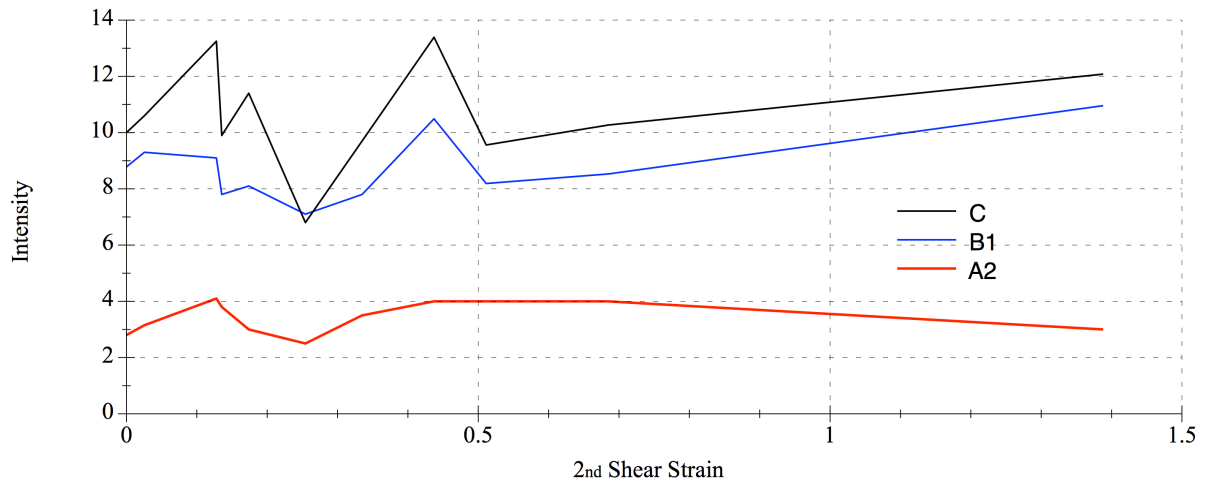
Figure 4.5: XRD obtained ODF for Sample  $\pi - 0$ .

Table 4.2: The ODF sections of  $\varphi_2 = 0^\circ$  and  $\varphi_2 = 45^\circ$  with contour maps with intensities of 1.5/2.5/4/8/10/12. The components are given i Table 2.1

Sample	$\varphi_2 = 0^\circ$	$\varphi_2 = 45^\circ$
Comp.		
$0 - \pi$		
$0 - \pi$ NQ		
$0 - 4.71$		
$\pi - 1.4$		
$\pi - 0.7$		
$\pi - 0.5$		
$\pi - 0.44$		
$\pi - 0.34$		
$\pi - 0.26$		



The different components intensities are plotted in Figure 4.6. For  $\varphi_2 = 0^\circ$ , the C-component intensities in Figure 4.6a is read from  $\varphi_1 = 90^\circ$  and  $\Phi = 45^\circ$ , and the  $A^2$  intensities are read from  $\varphi_1 = 135^\circ$  and  $\Phi = 45^\circ$ . For  $\varphi_2 = 45^\circ$ , the C-component intensities in Figure 4.6b is read from  $\varphi_1 = 180^\circ$  and  $\Phi = 90^\circ$ , the  $B^1$ -component intensities are read from  $\varphi_1 \approx 70^\circ$  and  $\Phi \approx 60^\circ$  and the  $A^2$  intensities are read from  $\varphi_1 \approx 70^\circ$  and  $\Phi = 90^\circ$ .

(a)  $\varphi_2 = 0^\circ$ (b)  $\varphi_2 = 45^\circ$ Figure 4.6: The different component intensities for (a)  $\varphi_2 = 0^\circ$  and (b)  $\varphi_2 = 45^\circ$ .

Due to the varying texture intensities between the samples, the texture component fraction compositions for both  $\varphi_2 = 0^\circ$  and  $\varphi_2 = 45^\circ$  are presented in Figure 4.7 for comparison of relative texture component fractions between samples.

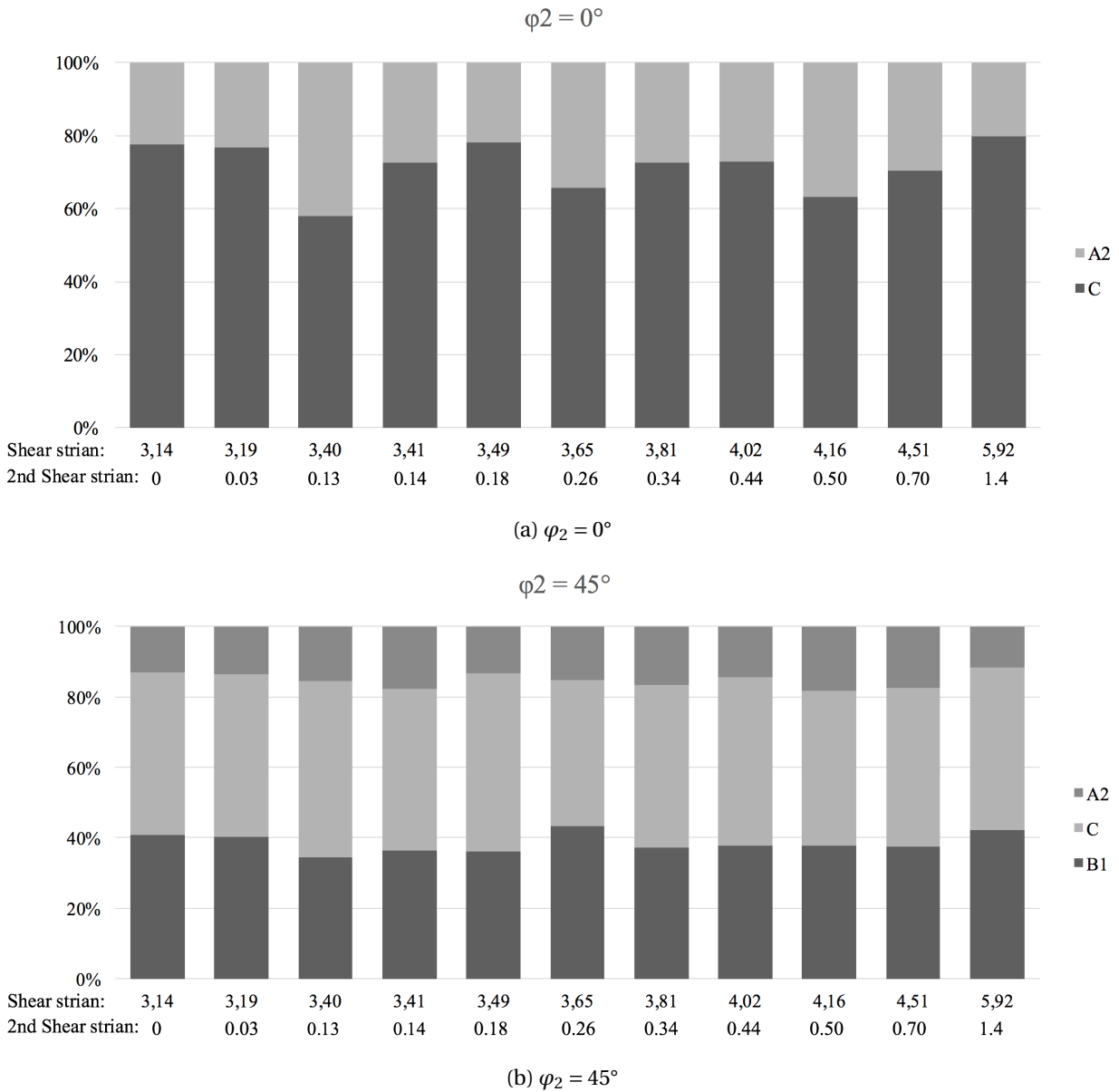
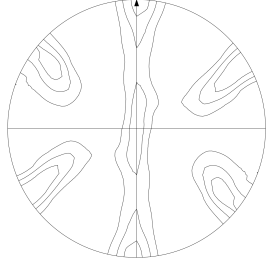
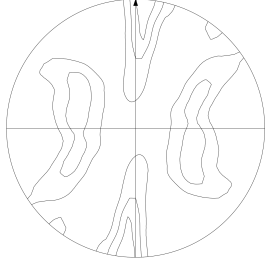


Figure 4.7: Components intensity fractions of the components for (a)  $\varphi_2 = 0^\circ$  and (b)  $\varphi_2 = 45^\circ$ .

The XRD obtained  $\{111\}$  and  $\{200\}$ -pole figures for all samples are presented in Appendix D. The  $\{111\}$  and  $\{200\}$ -pole figures for Sample  $\pi - 0$  are presented in Table 4.3. The first (horizontal) axis of the pole figures is the  $\theta$  direction and the second (vertical) axis is the  $z$  direction in relation to the torsion samples.

The texture analysis emphasises the ODFs, as the pole figures only have slight visible texture differences.

Table 4.3: The  $\{111\}$  and  $\{200\}$ -pole figures for Sample  $\pi - 0$  with contour maps with intensities of 1/2/3/4.5/6.

Sample	$\{111\}$ -pole figure	$\{200\}$ -pole figure
$\pi - 0$		

## 5 Discussion

In the following section the experimental results of average subgrain sizes, measured shear stress and texture will be discussed. Lastly, the accuracy of the results will be discussed based on the experimental work.

### 5.1 Deformation Memory

#### 5.1.1 Shear Stress Evolution

As anticipated, it was observed (Figure 4.4b) that the subgrain size decreased with a higher  $Z$ -value [2], laying the basis for the deformation memory investigation. The initial subgrain size for the 1<sup>st</sup> strain rate ( $Z = 3.33 \cdot 10^{13}$ ) was found to be just over  $2\mu m$ , with a steady-state flow shear stress of about  $27.5MPa$ . The subgrain size for the 2<sup>nd</sup> strain rate ( $Z = 1.27 \cdot 10^8$ ) was found to be between  $5 - 6\mu m$ , with a steady-state flow shear stress of about  $9MPa$ . Confirming the relation in Formula 11, saying that the flow stress is inversely proportional to the subgrain size [5].

Figure 4.4b presents the stress evolution in the change of strain rates. From the figure a clear drop in stress is visible at the change from  $\omega_1$  to  $\omega_2$ . In the change of angular velocity the shear stress at a low point of  $2MPa$  before it increased and reached steady-state flow stress of  $Z = 1.27 \cdot 10^8$ , opposed to a quick decrease from the 1<sup>st</sup> to the 2<sup>nd</sup> steady-state flow stress as illustrated in Figure 5.1. Ideally the measured stress-shear strain curve should resemble Figure 5.1, as the flow stress is dependent on subgrain size [2, 5] and it has been found that the subgrain size changes with a strain delay equal of the deformation memory. The observed stress is believed to originate from a regulation error in the torsion machines software, occurring in the change of angular velocity. The torsion machine is further discussed under §5.3.

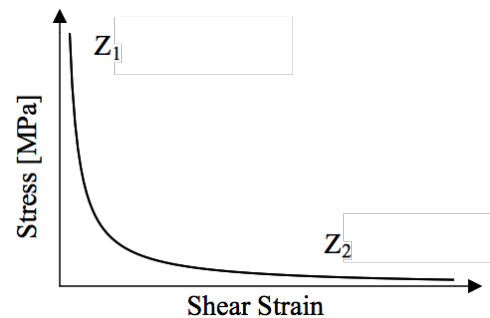


Figure 5.1: Expected stress evolution.

As the initial material was heterogeneous it had a random recrystallised texture prior to torsion. The random texture implies that each grain has a different Taylor factor than the others. The varying Taylor factor causes the grains to experience the stress unequally during deformation, as shown in Formula 10 [5, 16]. This results in grains orientated (relative to the sense of shear) corresponding with a high Taylor factor experiencing a higher stress, developing smaller subgrains hence Formula 11, and vice versa. Although the changes in stress for each subgrain is potentially up to 40% different, the measured shear stress during deformation will be the sum of the shear stress from all subgrains. As the average Taylor factor for FCC metals is 3.06 [14, 15] subgrains with higher or lower Taylor factor will approximately cancel each others deviation assuming a high number of subgrains in the material, thus the measured shear stress or the average subgrain size will not be affected from the change in Taylor factor.

### 5.1.2 Subgrain Size Evolution

It was found that the subgrain size increased until a 2<sup>nd</sup> shear strain of 0.26 was reached, then stabilising between 5 – 6  $\mu m$  (Figure 5.2). As presented in Figure 4.4b, for  $Z = 1.27 \cdot 10^8$ , the stress also reaches steady state flow at approximately 2<sup>nd</sup> shear strain of 0.26, again showing the correlation between subgrain size and stress. Thus, the measured stress curve could be singlehandedly used to give a rough estimation of a materials deformation memory, by investigating the slope in the measured stress whereas Formula 9 is not equal of 0, during the 2<sup>nd</sup> strain rate region [14, 15]. This method of analysis could therefore be preferable to identify the region of interest for further analysis of multiple deformation parameters such as temperatures, strain rates and different alloys as the measured stress can be monitored during each experiment. From the obtained results an empirical exponential approximation for the average subgrain size as a function of the 2<sup>nd</sup> shear strain was developed, and is presented in Formula 14 and plotted (red line) with the results in Figure 5.2.

$$\delta_2 = 5.5 - 3.6 \cdot \exp\left(\frac{-\gamma_2}{1/6}\right) \quad (14)$$



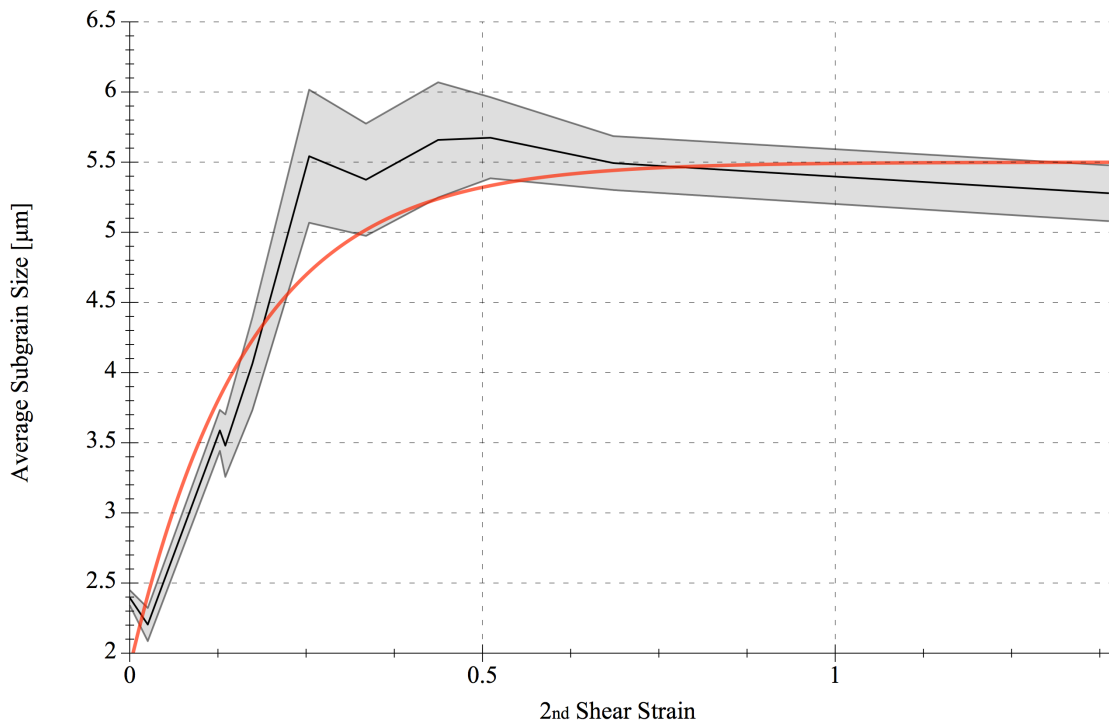


Figure 5.2: The average subgrain size as a function of 2nd shear strain, with the standard deviation marked in grey and the approximated subgrain size as a function of 2nd shear strain (red line).

Formula 14 assumes that the deformation is from between steady-state flow stress for two  $Z$ -values, where  $Z_1 = 3.33 \cdot 10^{13}$  and  $Z_2 = 1.27 \cdot 10^8$ . In further work a more general expression for the subgrain size should be implemented, accounting for the variable  $Z$ -values. Also an expression for the deformation memory at multiple parameters would be the final goal of the deformation memory investigation. However, in this early stage investigation there is insufficient data gathered to develop a general expression for the deformation memory.

The accuracy of the measured strain region in which the subgrain size is in a transient state between the 1<sup>st</sup> and the 2<sup>nd</sup> steady-state microstructure, is between (2<sup>nd</sup>) shear strains of 0.18 – 0.26, leaving the possibility that the deformation memory is less than 0.26. From investigations of the stress presented in Figure 4.4b it is found the deformation memory is unlikely smaller than a shear strain of 0.26, due to the rapidly increasing stress occurring at 2<sup>nd</sup> shear strains smaller than about 0.26. This indicates that the recovery process is occurring and the stress is not in steady state flow for the 2<sup>nd</sup> shear strain of 0.18. Due to the limited number of measurements in

the deformation memory region, the deformation memory cannot be given more precisely than the strain region of 0.18 – 0.26. Due to the stress evolution, the deformation memory is believed to be in the highest strain region between shear strains of 0.18 – 0.26.

### 5.1.3 Implications of the Deformation Memory

The implications of the discovered deformation memory of shear strains between 0.18 – 0.26 for AA6063 at 375°C are important for the understanding of subgrain size development during deformation.

In the case of extruding, the metals strain rate closest to the extrusion chamber will increase rapidly as the billet is pushed towards the die, assuming it flows past the dead zone in the extrusion chamber [1]. Whilst the metals deformation memory is delayed (with a shear strain between 0.18 – 0.26) it is possible that at point *e* (after the extrusion die) in Figure 1.1a the deformation memory does not remember point *d* (the extrusion die), but rather point *c* (prior to the extrusion die) instead. This could effect an extrusion cross section differently in accordance with the depth from the surface. E.g. the surface layer of the extrusion profile remembers the extrusion die with high Z-value ( $Z_{high}$ ) and the subgrain size is lowered, but slightly within of the extrusion profile the subgrains has a subgrain size equivalent of a Z-value ( $Z_{low}$ ) from within the extrusion chamber. Recovery occurs until the subgrain size (driving force for nucleation) is greater than  $\delta_c$ , at larger subgrains the recrystallisation process (grain growth) is dominant [2]. If the subgrain size for  $Z_{low}$  is in the region of  $\delta_c$  it is possible that the deformation memory in relation to the specific extrusion chamber and die gives rise to grain growth as presented in Figure 1.1c.

The deformation memory is temperature dependent as recovery and recrystallisation occurs more rapidly at higher temperatures [2], thus elevated temperatures will shorten the deformation memory. As an extrusion billet is passing through a die, its temperature will increase from friction and work hardening [1, 2, 28], shortening the metals deformation memory unevenly through its cross section. This alone could result in a surface layer with little deformation memory of the previous deformation from the extrusion chamber, leaving the surface with small grains from a high strain rate. As the temperature is decreasing inwards in the extrusion profile the middle of

the profile will have a longer deformation memory and thus possibly larger subgrains.

At the extrusion profiles surface in the die of the extruder, the strain rate ( $\geq 375/s$ ) and temperature are high [1, 2, 28], relative to inside the extrusion chamber. As the strain rate ( $\dot{\epsilon}$ ) is propositional with the Z-value and Z-value decreases exponentially with higher temperatures ( $T$ ), the Z-value (Formula 12) could remain about equal depending on the relation between strain rate and temperature. As the Zener–Hollomon parameter is only a steady-state parameter and the deformation memory is the strain region between two steady-states, extrusion simulations based on the Z-value could produce simulated microstructures that does not account for the changing deformation memory with varying strain rates and temperatures, giving inaccurate results.

The deformation memory will affect all the discussed subjects during extrusion and other hot deformation processes. Properly designing process equipment for high quality cosmetic applications requires total control on the mechanisms in work [3], accounting for the deformation memory is one step in that direction.

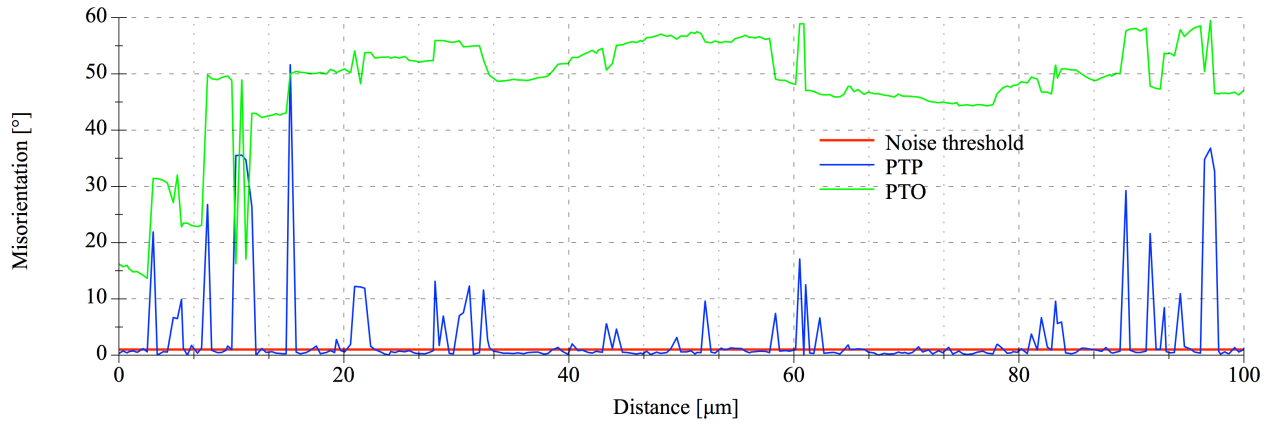
## 5.2 Texture Development

Due to the similarity of the pole figures (Appendix D) only the ODFs will be analysed, as the pole figures are two dimensional projections of the texture and the ODFs are more precise representations of the texture [17, 18]. When comparing the texture for  $\varphi_2 = 0^\circ$  and  $\varphi_2 = 45^\circ$  of Sample  $\pi - 0$  ( $Z = 3.33 \cdot 10^{13}$ ) and Sample  $0 - \pi$  ( $Z = 1.27 \cdot 10^8$ ) it is seen that the different shear strain rates results in near identical textures, as expected; showing that the texture only changes with strain [17, 18] and not with transient changing strain rates. Also Sample  $0 - \pi$  NQ shows that the texture of a not quenched sample does not differ substantially from the Sample  $0 - \pi$ , with a lower intensity of the same texture components. This indicates either that (1) the recrystallisation texture for torsion is not only characterised by the presence of the  $Bs$  texture component, but rather that the recrystallisation texture originate from grain boundary nucleation resulting in the slightly weaker texture [2]. (2) The torsion temperature has been too low for the sample to be recrystallised, leaving the sample partially recrystallised with a weaker texture. (3) The external cooling of the torsion machine cooled the sample too quickly, leaving the sample partially recrystallised with a weaker texture.

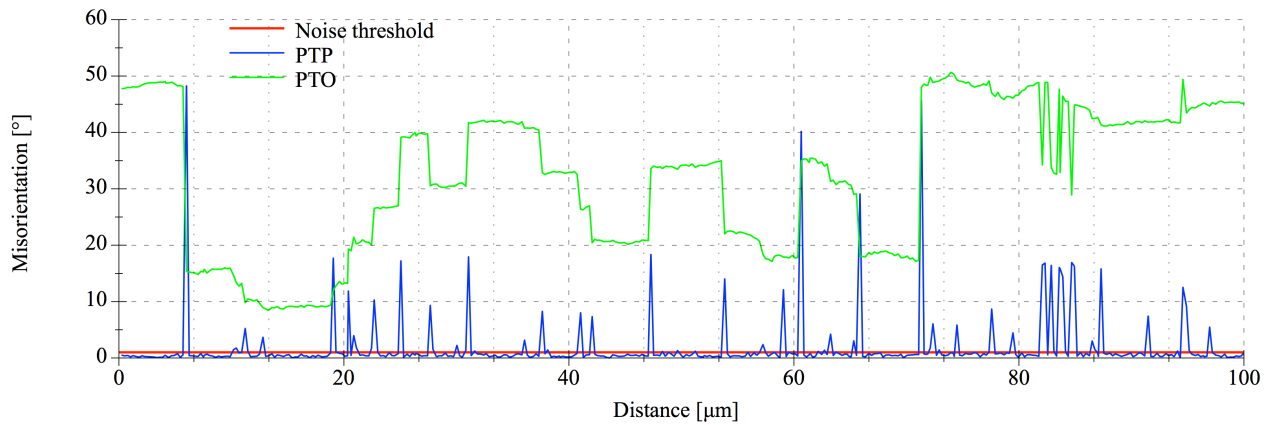
To investigate the two latter options experiment Ref.5 375 RX 120s was conducted, annealing a sample with equal strain for 120 seconds directly after torsion. Sample Ref.5 375 RX 120s texture shows the same components, but with an unexpected intensity increase. The most visible change in texture is in the ODF for  $\varphi_2 = 45^\circ$ , where the  $A^2$ -components intensity is stronger than for Sample  $0 - \pi$  NQ and Sample  $0 - \pi$ . However, for Sample  $\pi - 0$  the  $A^2$ -components are similar to Sample Ref.5 375 RX 120s making it difficult to conclude to what differentiates Sample Ref.5 375 RX 120s from the quenched samples other than increased texture intensity. Looking at the ODF for  $\varphi_2 = 45^\circ$  for Sample Ref.3 400 and Sample Ref.4 400 NQ it is clear that the texture for Sample Ref.4 400 NQ has a higher intensity. The rise in intensity for samples not quenched or annealed could indicate that only recovery occurs, allowing for texture gradients within the grain structure to be annihilated, thus the stronger texture [2].

Figure 5.3 presents a single  $100\mu m$  ptp-measurement for Sample Ref.3 400, Ref.4 400NQ and Ref.5 375 RX 120s, parallel to the shear direction where the grains are elongated in this direction

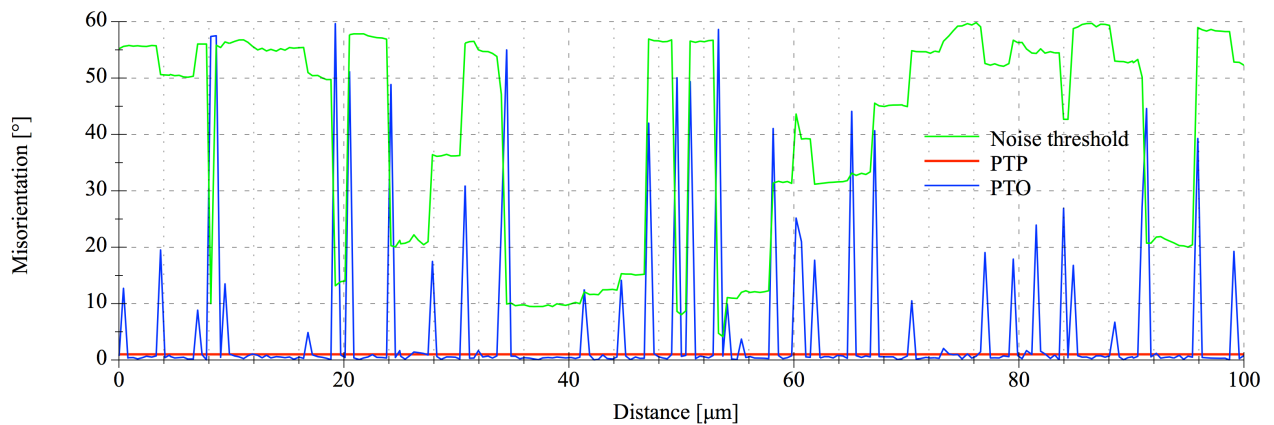
and the texture gradients are found to be most apparent.



(a) Sample Ref.3 400



(b) Sample Ref.4 400NQ



(c) Sample Ref.5 375 RX 120s

Figure 5.3: PTP-line intercept measurement for (a) Sample Ref.3 400 (b) Sample Ref.4 400NQ and (c) Sample Ref.5 375 RX 120s. The measurements were taken parallel the sense of shear.

Table 5.1 presents the average subgrain sizes for the mentioned samples. It can be seen that both Sample Ref.4 400 *NQ* and Sample Ref.5 375 *RX* 120s have had some subgrain growth, as expected. Due to the larger subgrain size in Sample Ref.4 400 *NQ* and as the sample is not quenched it is clear that the driving force for recovery is stronger at 400°C, when comparing with Sample Ref.5 375 *RX* 120s which is annealed for 120 seconds at 375°C.

Table 5.1: Subgrain sizes for Ref.3, Ref.4 and Ref.5.

Sample	$\bar{\delta}$ [ $\mu m$ ]	Standard deviation
Ref.3 400	2.70	0.10
Ref.4 400 <i>NQ</i>	5.55	0.70
Ref.5 375 <i>RX</i> 120s	3.40	0.13

Figure 5.3a shows that from the PTO-line that several grains have orientation gradients, whilst in Figure 5.3b and 5.3c there are less apparent orientation gradients, and it's difficult to separate gradients from measurement noise. These are only three measurements and are not representative for the entire samples, however they indicate to confirm the mentioned hypothesis. The absence of strong orientation gradients in Figure 5.3b and 5.3c combined with the observed grain growth (Table 5.1) suggests that samples with strengthened texture is a result of recovery.

In regards to texture evolution from shear strains of 3.14 to 6.3 little change was expected to occur, as the shear strain is low [5, 9]. Although Kassners *et al.* (1989) experiments were recrystallised, he found that little texture change occurs between strains from 3 to 10. He found that only the  $A^1$ ,  $B^1$  and  $C$  components weakened from a respectively (see Table 2.2) M, M and S to W-M, M-W and M during this strain. Experiments preformed by Montheillet *et al.* (1984) showed that a strain of 0.62 ( $\gamma = 1.1$ ) gives a dominant  $A^1$  orientation, and with a strain of 5.58 ( $\gamma = 9.7$ ) at 200°C mainly gives a  $C$  texture component with a weak  $B^1$  component. As both Kassners and Montheillets only investigated XRD obtained pole figures it is reasonable to assume that they only observed a couple of texture components, as they can be difficult to differentiate in a pole figure. As experiments in this work has ODF texture data, it is easier to investigate the

individual components. Comparison of Montheillets and Kassners results are difficult, due to their different notations of intensities, however they both found strong  $C$  component intensity with varying intensity of  $A^1$  and  $B^1$  for approximately equal strains as in this work. Kassners recrystallised texture, Montheillets deformed texture and the deformed texture from this work, indicate that the recrystallised texture can consist of the deformed texture components, although annealing experiments done by Pettersen (1999) shows that recrystallised samples often have a characteristic  $Bs$  texture component. As no samples in this work were fully recrystallised after deformation it is impossible to identify a characteristic ODF for recrystallised torsion texture, including the  $Bs$  texture component. If the  $Bs$  texture component would have been identified it would be easier to characterise deformed and recrystallised samples. However, this was not achieved in this work. In future work the  $Bs$  texture component should be identified in an ODF for easier comparison.

For this projects experiments it was found that the maximum texture intensity for each sample varied, as shown in Figure 4.6. This may be a result of recovery occurring unequally for the samples, indicating inconsistencies with the torsion machines quenching mechanism. The measured textures intensities make it difficult identify a trend in the component evolution during shear strains from 3.14 to 6.28. In effort to compare the measured intensities relative to the sample intensities, the intensities were plotted as relative component fractions in Figure 4.7. Due to uncertainties in the texture component reading, only the  $A^2$  and  $C$  component were read for  $\varphi_2 = 0^\circ$  and the  $A^2$ ,  $C$  and  $B^1$  component for  $\varphi_2 = 45^\circ$ . As seen in both graphs presented in Figure 4.7 the relative fractions of texture components for both  $\varphi_2 = 0^\circ$  and  $\varphi_2 = 45^\circ$  are about equal, showing that no texture change of the observed components occurred during the deformation memory strain region.

When comparing the measured texture with the simulated texture it can be seen that the Alamel-model best predict the measured texture. However, its intensities are up to three times the intensity of the measured samples, and thus not directly comparable. For the simulated (Alamel-model) texture, the only notable texture change for  $\varphi_2 = 45^\circ$  is that the  $B^1$  texture component intensity slightly increases with shear strain from 3 to 6. For  $\varphi_2 = 0^\circ$  it is seen that the  $A^2$  texture component intensity (at  $\Phi = 45^\circ$  and  $\varphi_1 = 135^\circ$ ) increases, whilst the  $C$  texture component

intensity remains about constant. As shear strains between 3 to 6 is a small strain region little texture evolution is expected [2, 17]. The measured texture for  $\varphi_2 = 45^\circ$  is equal to the simulated Alamel-model texture, with weaker intensity. The only observed change in the texture between the measured and the simulated Alamel-model texture is for the  $A^2$  component, where it's intensity  $\Phi = 45^\circ$  and  $\varphi_1 = 35^\circ$  was measured to increase from 2<sup>nd</sup> shear strains of 0.18 until 0.7. The cause of the difference in texture evolution is unknown. It is possible that during subgrain growth occurring in this strain region, the  $A^2$  component crystallographic orientation is orientated preferable in relation to the sense of shear for subgrain growth to occur, thus the increased texture intensity.

By only investigating the texture in ODFs the  $B_s$  texture component can not be investigated as the texture component was not identified in ODFs for monoclinic sample symmetry. However, by investigating the  $\{111\}$ -pole figures the  $B_s$  component cannot be separated from the  $B^1$  component, leaving only the  $\{200\}$ -pole figure for further analysis. Investigations of the  $\{200\}$ -pole figures for the samples where the most recovery have occurred, Sample Ref.4 400 NQ and Sample Ref.5 375 RX 120s, shows no indication of a  $B_s$  texture in the samples. The abstinence of the  $B_s$  texture component in addition to the measured subgrain sizes (Table 5.1) shows that very little, if any, recrystallisation have occurred. In future work, it would be beneficial to investigate the deformation memory at higher temperatures, as AA6063 does not fully recrystallise at  $375^\circ\text{C}$  within a timeframe of 120 seconds. By performing experiments at higher temperatures the obtained microstructure will be more distinctive, either deformed or recrystallised, and thus easier to characterise. However with elevated temperature will the deformation memory shorten in terms of strain, making the deformation memory investigation more challenging.

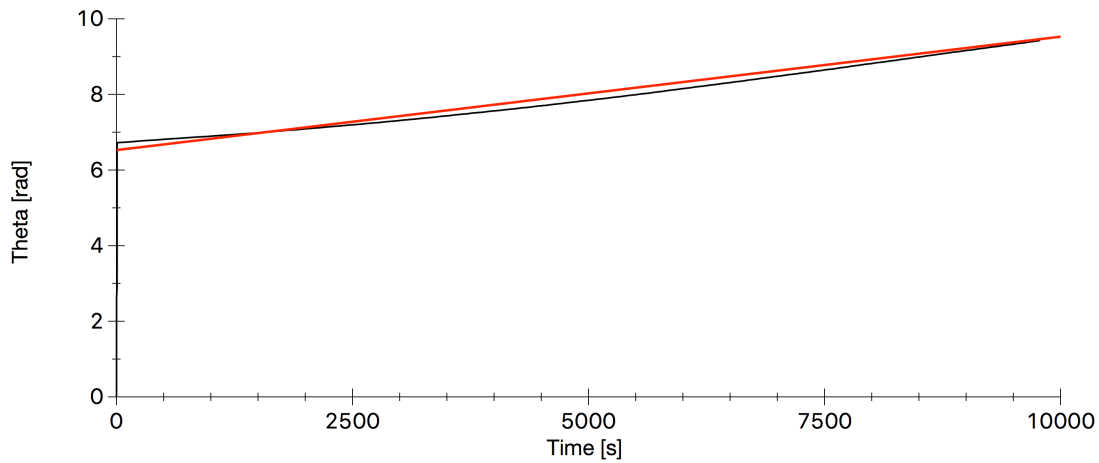


### 5.3 Result accuracy

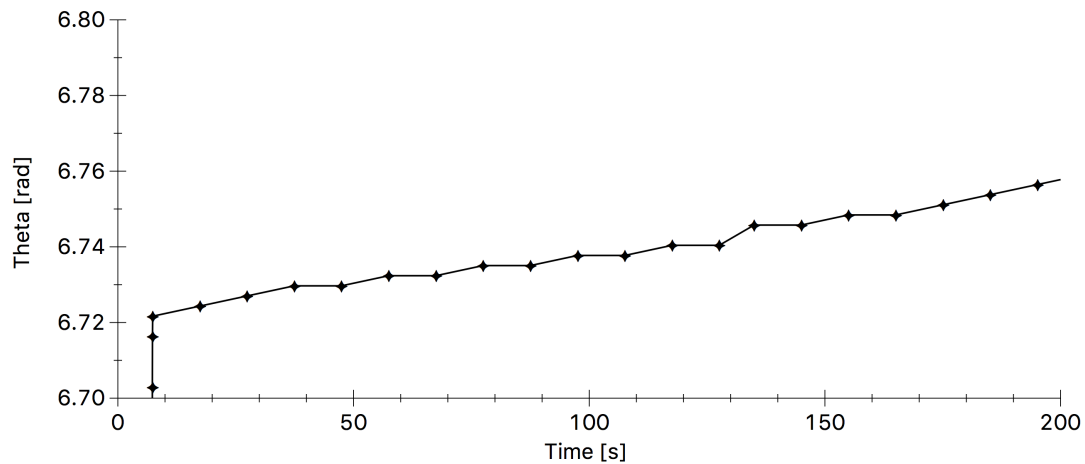
During the experimental work it was discovered that the torsion machine did not deliver the programmed angles of twist, resulting in the deviations (up to shear strain of about 0.2 extra 1<sup>st</sup> shear strain) in shear strain in relation to the experimental plan (Table 3.4). However, the angles of twist were recorded using a separate device than the torsion machine, as reference. These recorded angles of twist are the ones used in this work. Whether or not all samples' got an exact 1<sup>st</sup> angle of twist of 3.14 is irrelevant in regards to the subgrain size as all samples' were stable in steady-state flow stress for the 1<sup>st</sup> angular velocity ( $Z = 3.33 \cdot 10^{13}$ ) [2], in addition to the texture investigation due to the external measured angles of twist. As for the 2<sup>nd</sup> angle of twist, the actual angle of twist were recorded giving precise results.

As mentioned, it was observed that the samples' texture intensities varied slightly. As it is believed that samples with stronger texture have been subject to excessive recovery, the accuracy of the torsion machines quenching mechanism must be verified for further work.

Another observation from the experimental work was the unexpected stress evolution in the change of angular velocities, as described in §5.1.1. Investigations of the measurement data from the torsion machine have shown that as the torsion machine changes angular velocity, a one iteration delay in the software occurs resulting in a momentary drop in stress before torsion reinitiates at the next iteration and the stress is regained. Investigation of the angle of twist in relation to time (Figure 5.4) does not show any signs of this regulation error as  $\theta$  is increasing gradually, as shown in Figure 5.4b. Figure 5.4a reveals another regulation error with the torsion machine software. Comparing the red line to the measurement data it is visible that the angular velocity is not constant. However, the slope in the measured data is so moderate that during the deformation memory it is close to linear, it is therefore believed that this has little impact on the Z-value during the deformation memory.



(a)



(b)

Figure 5.4: Recorded torsion measurements for angle of twist as a function of time.

In further work the torsion machine software will have to be improved for a precise change of angular velocities and precision for angles of twist-setpoints. The impact of this iteration delay is unknown. From investigations of the samples' subgrain size showing growth up to shear strains of 0.26 in addition to Sample Ref.5 375 RX 120s little subgrain growth during annealing for 120 seconds, it is believed that the iteration error has had little impact on the samples' subgrain size at 375°C. As the samples have varying texture intensities and the texture intensity is related to recovery the quenching mechanism may not be the problem, as the duration of a iteration in the software varies from run to run. This will result in the different samples having slightly different

opportunities for recovery during this iteration between change of angular velocity, and thus different texture intensities.

From Figure 5.4b it is seen that the recorded angle of twist ( $\theta$ ) is not linear with time. As the torsion machines hydraulic motor was given a constant signal for the pressure vent opening, the recorded  $\theta$  values non linear behaviour is probably due to the optical counting device. During the experimental work, it was observed that the torsion machines optical counting devices disk had unevenly spaced measuring points. Looking at Figure 5.4a, it is seen that although the measured  $\theta$  is not linear, it is an even line with a slight slope. From Figure 4.4b and Figure 5.4b it is apparent that the recording of both the stress and angle of twist has measurement noise. The standard deviation for the shear stress recording was measured to be  $\pm 3\%$ , and the standard deviation for the angle of twist was found to be  $\pm 0.01\%$ . As these deviation are low they have not been taken into account.

During the sample preparation the surface of the torsion samples were straightened and sanded on the surface. This was done manually by hand, as the samples' little size made them difficult to handle. The manual sanding of the samples leaves room to variations in the depth of sanding, in regards to the radius of the torsion sample. As the sanding of the samples are kept to a minimum, the radius loss is neglected in all calculations of shear strain and shear strain rate, and thus strain, strain rate and Z-value. This radius loss is estimated to be about  $50\mu m$ , which would not significantly affect the results.

## 6 Conclusion

In this project the influence of transient change in strain rate on subgrain size during deformation by torsion of AA6063 have been studied. This was done by deforming the metal at a high (1<sup>st</sup>) strain rate allowing the steady-state microstructure of the high strain rate to develop, then immediately changing the strain rate to a 2<sup>nd</sup> lower strain rate. By performing experiments with various 2<sup>nd</sup> strains, the subgrain size evolution between two steady-state microstructures was investigated. This strain region is defined as the metals deformation memory.

The results from this investigation have shown that AA6063s deformation memory at 375°C is in the higher strain region of shear strains between 0.18 – 0.26, which is equivalent to strains between 0.10 – 0.15.

The stress during deformation was also investigated. A correlation between the recorded shear stress and the deformation memory was found, showing that the shear stress is a transient state during the deformation memory.

Texture investigations have shown little texture evolution during the investigated strains. Orientation gradients were observed in the deformed state. It was found that the samples' texture intensity increased with recovery due to annihilation of the orientation gradients.

In further work the deformation memory will have to be identified for various temperatures, as the deformation memory is temperature dependent. Due to regulation errors will the torsion machine need to be assessed before continuation of experimental work.

---

## 7 Referanses

- [1] George E. Dieter. *Mechanical metallurgy*. McGraw-Hill New York, si ed. edition, 1976.
- [2] F.J. Humphreys og M. Hatherly. *Recrystallization and Related Annealing Phenomena*. Elsevier, Oxford, second edition edition, 2004.
- [3] SAPA. Next generation extrusion technology for high performance cosmetic application - cosmetex. August 2015.
- [4] The University of Liverpool. MATTER. Torsion test. <http://aluminium.matter.org.uk/content/html/eng/default.asp?catid=175&pageid=2144416592>, February 2016.
- [5] Tanja Pettersen. A study of the deformation and recrystallization microstructures and textures an AA6060 and AA6082 alloys. NTNU - Institutt for materialteknologi og elektrokjemi, 1999.
- [6] J Bailey. Fundamental aspects of torsional loading. Metals Handbook, volume 8., 9th edition, 1985.
- [7] W. Blum, Q. Zhu, R. Merkel, and H.J. McQueen. Geometric dynamic recrystallization in hot torsion of al5mg0.6mn (aa5083). *Materials Science and Engineering: A*, 205(1–2):23 – 30, 1996.
- [8] John J. Jonas, Chiradeep Ghosh, and Laszlo S. Toth. The equivalent strain in high pressure torsion. *Materials Science and Engineering: A*, 607:530 – 535, 2014.
- [9] M.E. Kassner, M.M. Myshlyayev, and H.J. McQueen. Large-strain torsional deformation in aluminum at elevated temperatures. *Materials Science and Engineering: A*, 108:45 – 61, 1989.
- [10] Bjørn Holmedal. Geometriberegning, September 2015.
- [11] HE Vatne, MG Mousavi, S Benum, B Ronning, and E Nes. Texture and structure evolution in AlMn and commercial purity aluminium deformed by monotonic and reversed hot torsion.

- 
- In *Aluminium Alloys: Their Physical and Mechanical Properties, Pts 1–3*, volume 217, pages 553–558, 1996.
- [12] Christian Oen Paulsen. Recrystallisation behaviour in extruded profiles of non-dispersoid containing al-mg-si alloys. Master's thesis, NTNU, 2015.
- [13] M.E. Kassner. Chapter 7 - recrystallization. In M.E. Kassner, editor, *Fundamentals of Creep in Metals and Alloys (Third Edition)*, pages 159 – 165. Butterworth-Heinemann, Boston, third edition edition, 2015.
- [14] K. Marthinsen and E. Nes. Modelling strain hardening and steady state deformation of al–mg alloys. *Materials Science and Technology*, 17(4):376–388, 2001.
- [15] Knut Erik Snilsberg. Mikrostruktur og mekaniske egenskaper for 7xxx-legeringer. Master's thesis, Norges teknisk-naturvitenskapelige universitet, 2009.
- [16] H. Justinger and G. Hirt. Estimation of grain size and grain orientation influence in micro-forming processes by taylor factor considerations. *Journal of Materials Processing Technology*, 209(4):2111 – 2121, 2009.
- [17] V. Randle and O. Engler. *Introduction to Texture Analysis: Macrotecture, Microtexture and Orientation Mapping*. Taylor & Francis, 2000.
- [18] Chapter 8 textural developments during thermo-mechanical processing. In Indradev Samajdar Bert Verlinden, Julian Driver and Roger D. Doherty, editors, *Thermo-Mechanical Processing of Metallic Materials*, volume 11 of *Pergamon Materials Series*. Pergamon, 2007.
- [19] The University of Liverpool. MATTER. Orientation distribution function. <http://core.materials.ac.uk/search/detail.php?id=2625>, February 2016.
- [20] Paul Van Houtte, Saiyi Li, Marc Seefeldt, and Laurent Delannay. Deformation texture prediction: from the taylor model to the advanced lamel model. *International Journal of Plasticity*, 21(3):589 – 624, 2005.
- [21] M. Cohen og J.J. Jonas F. Montheillet. Axial stresses and texture development during the torsion testing of al, cu and  $\alpha$ -fe. *Acta Metallurgica*, 32(11):2077 – 2089, 1984.

- 
- [22] L.S Toth, P Gilormini, and J.J Jonas. Effect of rate sensitivity on the stability of torsion textures. *Acta Metallurgica*, 36(12):3077 – 3091, 1988.
- [23] A Panigrahi, N Scheerbaum, P Chekhonin, J Scharnweber, B Beausir, M Hockauf, S Sankaran, and W Skrotzki. Effect of back pressure on material flow and texture in ecap of aluminum. *IOP Conference Series: Materials Science and Engineering*, 63(1):012153, 2014.
- [24] M. Arzaghi, J.J. Fundenberger, L.S. Toth, R. Arruffat, L. Faure, B. Beausir, and X. Sauvage. Microstructure, texture and mechanical properties of aluminum processed by high-pressure tube twisting. *Acta Materialia*, 60(11):4393 – 4408, 2012.
- [25] Satyam Suwas, László S. Tóth, Jean-Jacques Fundenberger, André Eberhardt, and Werner Skrotzki. Evolution of crystallographic texture during equal channel angular extrusion of silver. *Scripta Materialia*, 49(12):1203 – 1208, 2003.
- [26] László S. Tóth. Modelling of preferred orientation. *Laboratoire de Physique et Mécanique des Matériaux, Université de Metz, France*, 2005.
- [27] Abdel Yazid Khereddine, Fayçal Hadj Larbi, Hiba Azzeddine, Thierry Baudin, François Brisset, Anne-Laure Helbert, Marie-Hélène Mathon, Megumi Kawasaki, Djamel Bradai, and Terence G. Langdon. Microstructures and textures of a cu–ni–si alloy processed by high-pressure torsion. *Journal of Alloys and Compounds*, 574:361 – 367, 2013.
- [28] K. Zhang, B. Holmedal, O. S. Hopperstad, S. Dumoulin, J. Gawad, A. Van Bael, and P. Van Houtte. Multi-level modelling of mechanical anisotropy of commercial pure aluminium plate: Crystal plasticity models, advanced yield functions and parameter identification. *International Journal of Plasticity*, 66:3–30, 3 2015.
- [29] Jarle Hjelen. Scanning Electron-Mikroskopi. Kompendie, Metallurgisk institutt, NTH, March 1989.
- [30] Oxford Instruments Plc. X-ray diffraction. [http://www.ebsd.com/popup/box4\\_texture.htm](http://www.ebsd.com/popup/box4_texture.htm), April 2016.

- 
- [31] Andrew J. Ying, Conal E. Murray, and I. C. Noyan. A rigorous comparison of X-ray diffraction thickness measurement techniques using silicon-on-insulator thin films. *Journal of Applied Crystallography*, 42(3):401–410, Jun 2009.
- [32] Stephen Zahra. Understanding pid. <https://sites.google.com/site/controlandelectronics/understanding-pid>, March 2016.
- [33] Stanka Tomovic-Petrovic and Ola Jensrud. Extrusion of silicon-rich AlMgSi alloys. *Journal of Materials Processing Technology*, 212(6):1437 – 1442, 2012.
- [34] SAPA. Sapa extrusions north america. <http://www.sapagroup.com/pages/522574/Brochures/Alloy%206063%20Rev2012.pdf>, September 2015.
- [35] Alcoa Engineered Products. Understanding extruded aluminium alloys. [http://www.alcoa.com/adip/catalog/pdf/Extruded\\_Alloy\\_6063.pdf](http://www.alcoa.com/adip/catalog/pdf/Extruded_Alloy_6063.pdf), September 2015.
- [36] Ø. Grong L. Kolbeinsen Casper van der Eijk, Gabriella Maria Tranell. Microstructure control of steels through dispersoid metallurgy using novel grain refining alloys. *ISIJ International*, 46(6):824–831, 2006.
- [37] Kai Zhang. Hyperxtrude simulations. 2016.



## A Derivation of the Grain Elongated

Using geometric relations a quadratic grains diagonal  $S_o$  is described by Formula 16.

$$S_o = \sqrt{l^2 + l^2} \quad (15)$$

$$S_o = \sqrt{2}l \quad (16)$$

The length  $a$  in Figure 2.2b is described by Formula 18.

$$d^2 = l^2 + a^2 \quad (17)$$

$$a = \sqrt{d^2 - l^2} \quad (18)$$

The elongated diagonal,  $S$ , is then described by Formula 20.

$$S = \sqrt{l^2 + (a + l)^2} \quad (19)$$

$$S = \sqrt{l^2 + \left(\sqrt{d^2 - l^2} + l\right)^2} \quad (20)$$

For a grain of length,  $l = 1$ ,  $a$  is given by the shear strain of the grain, given the relation  $\gamma = \frac{r\theta}{L}$ ,  $S$  can be expressed as a function of shear strain in Formula 22.

$$S = \sqrt{1 + \left(\frac{\theta r}{L} + 1\right)^2} \quad (21)$$

$$S = \sqrt{1 + (\gamma + 1)^2} \quad (22)$$

The elongated diagonal  $S$  relation to  $S_o$  is accordingly expressed by the relationship given in Formula 23.

$$\frac{S}{S_o} = \frac{\sqrt{1 + (\gamma + 1)^2}}{\sqrt{2}l} = \sqrt{\frac{1}{2} + \frac{1}{2}(\gamma + 1)^2} \quad (23)$$

## B IPF and IQ-maps

In this appendix the IPF-map and IQ-map for each sample are presented. All maps in this section are presented with the horizontal direction in the  $z$  direction and the vertical direction in the  $\theta$  direction in relation to the torsion samples. The colours in the IPF-maps represent crystallographic orientations, which are presented in Figure B.1.

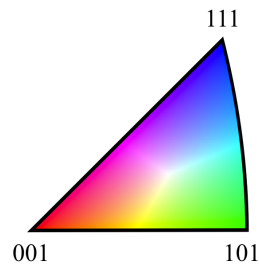


Figure B.1: The colour representation of crystallographic orientations.

### B.1 Sample Ref.1 350°C

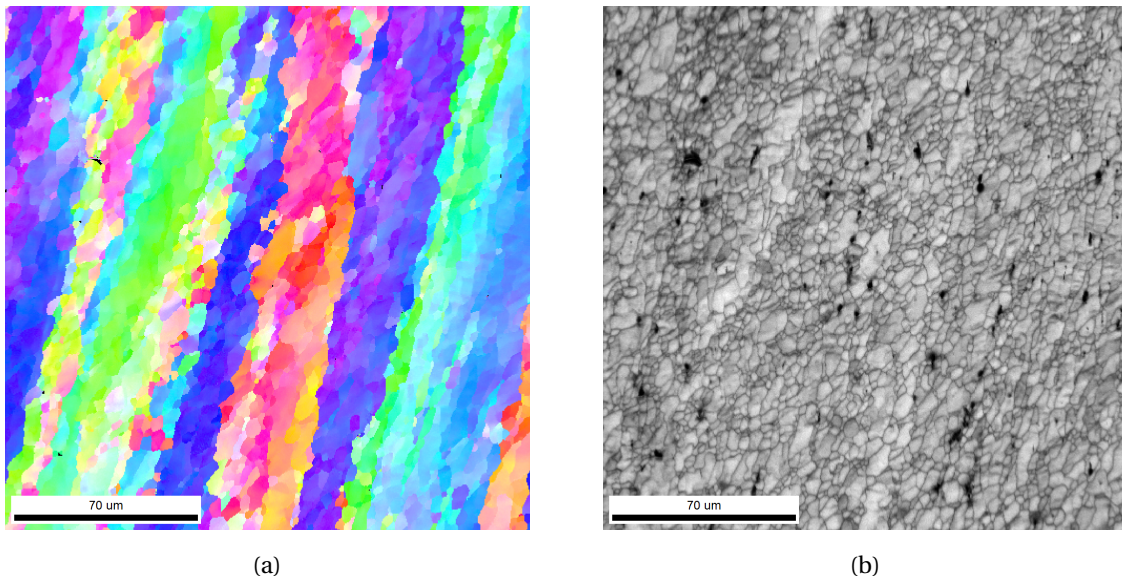


Figure B.2: (a) The IPF-map and (b) IQ-map for Sample Ref.1 350°C.

**B.2 Sample Ref.2 375°C**

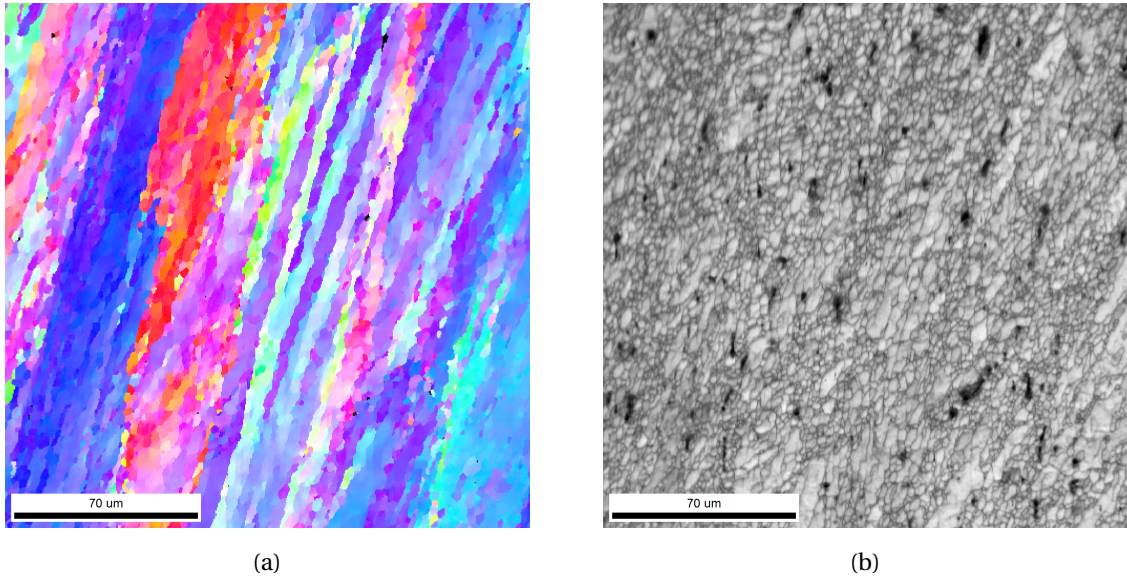


Figure B.3: (a) The IPF-map and (b) IQ-map for Sample Ref.2 375°C.

**B.3 Sample Ref.3 400°C**

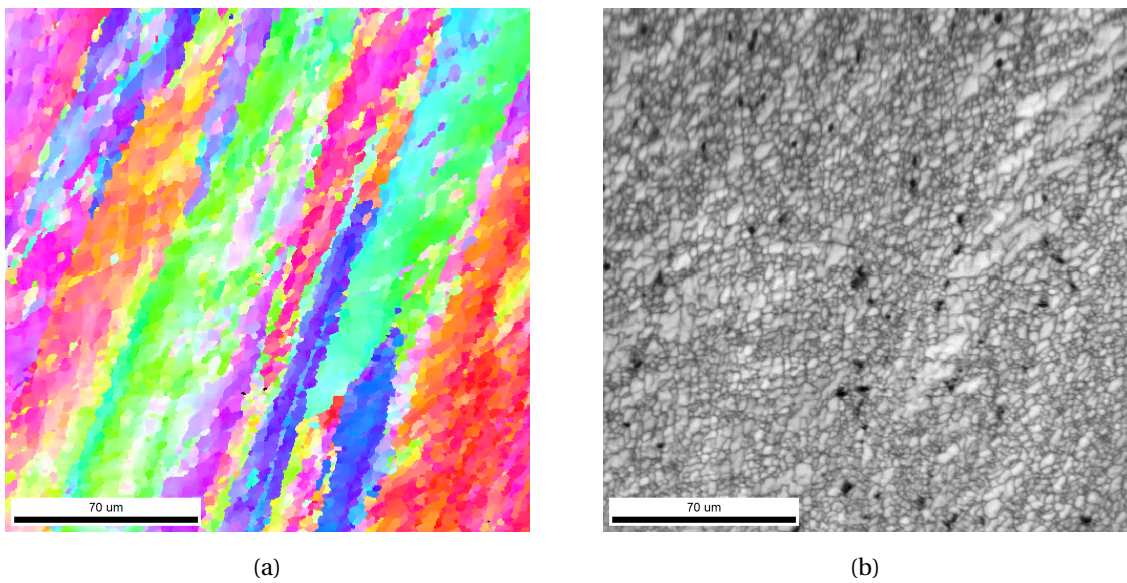


Figure B.4: (a) The IPF-map and (b) IQ-map for Sample Ref.3 400°C.



**B.4 Sample Ref.4 400°C NQ**

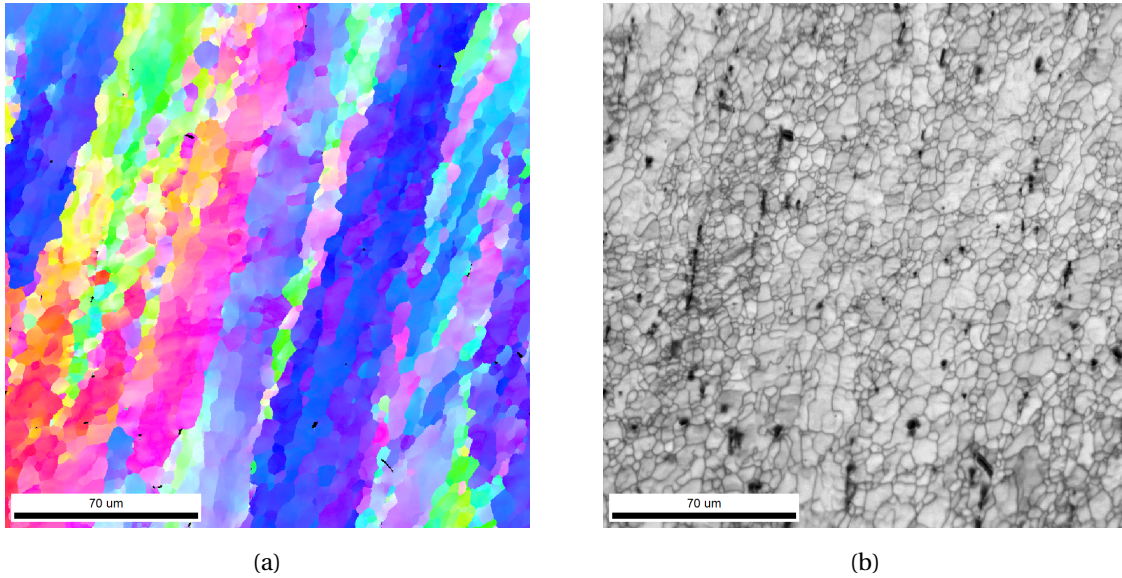


Figure B.5: (a) The IPF-map and (b) IQ-map for Sample Ref.4 400°C NQ.

**B.5 Sample Ref.5 375°C RX 120sec**

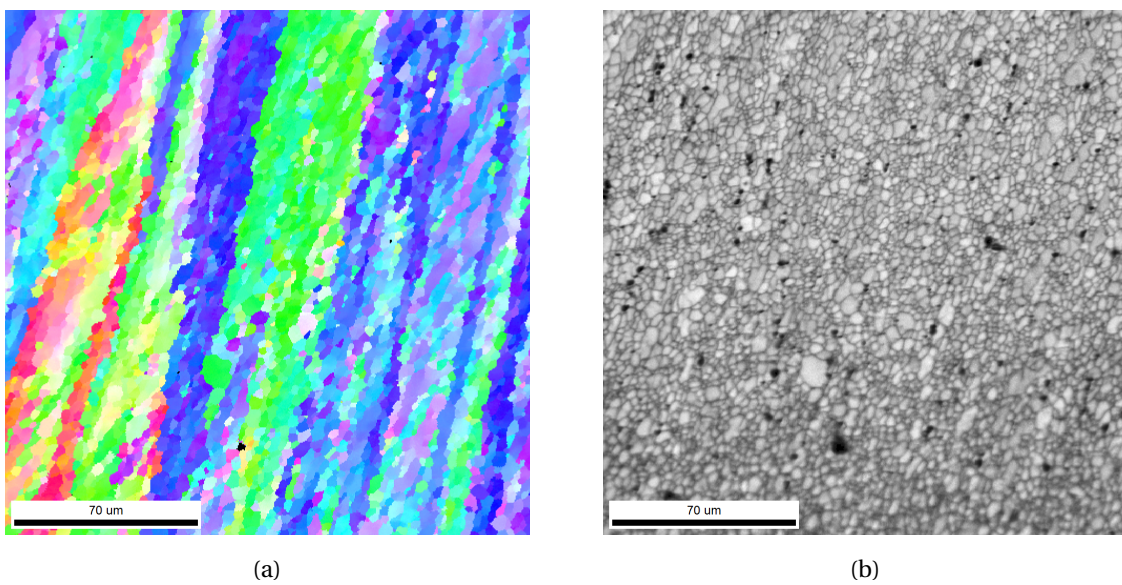
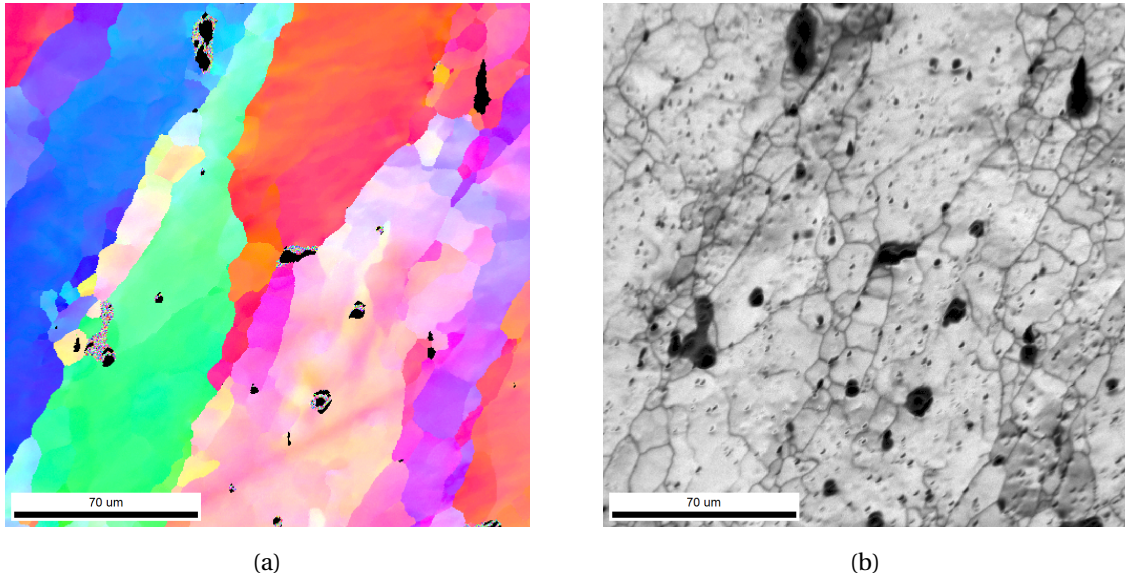
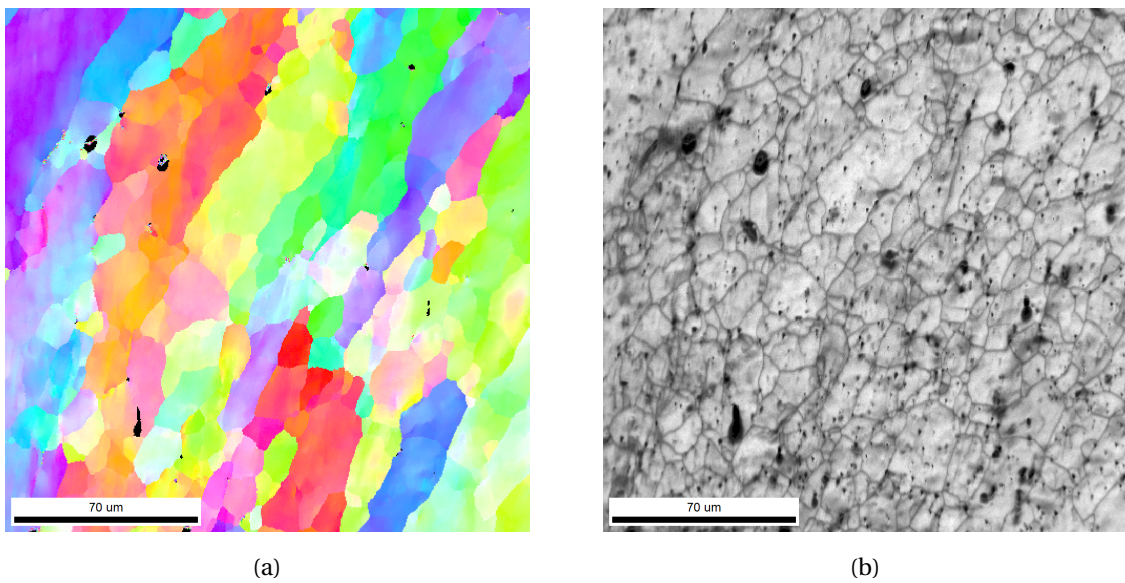


Figure B.6: (a) The IPF-map and (b) IQ-map for Sample Ref.5 375°C annealed 120sec.

**B.6 Sample 0- $\pi$** Figure B.7: (a) The IPF-map and (b) IQ-map for Sample 0- $\pi$ .**B.7 Sample  $\pi$ -0 No Quench**Figure B.8: (a) The IPF-map and (b) IQ-map for Sample  $\pi$ -0 NQ.



**B.8 Sample 0-3 $\pi$**

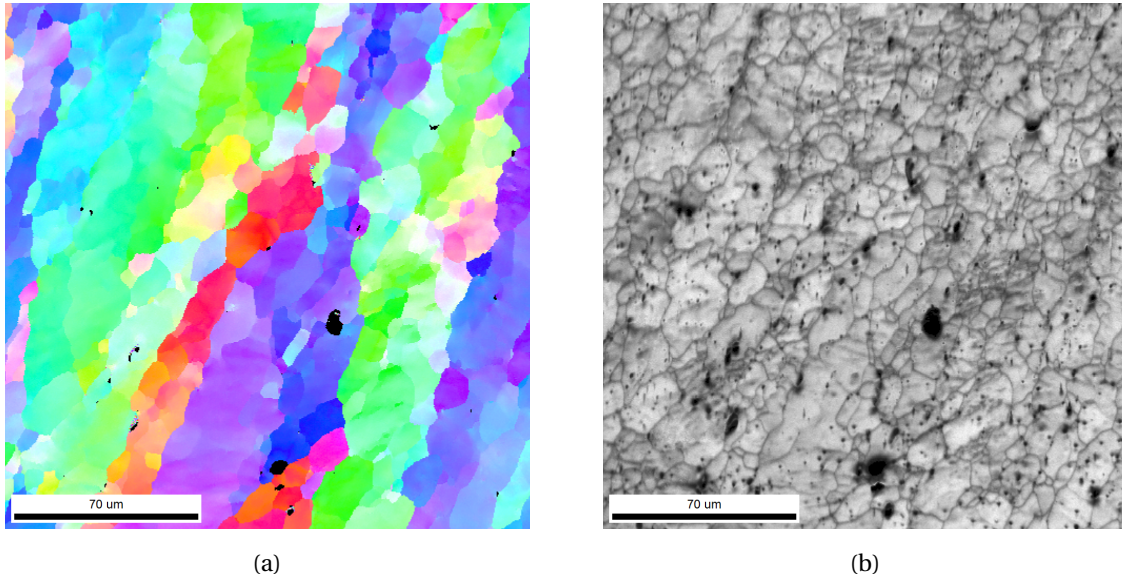


Figure B.9: (a) The IPF-map and (b) IQ-map for Sample 0-4.71.

**B.9 Sample  $\pi$ -1.4**

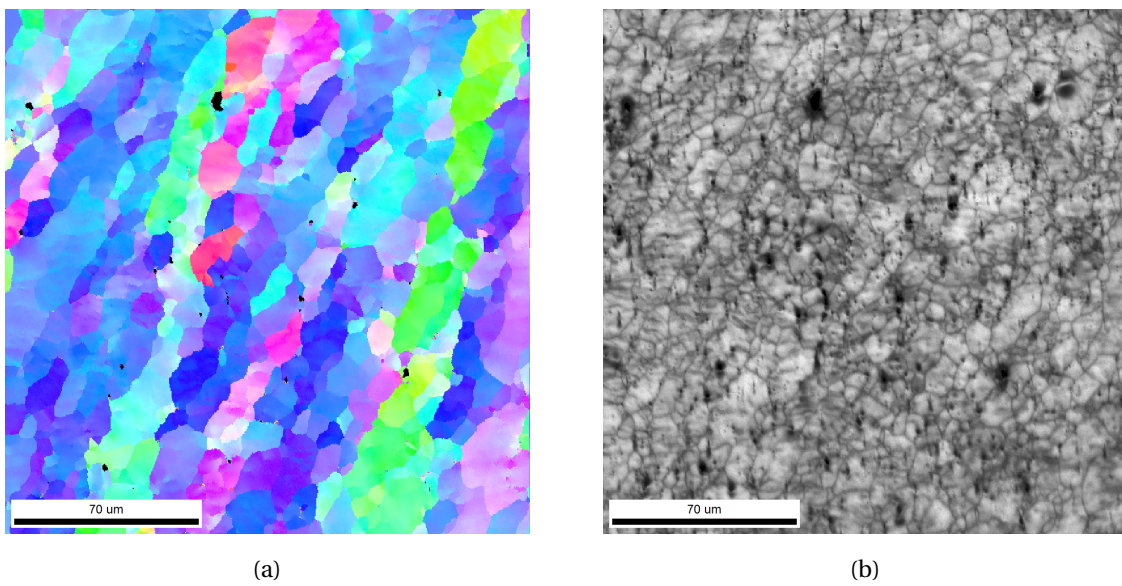


Figure B.10: (a) The IPF-map and (b) IQ-map for Sample  $\pi$ -1.4.

**B.10 Sample  $\pi$ -0.7**

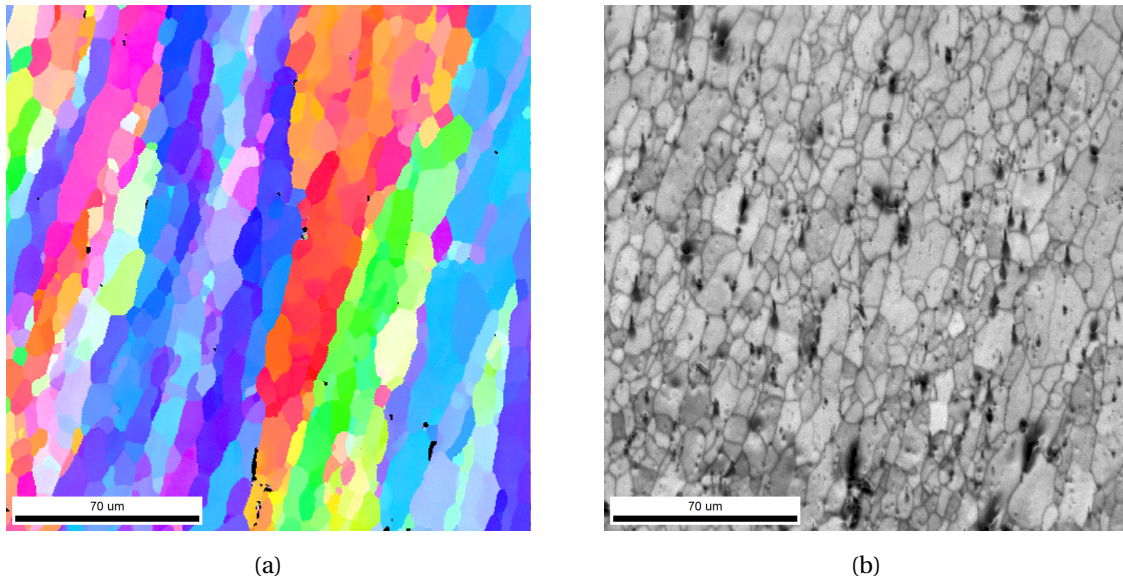


Figure B.11: (a) The IPF-map and (b) IQ-map for Sample  $\pi$ -0.7.

**B.11 Sample  $\pi$ -0.5**

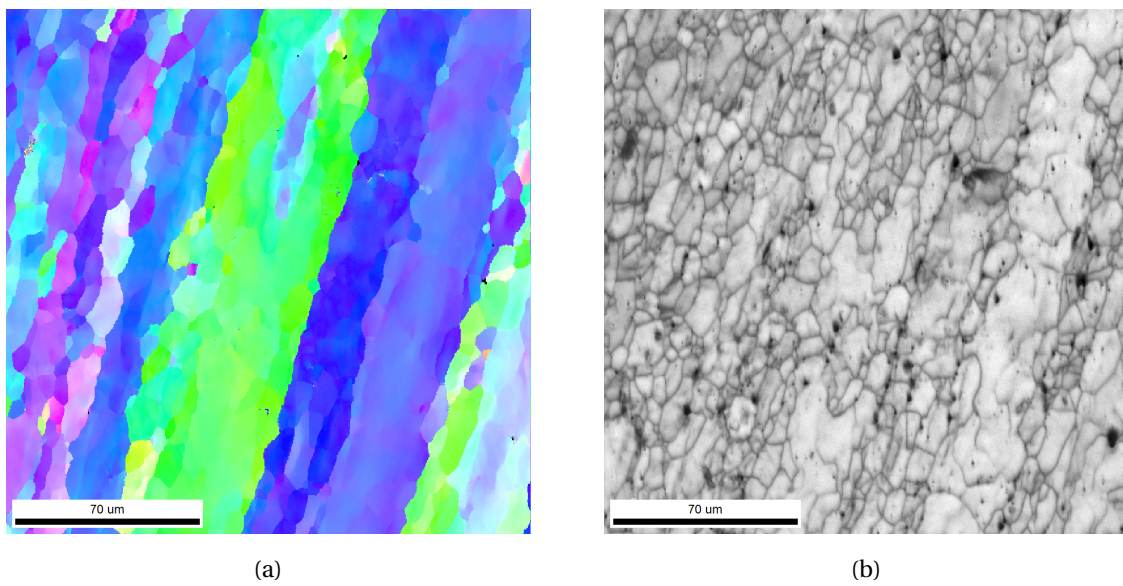


Figure B.12: (a) The IPF-map and (b) IQ-map for Sample  $\pi$ -0.5.



**B.12 Sample  $\pi$ -0.44**

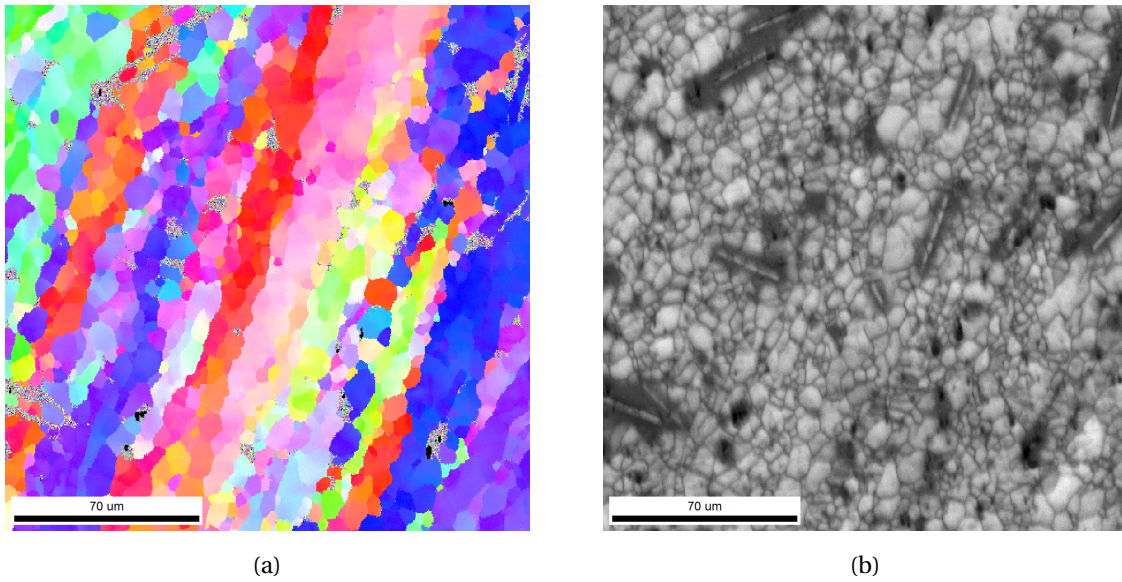


Figure B.13: (a) The IPF-map and (b) IQ-map for Sample  $\pi$ -0.87.

**B.13 Sample  $\pi$ -0.34**

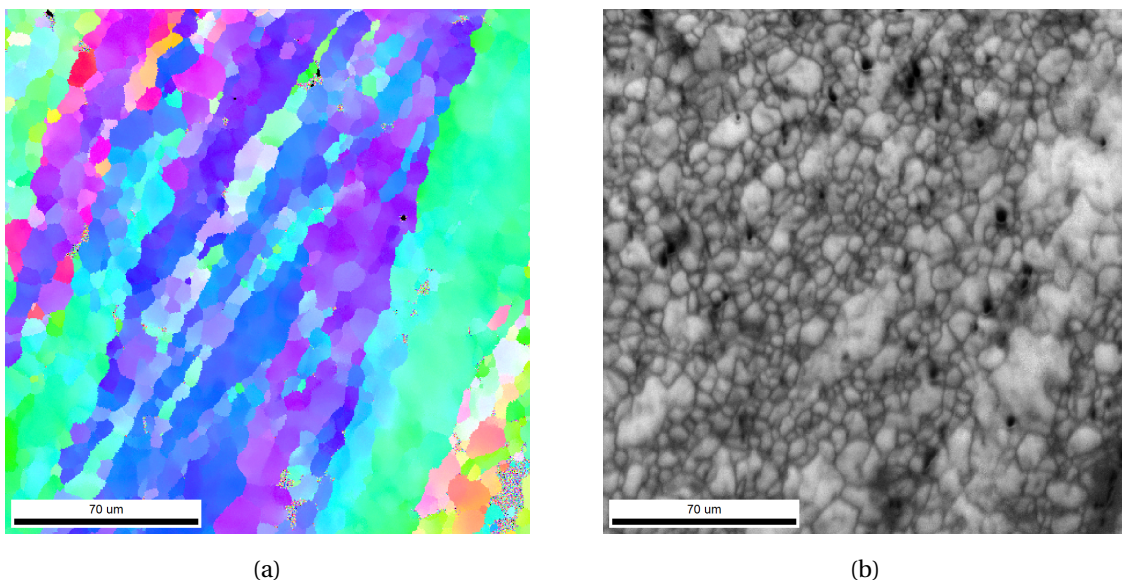


Figure B.14: (a) The IPF-map and (b) IQ-map for Sample  $\pi$ -0.34.



**B.14 Sample  $\pi$ -0.26**

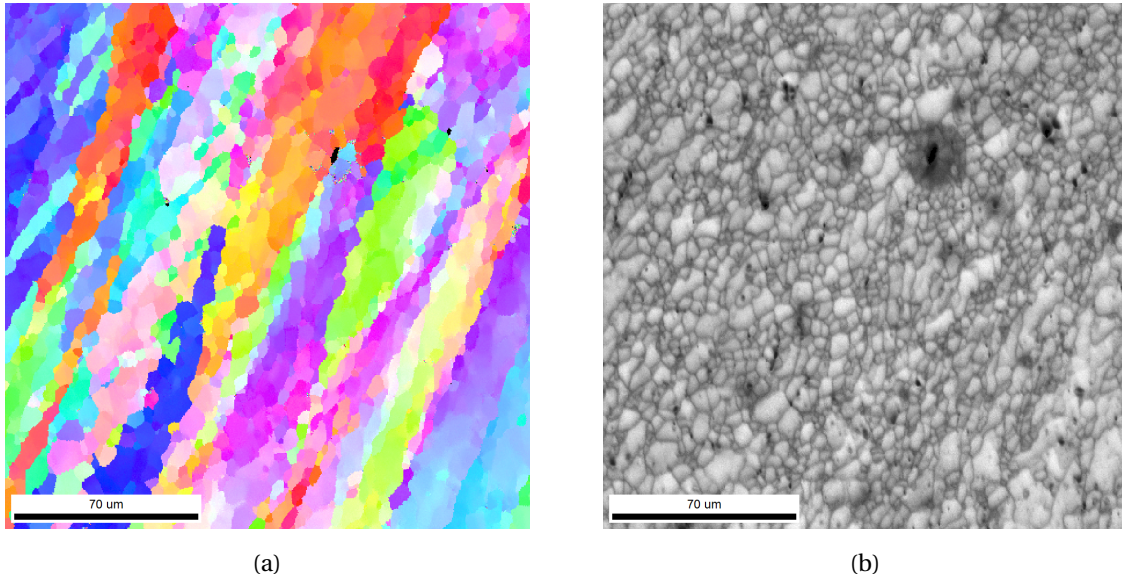


Figure B.15: (a) The IPF-map and (b) IQ-map for Sample  $\pi$ -0.26.

**B.15 Sample  $\pi$ -0.18**

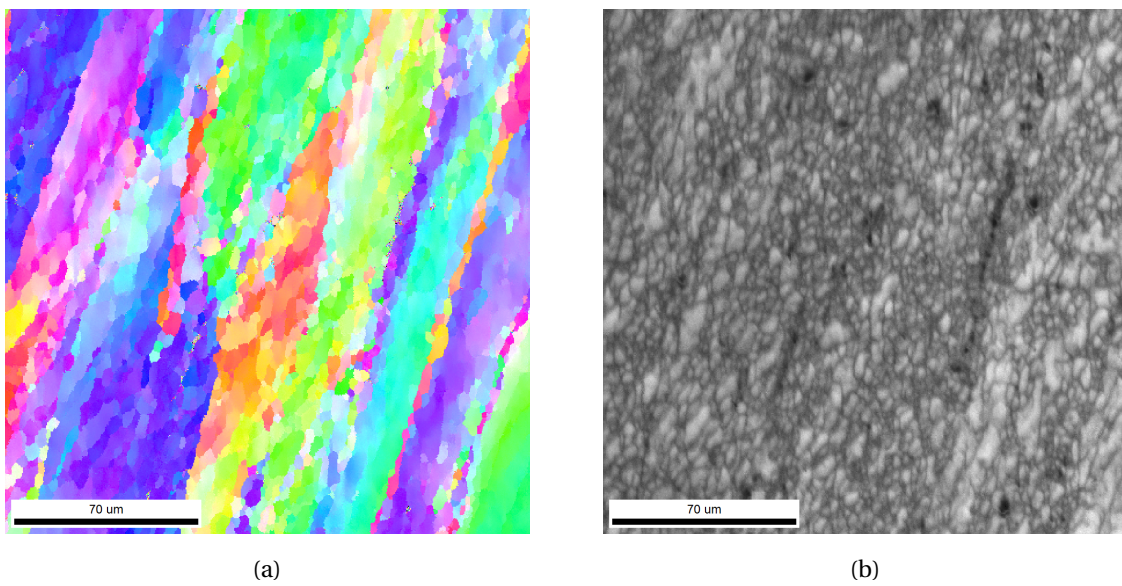


Figure B.16: (a) The IPF-map and (b) IQ-map for Sample  $\pi$ -0.18.

**B.16 Sample  $\pi$ -0.14**

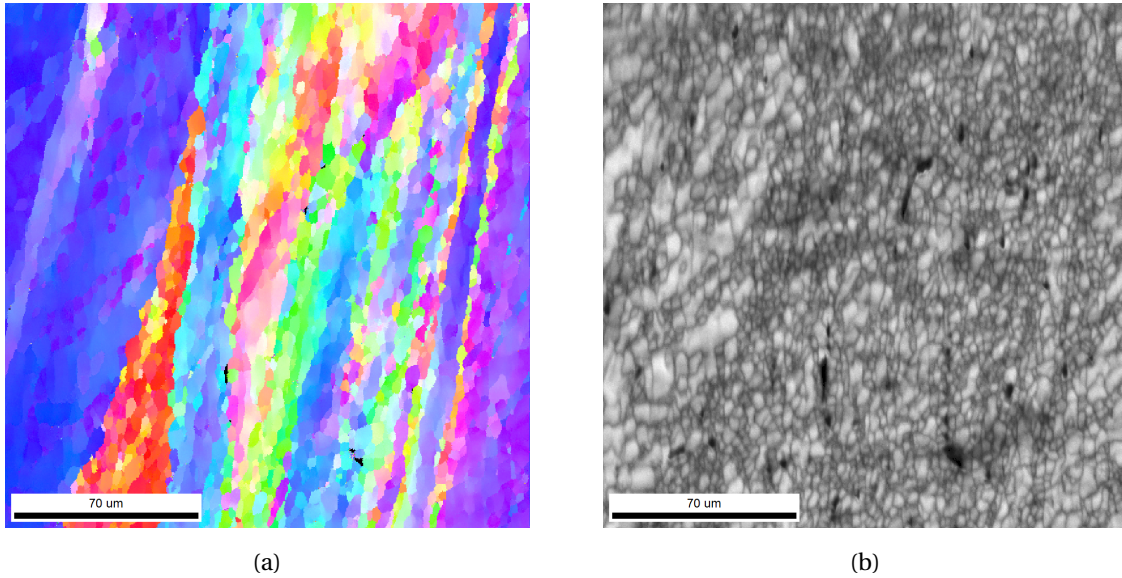


Figure B.17: (a) The IPF-map and (b) IQ-map for Sample  $\pi$ -0.14.

**B.17 Sample  $\pi$ -0.13**

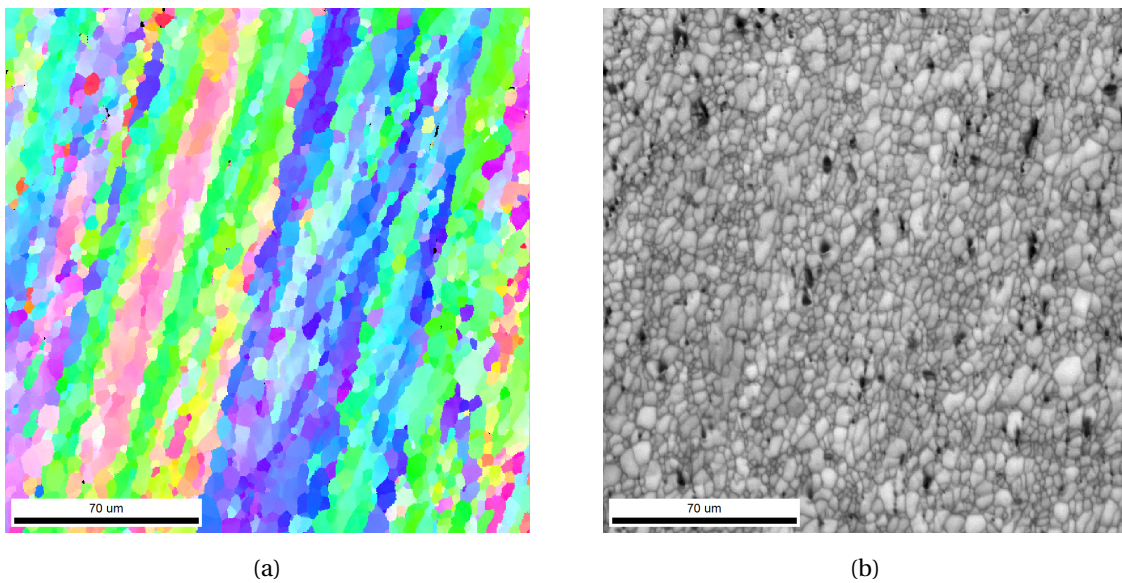


Figure B.18: (a) The IPF-map and (b) IQ-map for Sample  $\pi$ -0.13.

**B.18 Sample  $\pi$ -0.03**

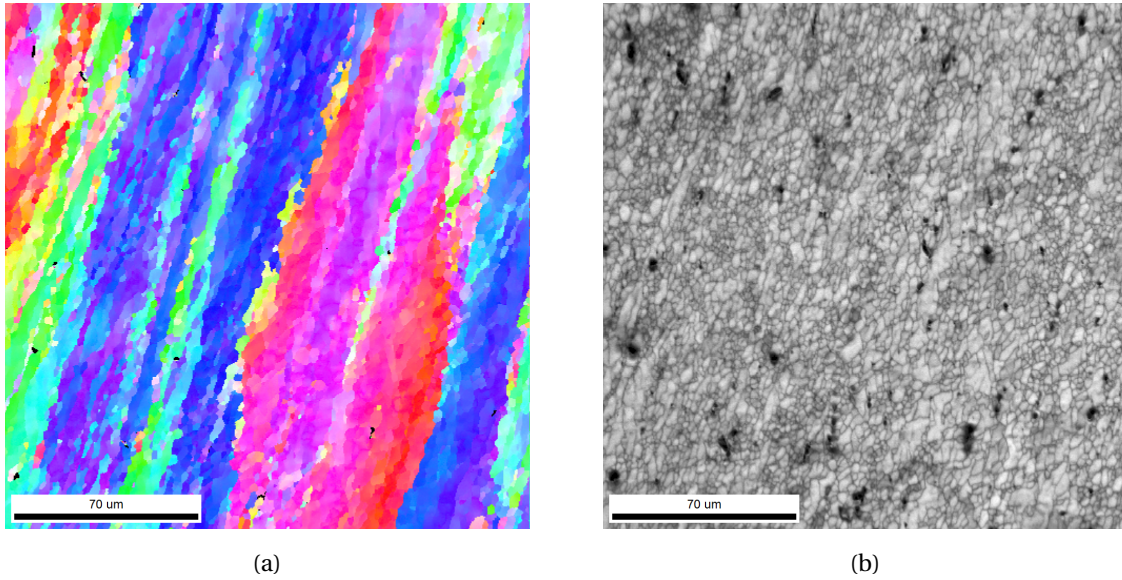


Figure B.19: (a) The IPF-map and (b) IQ-map for Sample  $\pi$ -0.03.



## C The Average Grain Size Values

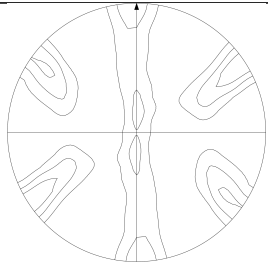
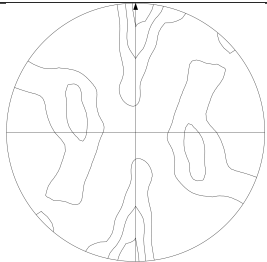
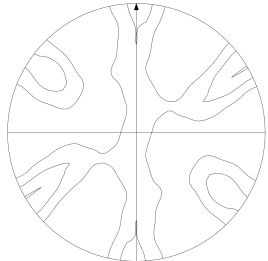
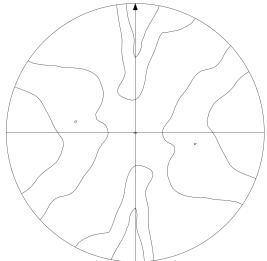
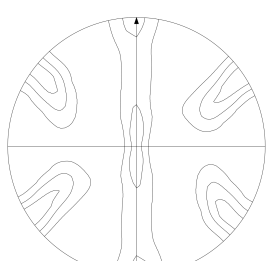
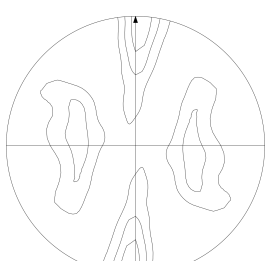
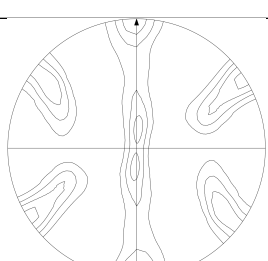
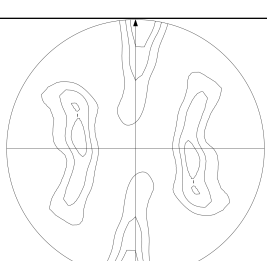
In this appendix the values in the average subgrain size plot in Figure 4.3 are presented in Table C.1.

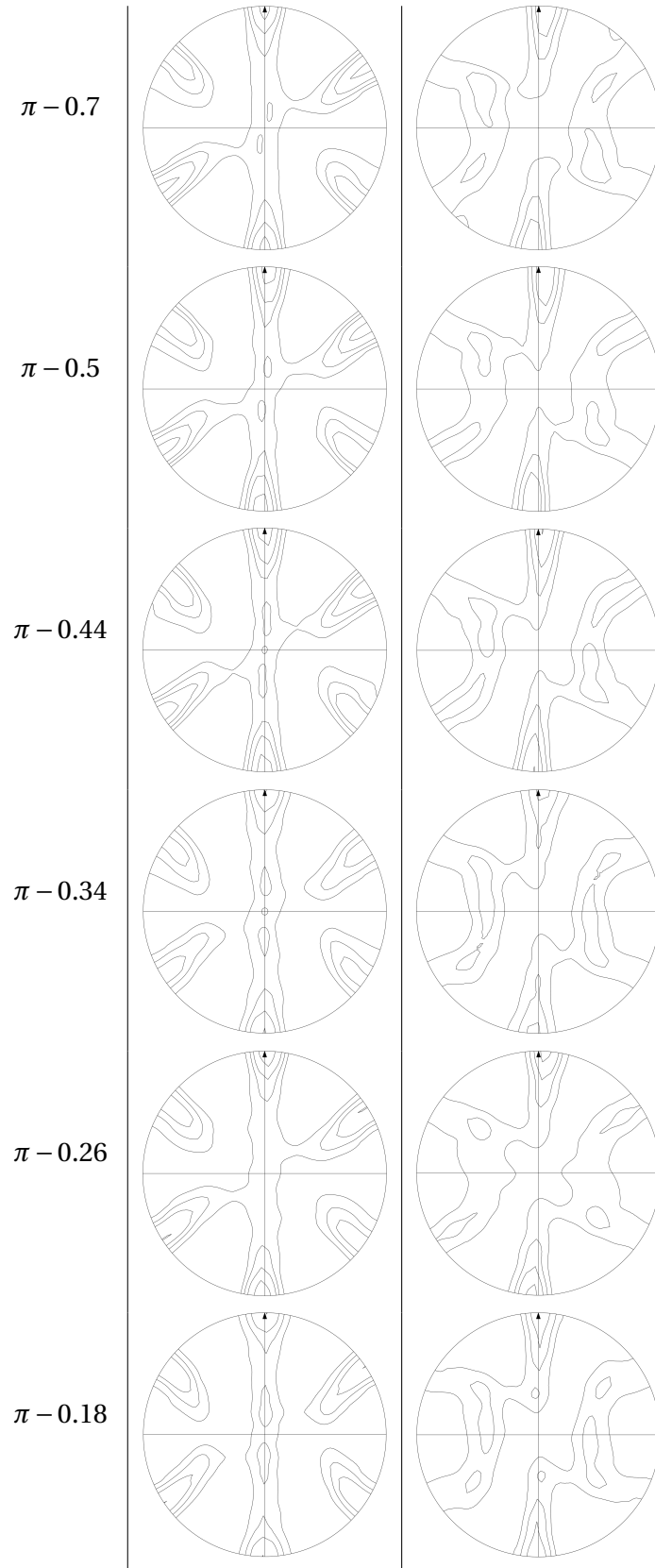
Table C.1: Values used in in Figure 4.3.

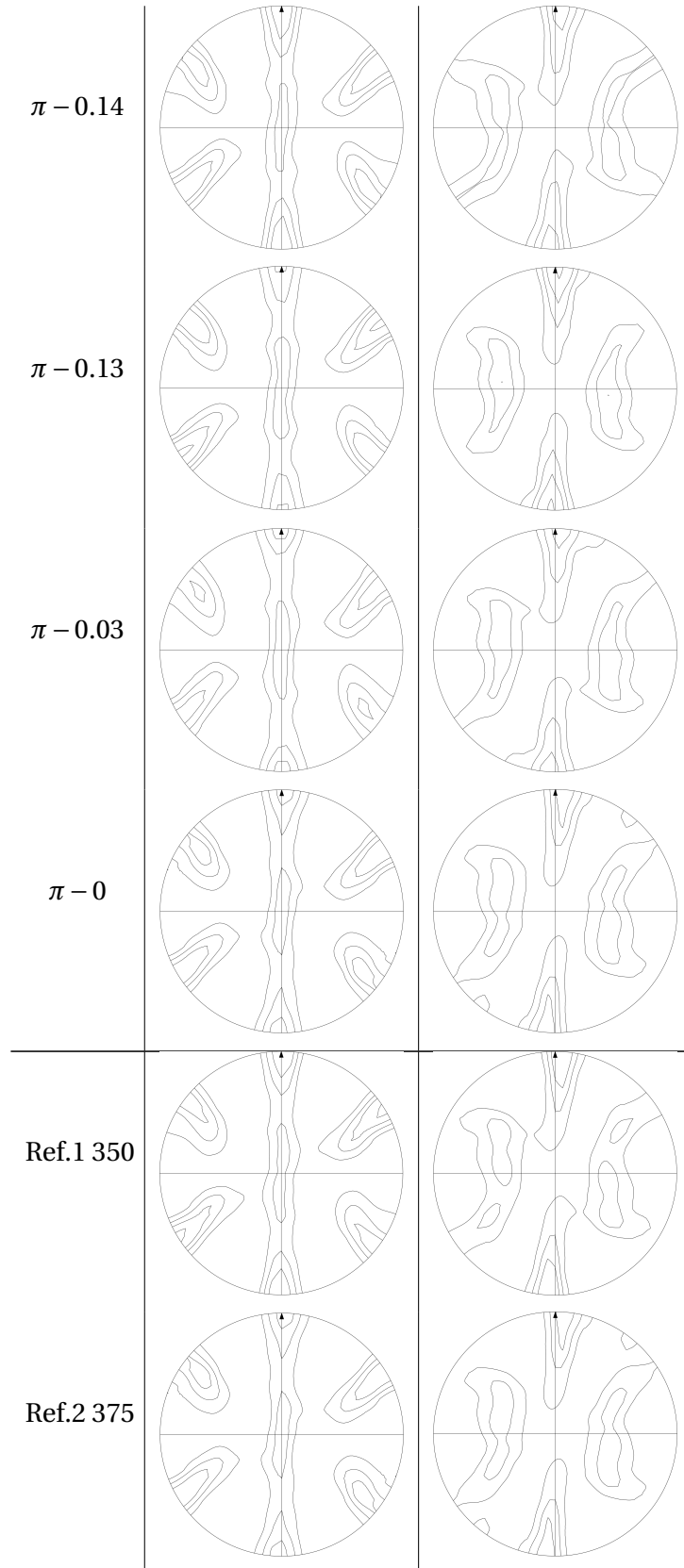
Sample ID	Shear Strain	$\bar{\delta}$	Standard Deviation
$\pi$ -1.4	2.7761	5.2785	0.1992
$\pi$ -0.7	1.3701	5.494	0.1922
$\pi$ -0.50	1.0225	5.674	0.2893
$\pi$ -0.44	0.8742	5.6584	0.4108
$\pi$ -0.34	0.6697	5.3746	0.4002
$\pi$ -0.26	0.5087	5.5422	0.4743
$\pi$ -0.18	0.3476	4.0622	0.3307
$\pi$ -0.14	0.271	3.4794	0.2229
$\pi$ -0.13	0.2556	3.5876	0.1462
$\pi$ -0.03	0.0511	2.2041	0.1185
$\pi$ -0	0	2.3955	0.0539

## D Pole figures

The XRD obtained 111 and 200-pole figures for all samples are presented in Table D.1. All pole figures are presented with equal contour maps. The first (horizontal) axis of the pole figures is the  $\theta$  direction, and the second (vertical) axis is the  $z$  direction in relation to the torsion samples.

Sample	111-pole figure	200-pole figure
$0 - \pi$		
$0 - \pi$ NQ		
$0 - 4.71$		
$\pi - 1.4$		





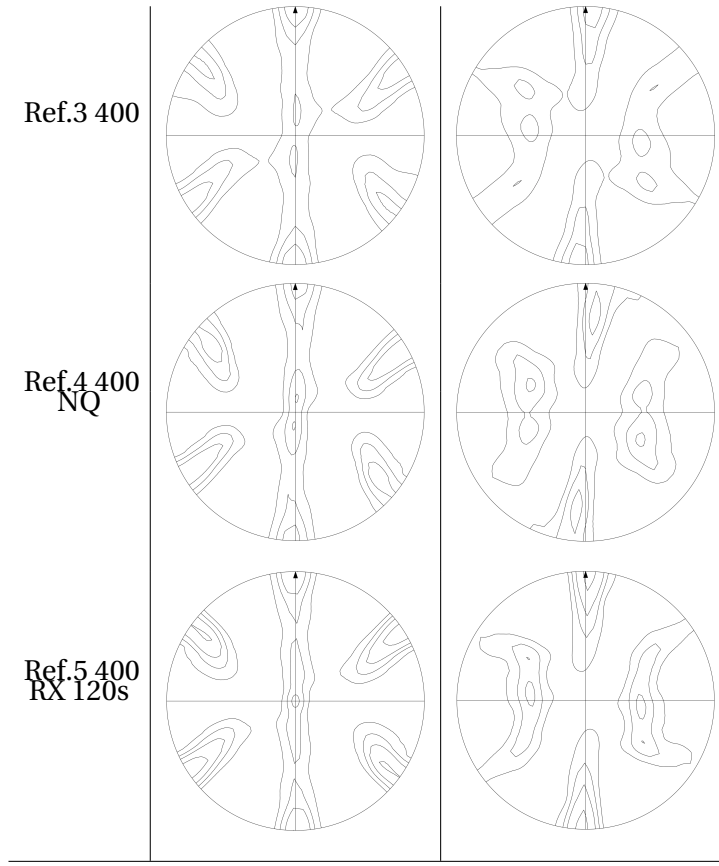
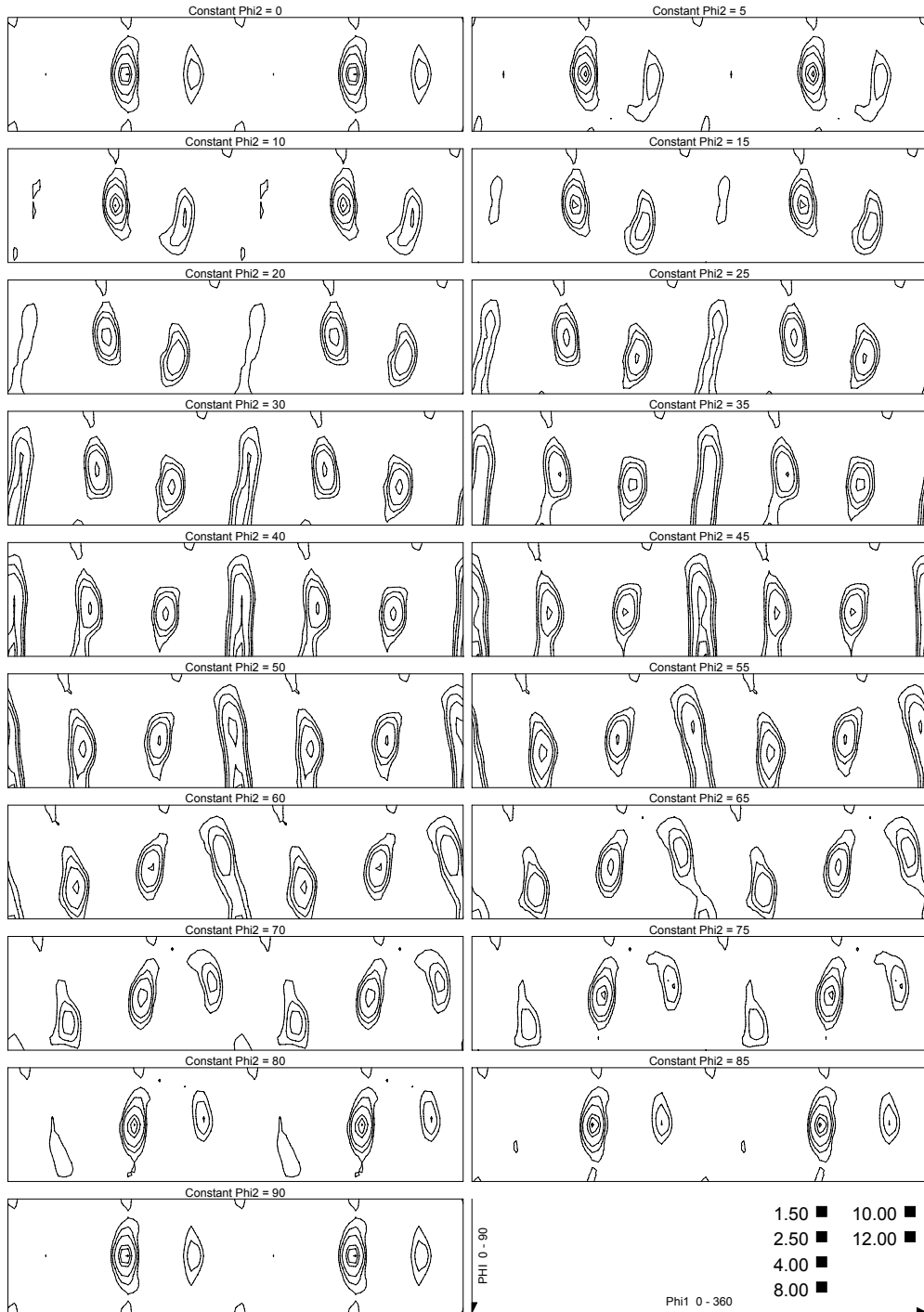


Table D.1: The 111 and 200-pole figures with contour maps with intensities of 1/2/3/4.5/6.

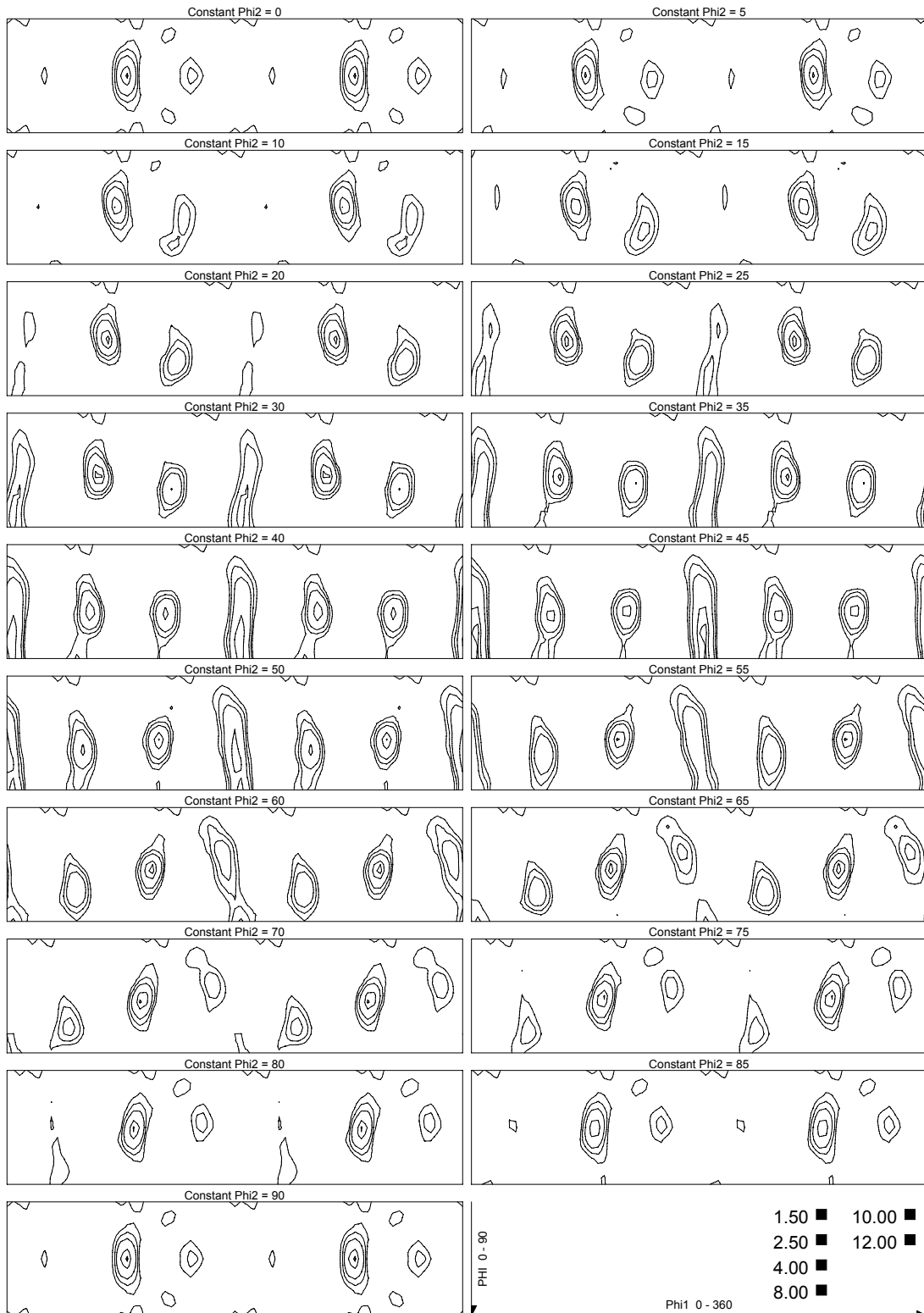


# E The full ODFs



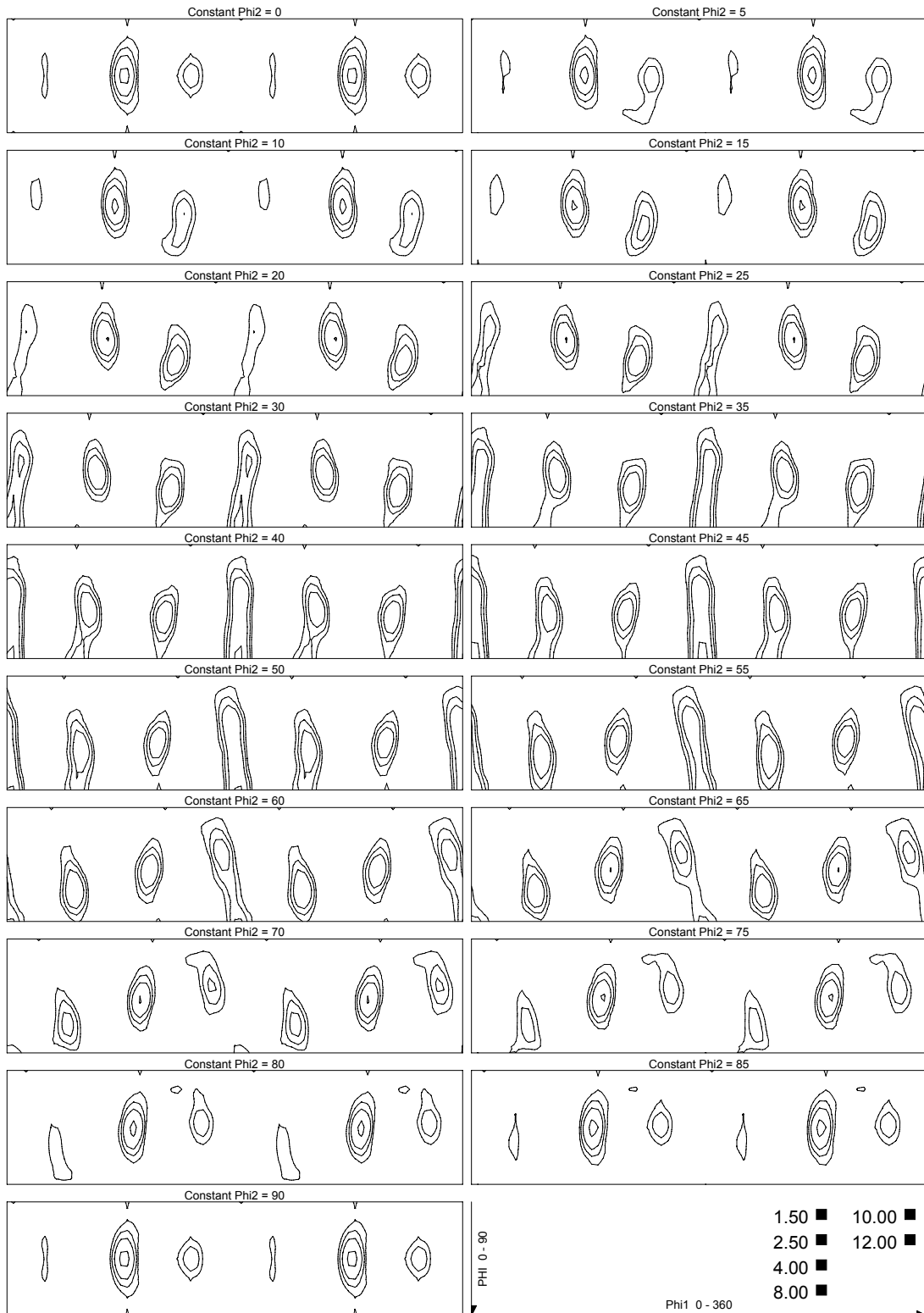
(a)

Figure E.1: ODF for Sample Ref.1 350°C



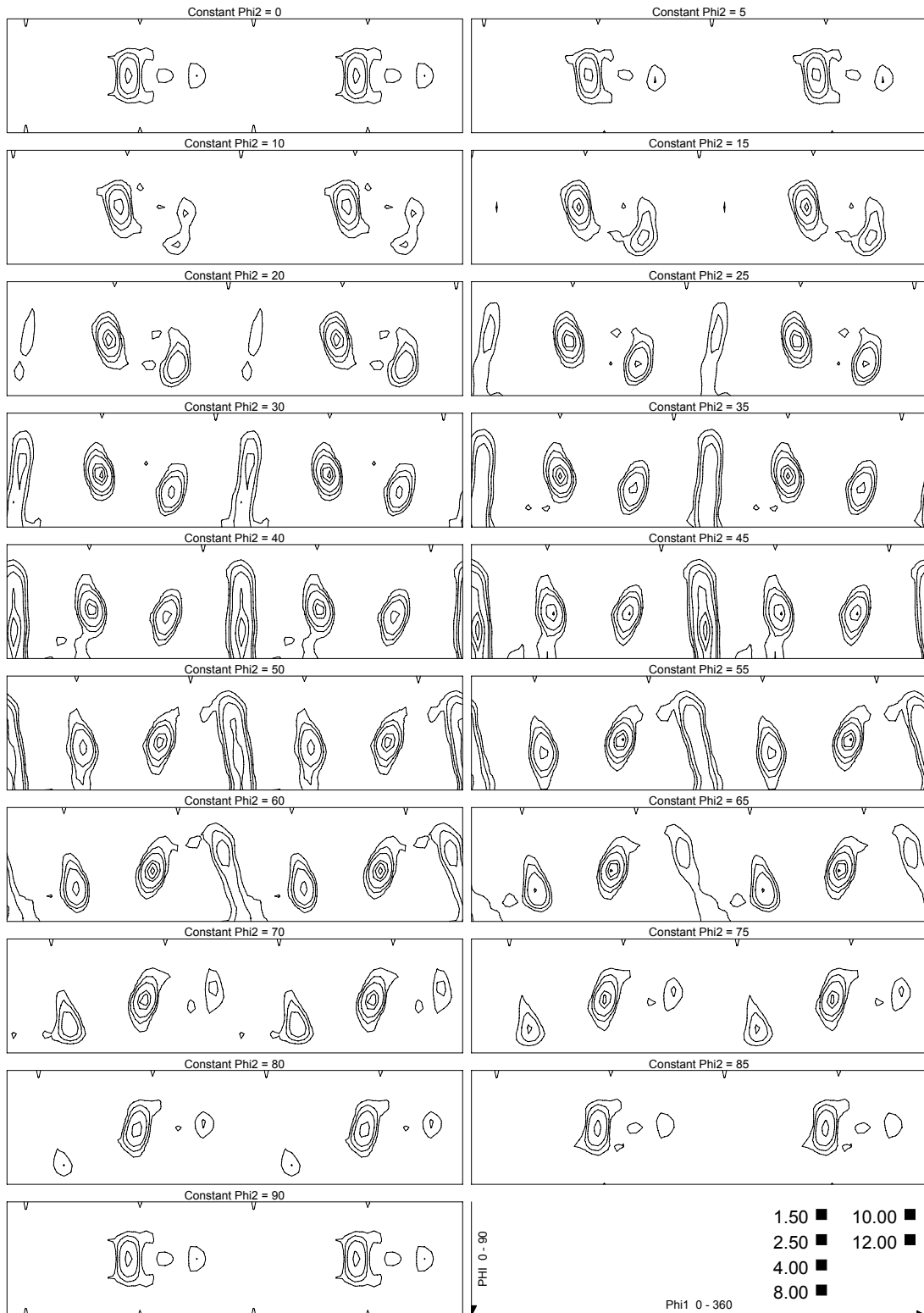
(b)

Figure E.1: ODF for Sample Ref.2 375°C



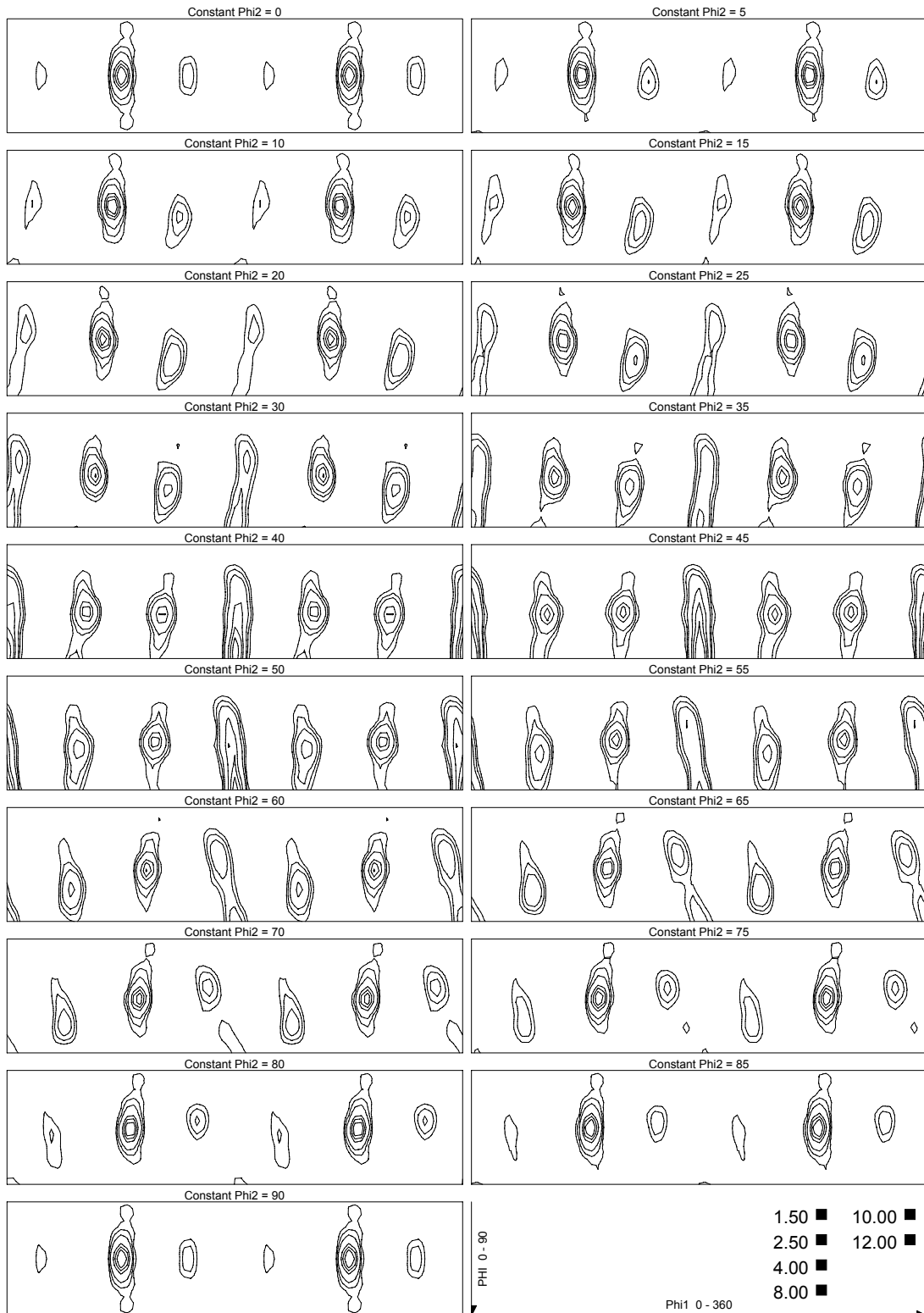
(c)

Figure E.1: ODF for Sample Ref.3 400°C



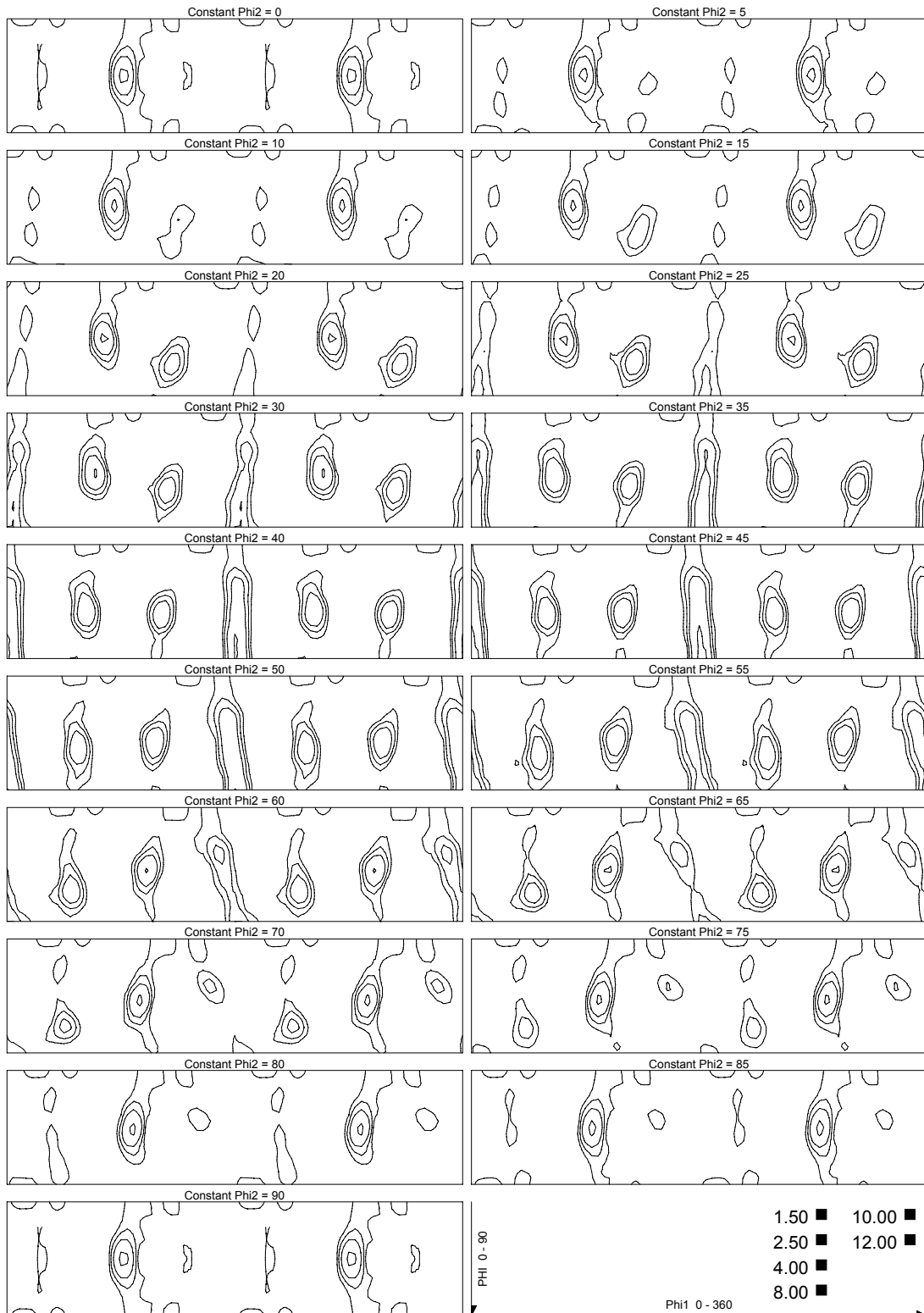
(d)

Figure E.1: ODF for Sample Ref.4 400°C NQ



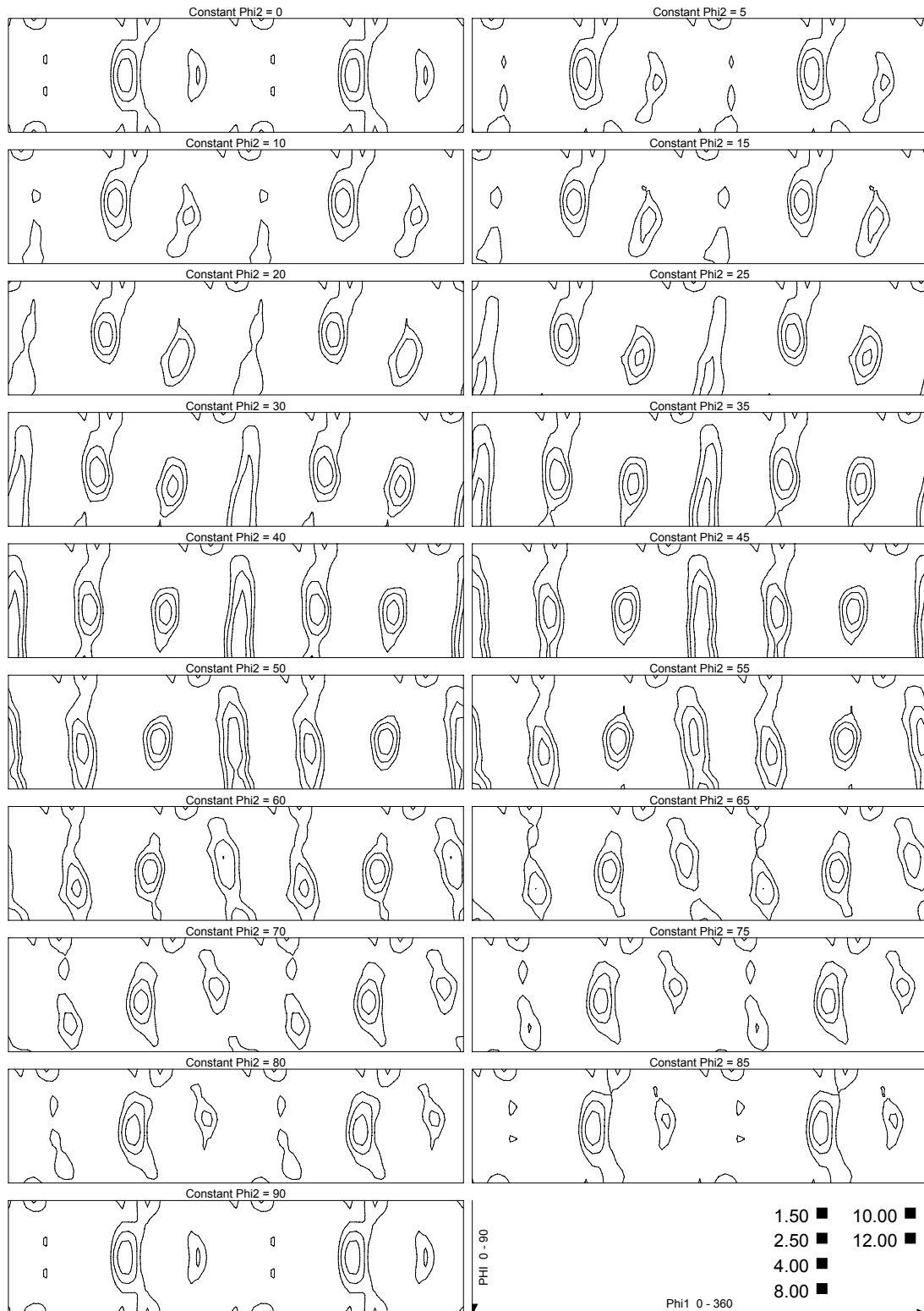
(e)

Figure E.1: ODF for Sample Ref.5 375°C annealed 120sec



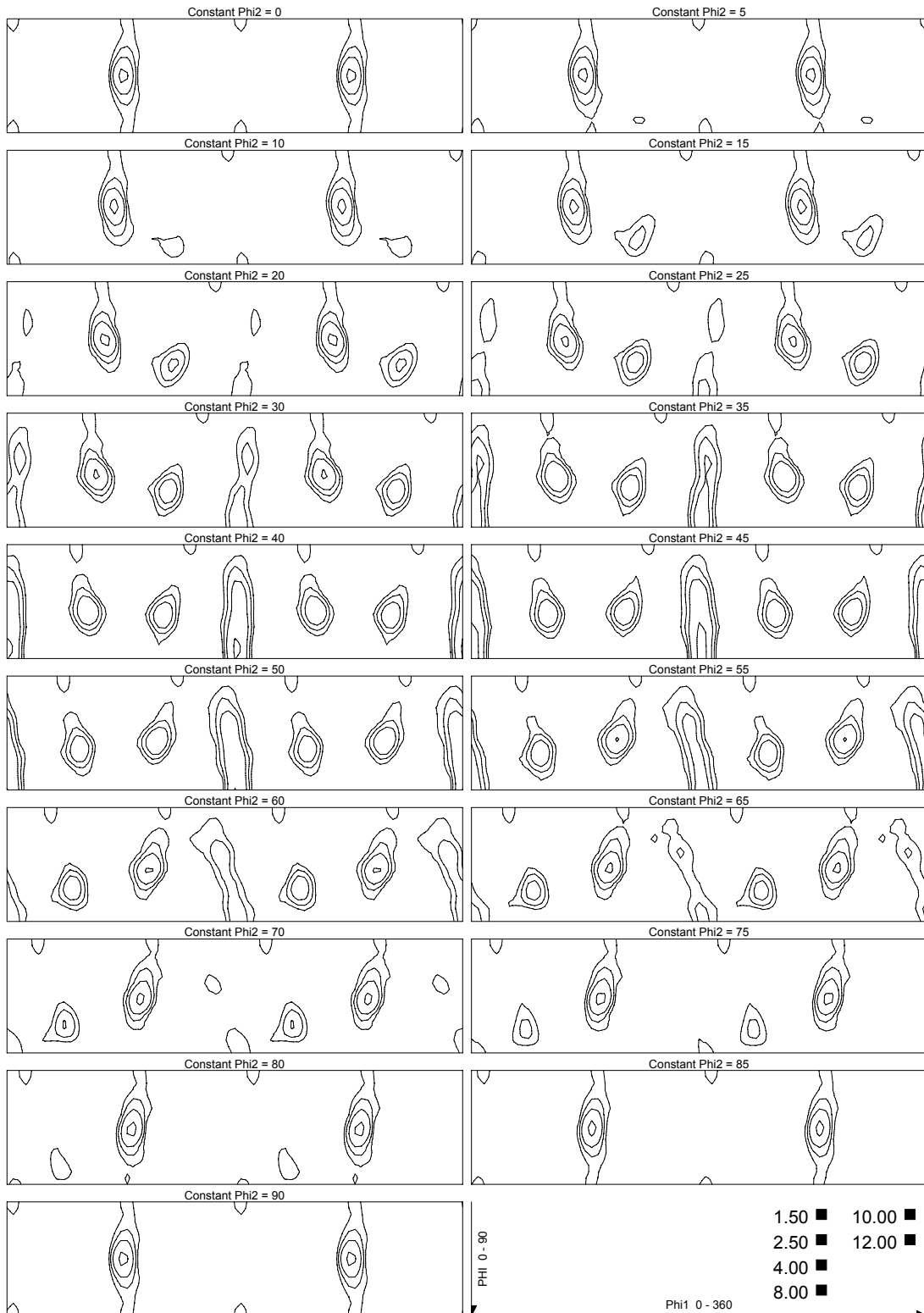
(f)

Figure E.1: ODF for Sample 0- $\pi$



(g)

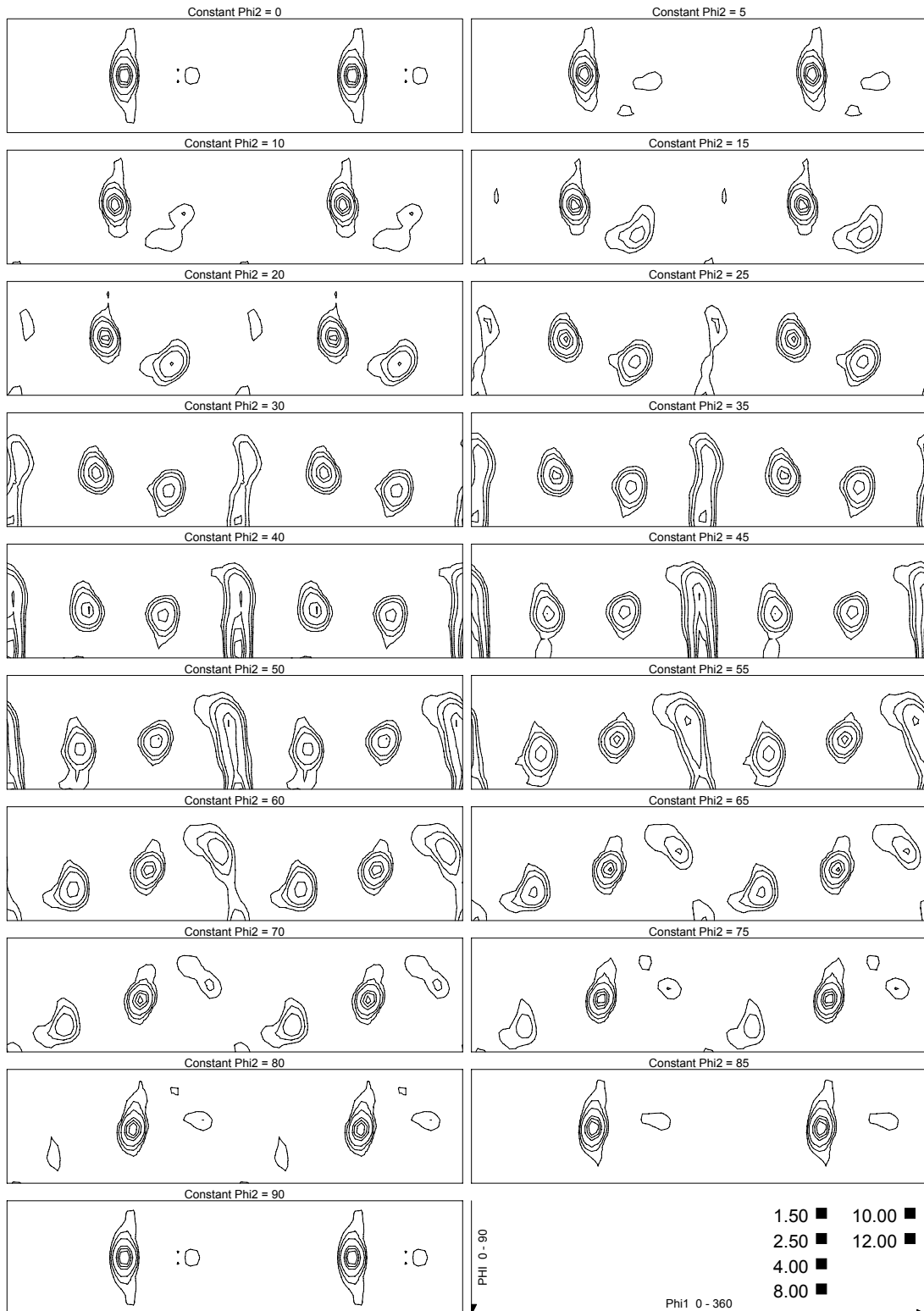
Figure E.1: ODF for Sample  $\pi$ -0 NQ



(h)

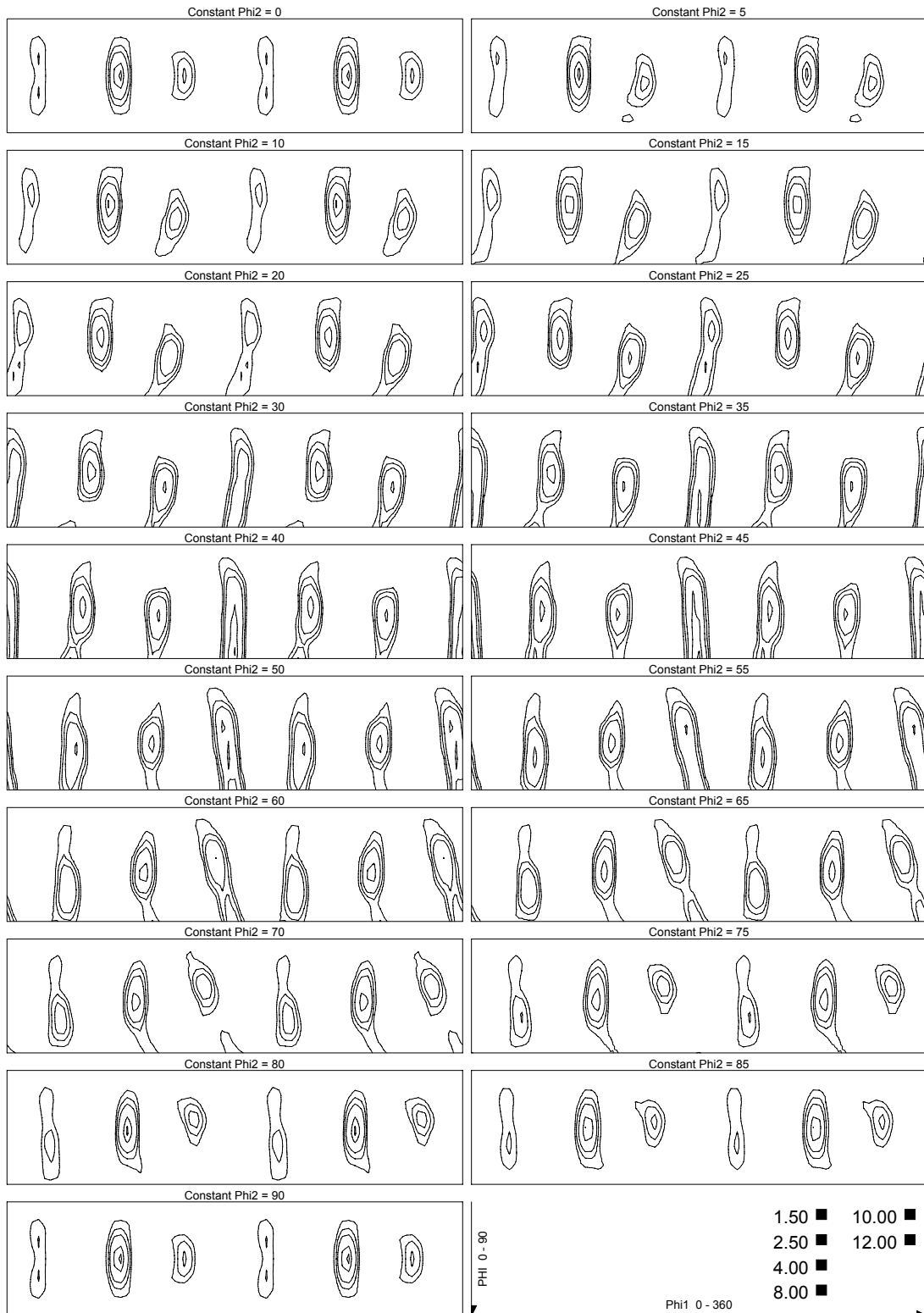
Figure E.1: ODF for Sample 0-4.71





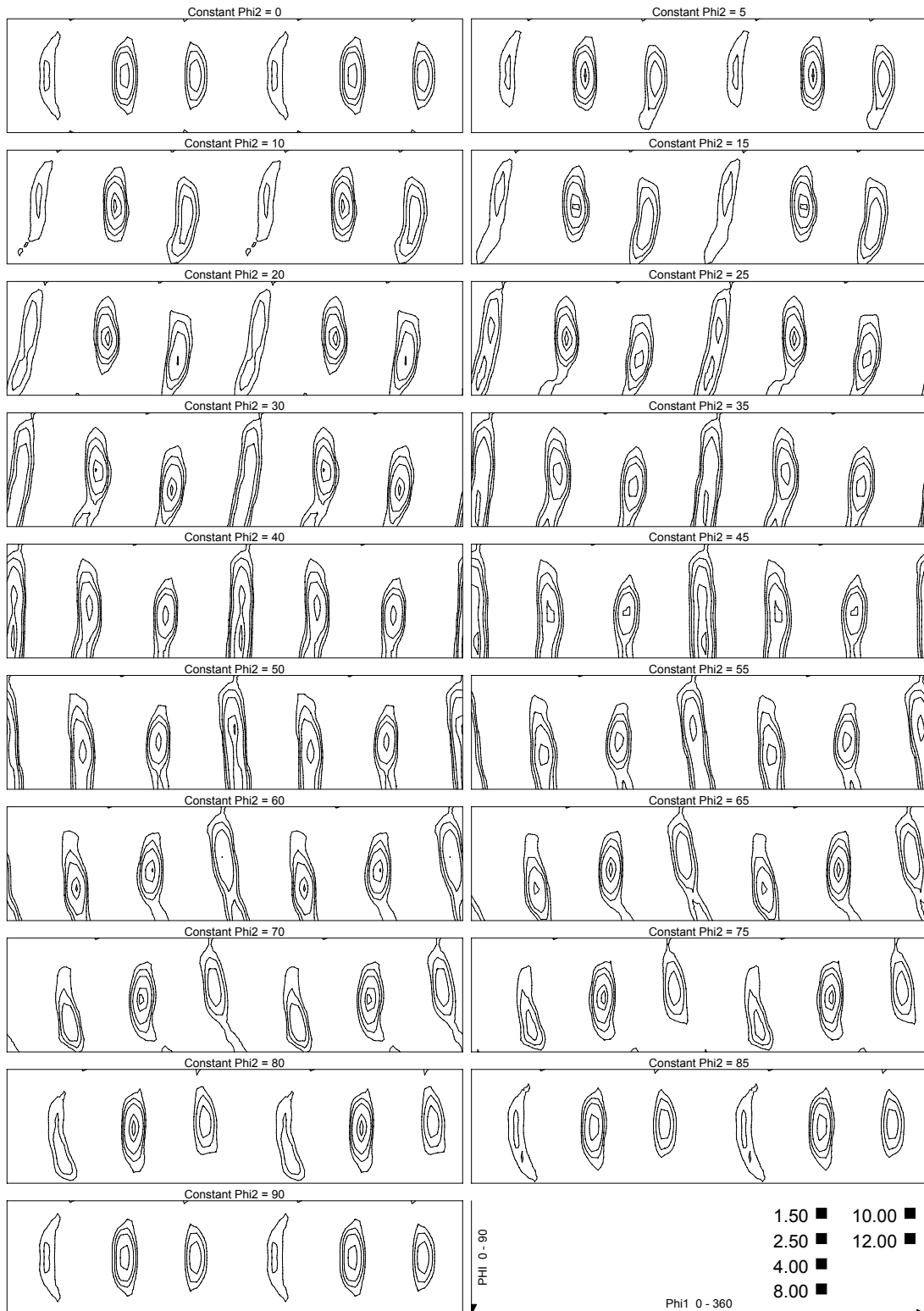
(i)

Figure E.1: ODF for Sample  $\pi$ -1.4



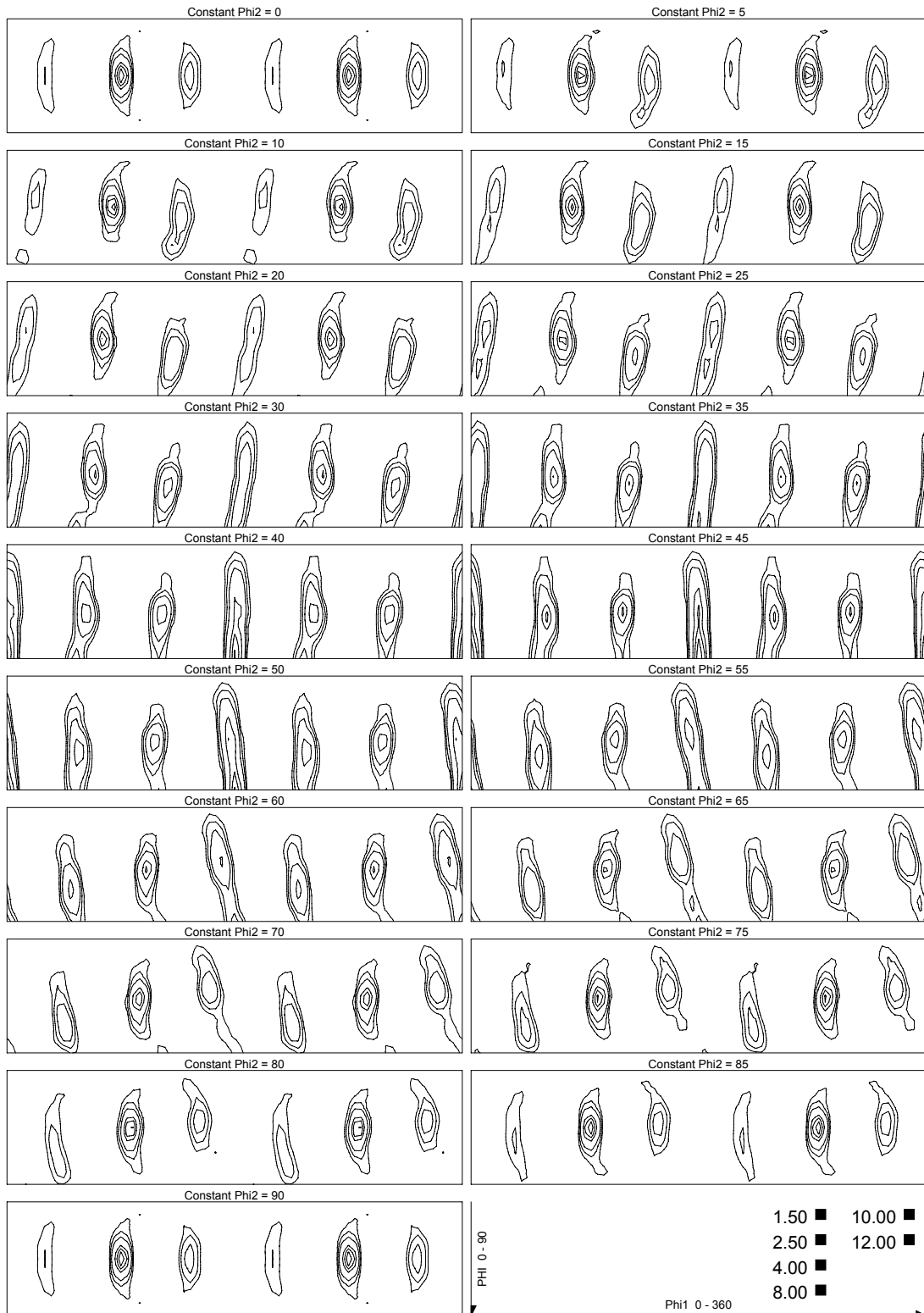
(j)

Figure E.1: ODF for Sample  $\pi$ -0.7



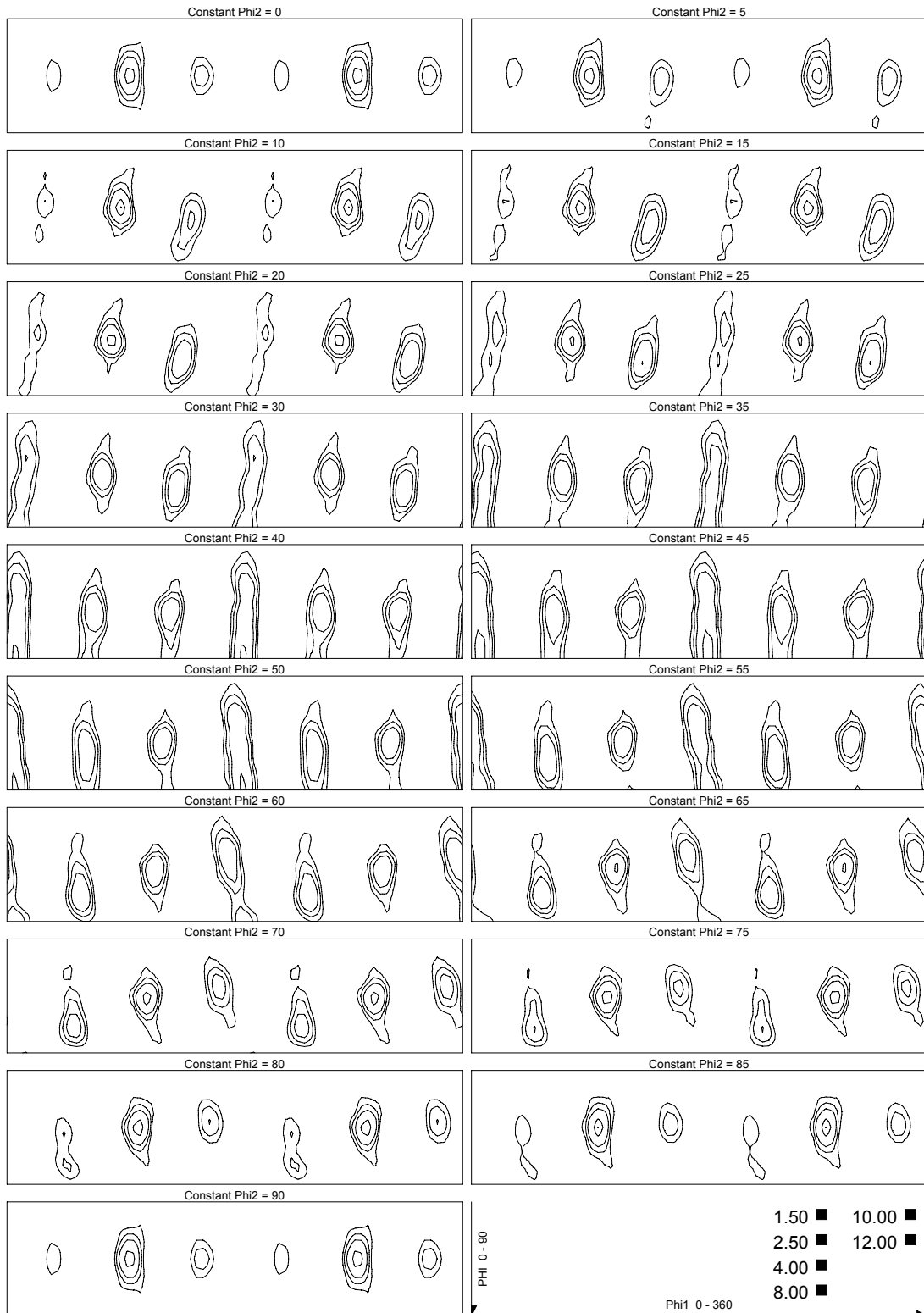
(k)

Figure E.1: ODF for Sample  $\pi$ -0.50



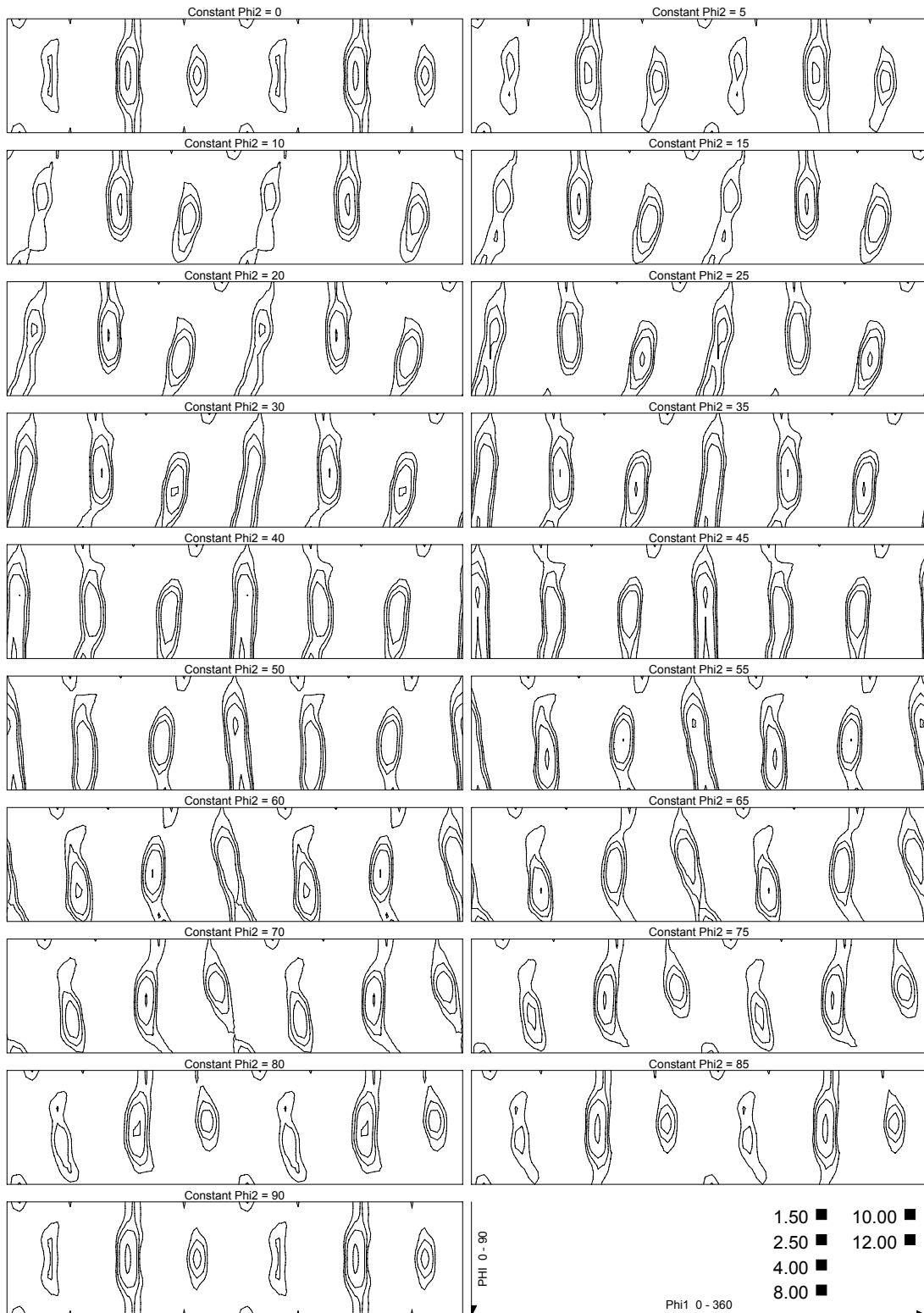
(1)

Figure E.1: ODF for Sample  $\pi$ -0.44



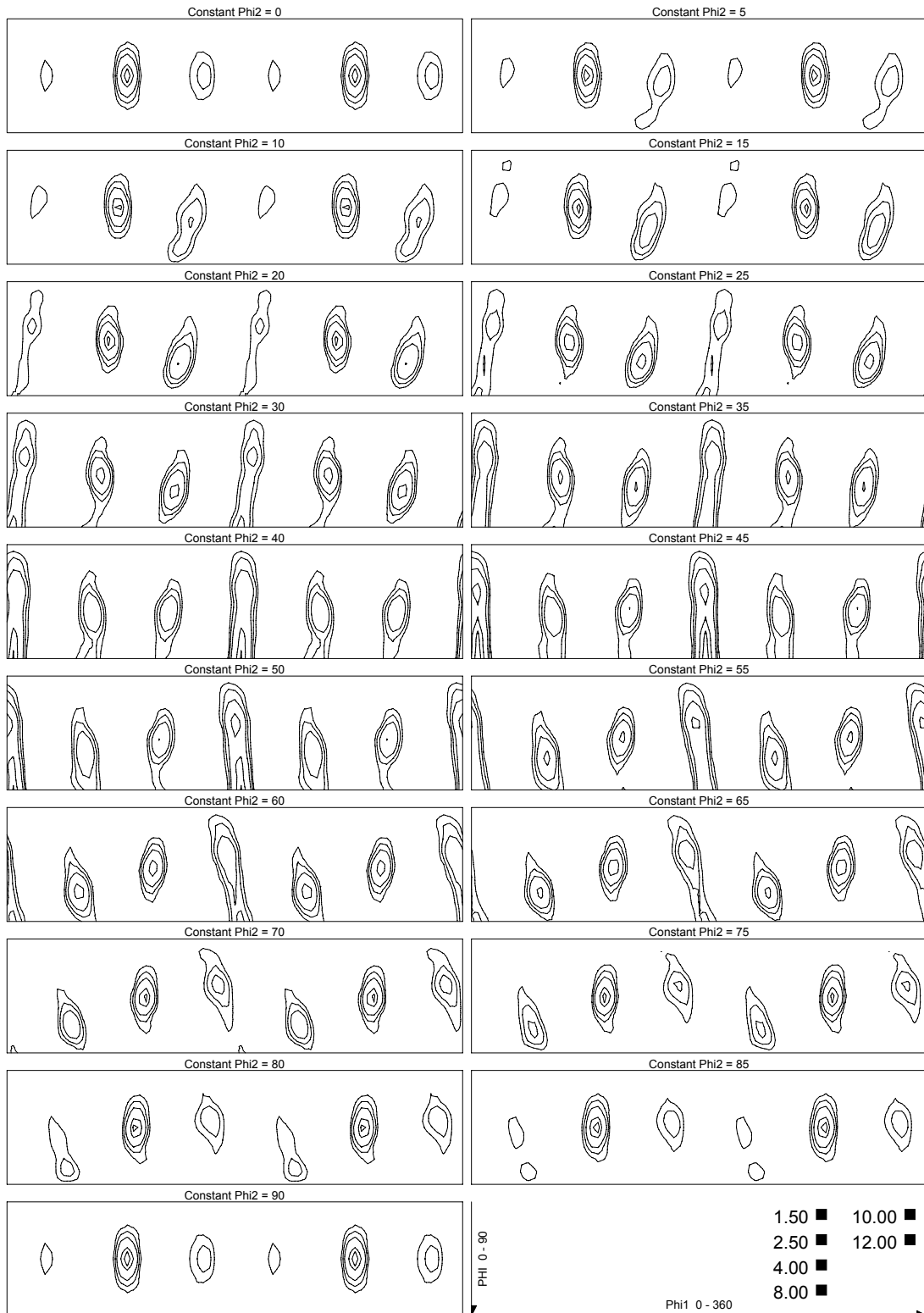
(m)

Figure E.1: ODF for Sample  $\pi$ -0.34



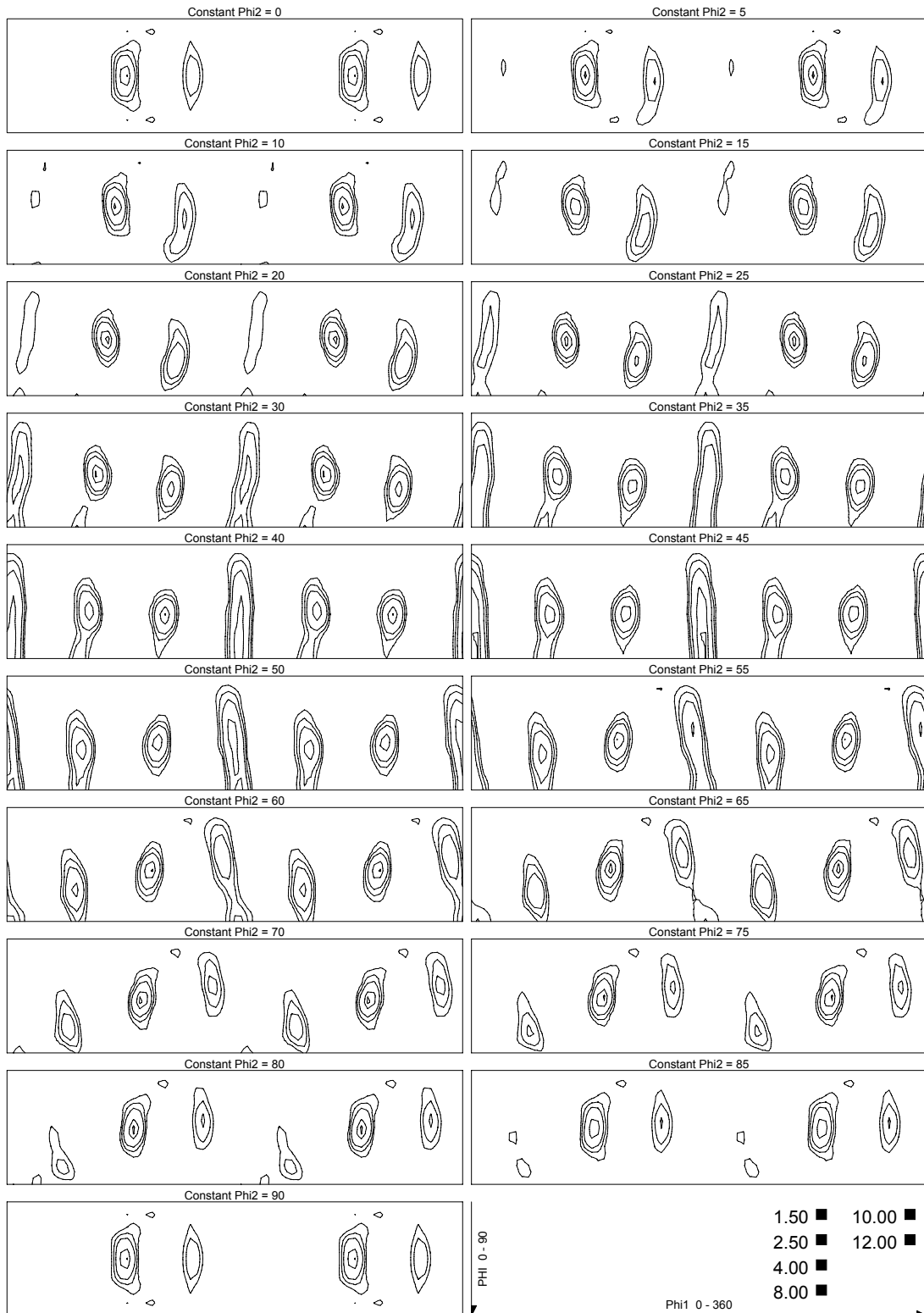
(n)

Figure E.1: ODF for Sample  $\pi$ -0.26



(o)

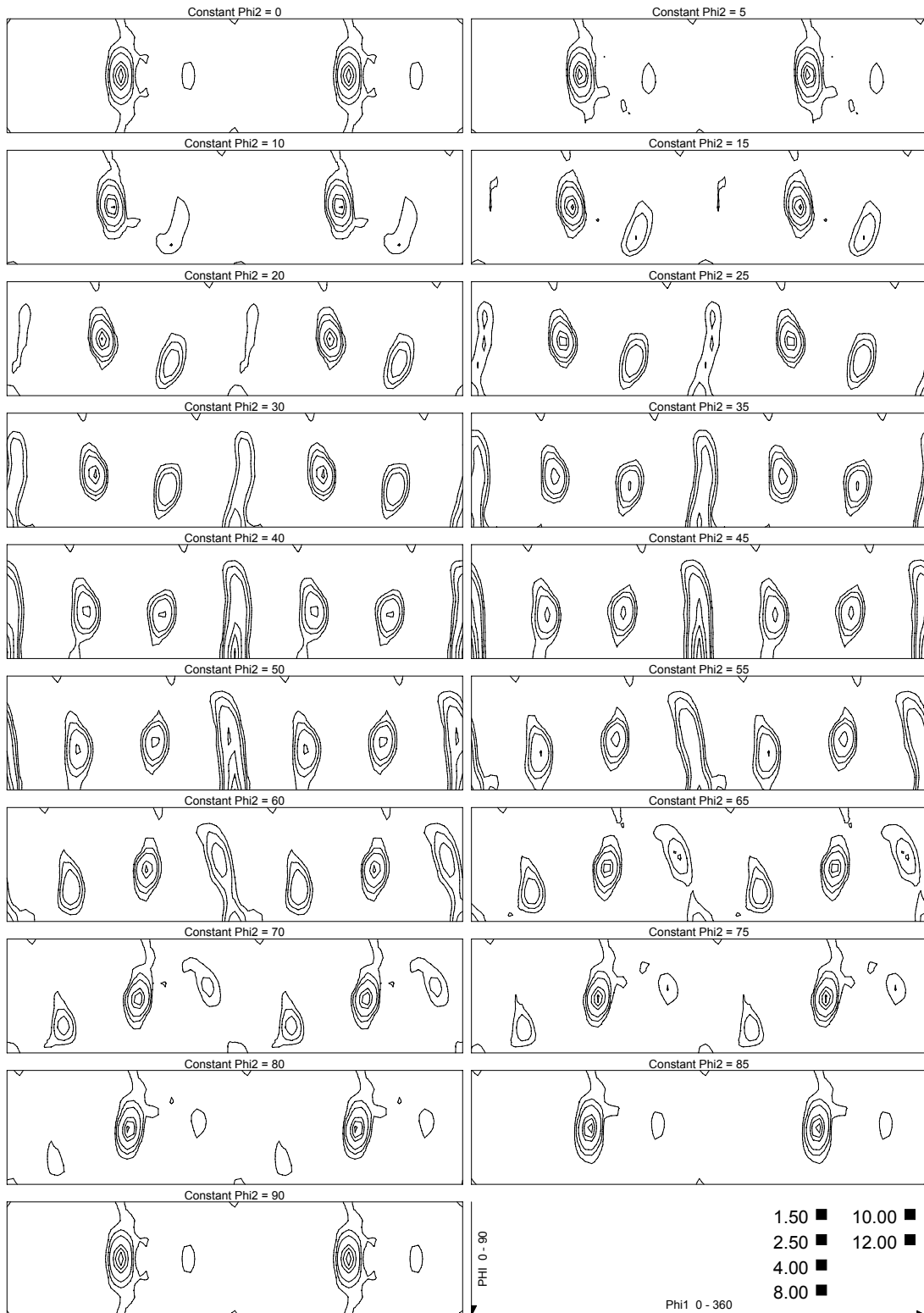
Figure E.1: ODF for Sample  $\pi$ -0.18



(p)

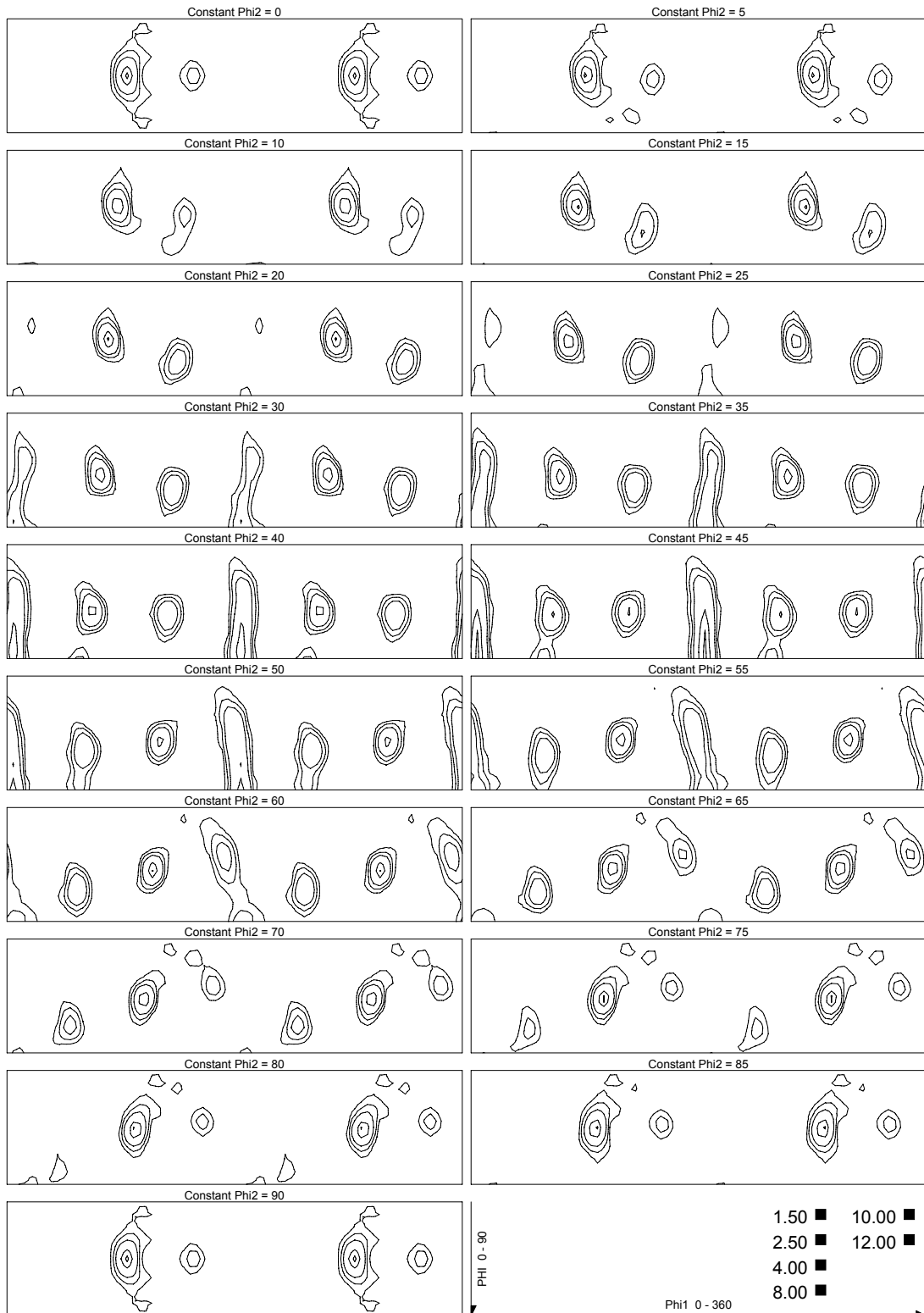
Figure E.1: ODF for Sample  $\pi$ -0.14





(q)

Figure E.1: ODF for Sample  $\pi$ -0.13



(r)

Figure E.1: ODF for Sample  $\pi$ -0.03